UNIVERSITY *of* York

This is a repository copy of *Grain boundaries in polycrystalline materials for energy applications : First principles modeling and electron microscopy*.

White Rose Research Online URL for this paper:
https://eprints.whiterose.ac.uk/208488/

Version: Published Version

Article:

Quirk, J., Rothmann, M., Li, W. et al. (2 more authors) (2024) Grain boundaries in polycrystalline materials for energy applications : First principles modeling and electron microscopy. Applied Physics Reviews. 011308. ISSN 1931-9401

https://doi.org/10.1063/5.0175150

White Rose
university consortium
Universities of Leeds, Sheffield & York

eprints@whiterose.ac.uk
https://eprints.whiterose.ac.uk/

Grain boundaries in polycrystalline materials for energy applications: First principles modeling and electron microscopy 🕩

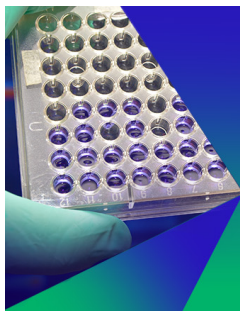J. Quirk ⬤ ; M. Rothmann ⬤ ; W. Li ⬤ ; D. Abou-Ras ⬤ ; K. P. McKenna ✉ ⬤

Check for updates

View Online   Export Citation   CrossMark

Grain boundaries in polycrystalline materials for energy applications: First principles modeling and electron microscopy Ⓕ

View Online   Export Citation   CrossMark

J. Quirk,[1] ⓘD M. Rothmann,[2] ⓘD W. Li,[2] ⓘD D. Abou-Ras,[3] ⓘD and K. P. McKenna[4,a] ⓘD

AFFILIATIONS

[1]Chemistry – School of Natural and Environmental Science, Newcastle University, Newcastle upon Tyne NE1 7RU, United Kingdom
[2]Foshan Xianhu Laboratory of the Advanced Energy Science and Technology Guangdong Laboratory, Xianhu Hydrogen Valley, Foshan 528200, People's Republic of China
[3]Helmholtz-Zentrum Berlin für Materialien und Energie GmbH, Berlin, Germany
[4]School of Physics, Engineering and Technology, University of York, York, YO10 5DD, United Kingdom

[a]Author to whom correspondence should be addressed: keith.mckenna@york.ac.uk

ABSTRACT

Polycrystalline materials are ubiquitous in technology, and grain boundaries have long been known to affect materials properties and performance. First principles materials modeling and electron microscopy methods are powerful and highly complementary for investigating the atomic scale structure and properties of grain boundaries. In this review, we provide an introduction to key concepts and approaches for investigating grain boundaries using these methods. We also provide a number of case studies providing examples of their application to understand the impact of grain boundaries for a range of energy materials. Most of the materials presented are of interest for photovoltaic and photoelectrochemical applications and so we include a more in depth discussion of how modeling and electron microscopy can be employed to understand the impact of grain boundaries on the behavior of photoexcited electrons and holes (including carrier transport and recombination). However, we also include discussion of materials relevant to rechargeable batteries as another important class of materials for energy applications. We conclude the review with a discussion of outstanding challenges in the field and the exciting prospects for progress in the coming years.

TABLE OF CONTENTS

31 January 2024 08:53:32

I. INTRODUCTION

The majority of materials found in nature or those synthesized for fundamental studies or technological applications are crystalline, i.e., their constituent atoms are arranged into periodic structures characterized by a long-range spatial order. However, perfect single crystals are relatively uncommon, and most crystalline materials are instead polycrystalline with a microstructure characterized by an ensemble of grains with particular crystallographic orientations, shapes, and compositions separated by grain boundaries.[1] Grain boundaries are a ubiquitous class of extended defect that has long been known to be important for determining the properties of materials (including mechanical,[2,3] electronic,[4–8] optical,[9–11] magnetic,[12–15] and thermal[16,17]). For example, the interaction of dislocations (another ubiquitous type of extended defect) with grain boundaries plays a key role in determining the hardness of metals—a fact that is important for the millennia-old technologies of metal working and sword making but was not properly understood until the 20th century.[18] In the latter half of the 20th century, the emergence and rapid development of semiconductor devices led to increased understanding of the often deleterious impact of extended defects, such as grain boundaries, on optoelectronic properties of materials, such as charge-carrier mobility and electron–hole recombination.[19,20] As we now head toward the middle of the 21st century, one of the most pressing materials challenges we face is the urgent need to decarbonize our energy supply, economy, and society in order to secure a sustainable future for humanity. High performance, low-cost, and sustainable materials are sought for a wide range of energy technologies that could help us realize our net zero ambitions for carbon emissions. For example, these include thermoelectric materials for waste heat harvesting,[21,22] semiconductors for photovoltaic[23,24] and photoelectrochemical cells,[25,26] electrodes and electrolytes for fuel cells and batteries,[27] and permanent magnets for motors and turbines.[13,14] Across all of these technologies, grain boundaries in materials play a key role in controlling performance yet often their specific effects are not fully understood presenting an obstacle to materials discovery and optimization.

This review article aims to highlight how first principles materials modeling and electron microscopy techniques can provide atomic scale insight into the properties of grain boundaries in energy materials. Moreover, we will show how the highly complementary nature of these two approaches means more can be achieved by their application in tandem than alone. Such methods can be applied successfully to materials relevant to a very wide range of energy applications, but in this review, we focus attention mainly on materials for photovoltaic applications where grain boundaries impact the dynamics of electrons and holes under photoexcitation.[4,23,28,29] The schematic in Fig. 1 shows examples of the complementary information first principles modeling and electron microscopy can provide on the atomic structure and properties of grain boundaries. Scanning transmission electron microscopy (STEM) can provide two-dimensional (2D) atomically resolved images of the structure of grain boundaries providing the grain boundary plane can be oriented parallel to the electron beam.[30–33] This leaves the structure in the third dimension uncertain in some cases as it is not always possible to obtain images for different orientations to resolve the 3D structure. However, first principles modeling can be used to identify stable grain boundary structures in 3D, and compared to the experimental images, the atomic structure of the grain boundary can be fully determined.[32,34–39] This then brings the added benefit that a wide range of other properties (such as electronic structure,[32,34,39] magnetic structure,[15] defect properties,[35–38] and spectroscopic properties[40]) can be predicted using the experimentally validated structure. Some of these properties are more challenging to probe experimentally at the atomic scale and so this complementary interaction between the approaches is extremely powerful. Electron backscatter diffraction (EBSD) can provide information on the crystalline phases and local orientations of individual grains in a polycrystalline material,[41–43] which can be useful for developing and validating first principles models. The recombination of electrons and holes excited by an electron beam (cathodoluminescence) can also provide information on the optoelectronic properties of grain boundaries.[44,45] The emission spectra resulting from radiative electron–hole recombination can be detected and mapped spatially throughout a polycrystalline material. The variation in intensity near grain boundaries can be modeled to extract information on electrostatic barriers for electrons and holes resulting from charged defect segregation and associated band bending. This information too can be linked back to first principles models of defect segregation to grain boundaries and calculations of associated space charge regions.[46] The examples given above highlight the complementarity of first principles modeling and electron microscopy for understanding the properties of grain boundaries at the atomic level. When brought together with information from other materials characterization techniques, such as charge transport[47–49] and photoluminescence spectroscopy,[29,50,51] one can obtain detailed insight into the impact of grain boundaries on the device performance. This understanding can then be deployed to better optimize the performance of materials as well as to identify new promising materials for next-generation devices.

This review will introduce the key concepts and approaches for first principles modeling and electron microscopy characterization of grain boundaries. Although we focus mainly on photovoltaic materials, many of the methods and ideas are applicable to a far wider range of materials. As such, it should serve as a useful introduction for any researcher looking to better understand how theory and experiment can work together to better understand the properties of polycrystalline materials.

The remainder of the review is structured in the following way. We start by reviewing the key definitions, terminology, and concepts related to grain boundary defects in Sec. II. There is no attempt here to be comprehensive as there are already many good books on the subject that go into finer details. Our aim is only to provide a basic introduction sufficient to be able to understand methods for modeling and characterizing grain boundaries. In Sec. III, we provide an introduction to first principles materials modeling and electron microscopy approaches for grain boundary defects. Again, we will aim to provide sufficient information on the methods to enable the reader to engage
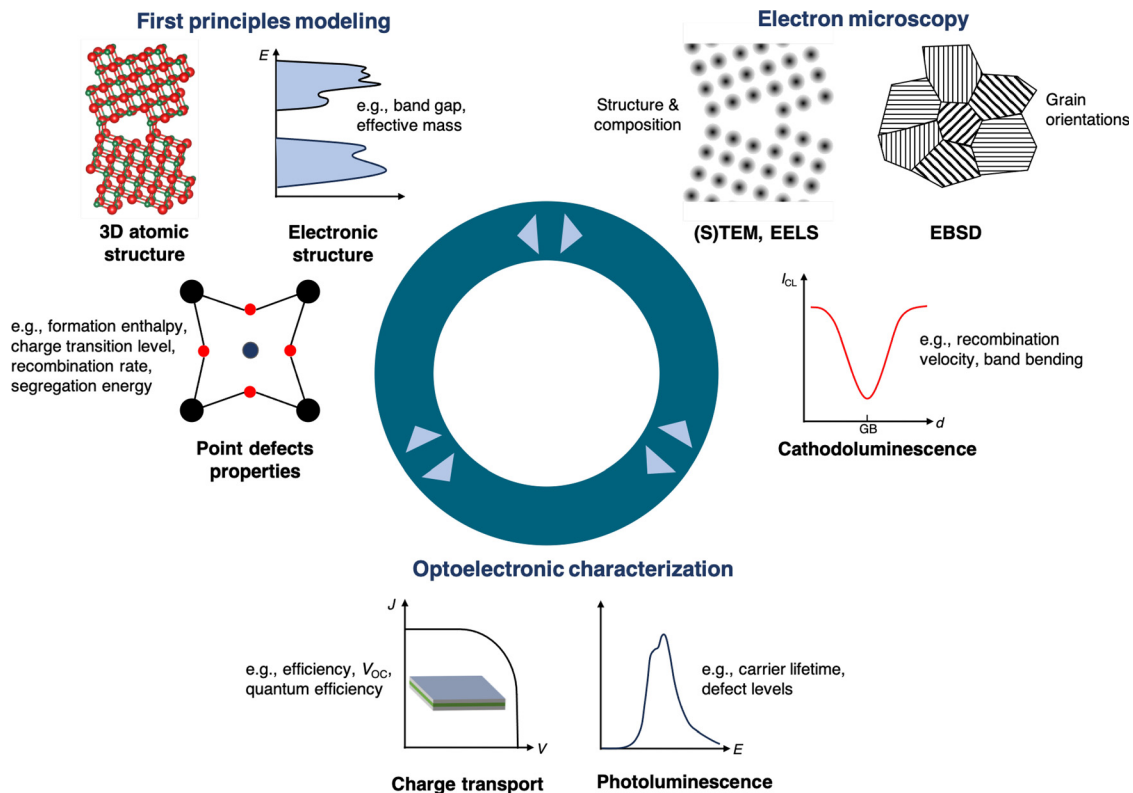
31 January 2024 08:53:32

FIG. 1. Examples of structural and optoelectronic properties of grain boundaries accessible with first principles modeling and electron microscopy techniques (the main focus of this review). There is strong complementarity between these approaches and opportunities for information exchange (often iterative) in both directions to deepen understanding of the atomistic structure of grain boundaries. When combined with other optoelectronic characterization techniques (e.g., charge transport or photoluminescence), this understanding connects the properties of grain boundaries to device performance (a photovoltaic device in this example).

with the research in this area and refer to appropriate literature for more detailed information on the methods beyond the scope of this review. In Sec. IV, we discuss a number of energy materials as case studies and describe how first principles materials modeling and electron microscopy have been used to provide deeper insight into the structure and properties of grain boundary defects. The impact of grain boundaries in various semiconductor thin films on the device performance is highlighted in Sec. V. In Sec. VI, we discuss our perspective on some of the key challenges for research in this area and suggest a number of future directions. Finally, in Sec. VII, we summarize and conclude the review.

II. GRAIN BOUNDARY DEFECTS
A. Description of grain boundary defects

Grain boundaries are two-dimensional defects that delineate two crystalline regions (or grains) in a polycrystalline material.[1] Even in the common situation that two adjacent grains share the same crystal structure, grain boundary defects are expected in general, since the grains may have different crystallographic orientation as well as an arbitrary translation with respect to each other. Boundaries between the grains may exhibit a complex shape in real materials. However, computational simulations and experimental imaging of polycrystalline materials suggest that in order to locally minimize energy grain

boundaries often adopt faceted shapes with extended regions separated by planar grain boundaries.[31,52,53] The orientational relationship between two grains meeting at a planar grain boundary can be uniquely defined in terms of five angles: two angles for each grain to describe its orientation (often more conveniently expressed in terms of Miller indices) and an angle to describe the rotation of one grain with respect to the other about an axis perpendicular to the grain boundary plane [Fig. 2(a)]. Two types of high-symmetry planar grain boundary have been the focus of many computational and experimental studies due to their suitability for atomistic modeling and imaging: symmetric tilt and twist grain boundaries.[1] Tilt grain boundaries are formed at the interface between two grains with orientations that differ only by rotation about a common tilt axis parallel to the grain boundary plane [Fig. 2(b)]. In symmetric tilt grain boundaries, the orientations of the two grains either side of the grain boundary plane are mirror symmetric (although not necessarily the structure since rigid body translations can break this symmetry). For example, mirror symmetric rotation of grains terminating on the {100} planes about the [001] tilt axis gives rise to a series of symmetric tilt grain boundaries with decreasing tilt angle: (210)[001] (310)[001] (410)[001], etc. (where the first set of Miller indices specifies the termination plane of the grain and the second set specifies the tilt axis). In the small angle limit, tilt grain boundaries can be viewed as arrays of one-dimensional edge dislocations.[54]
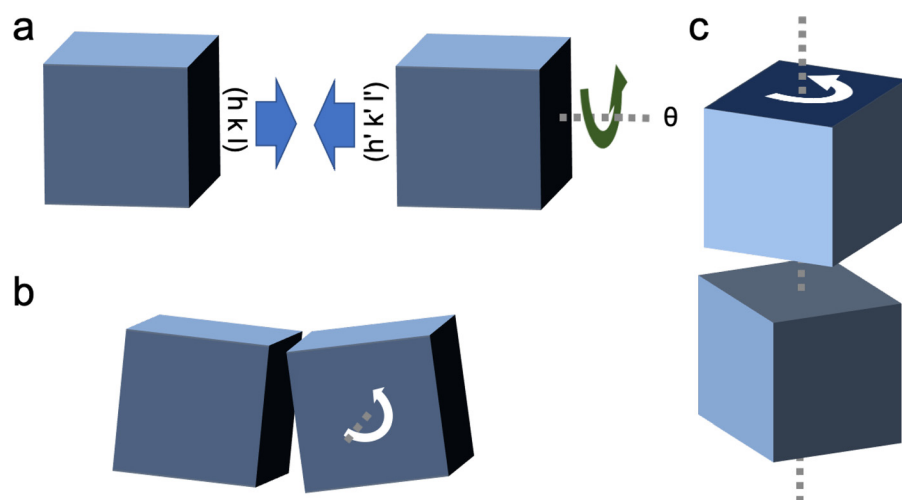
FIG. 2. (a) Illustration showing how the crystallographic orientation of a planar grain boundary can be defined by specifying the terminating planes of the two grains, e.g., using Miller indices (hkl) and (h′k′l′), together with a rotation by an angle θ about an axis perpendicular to the grain boundary plane. (b) A pure tilt grain boundary is formed by adjoining two grains with equivalent terminations but with arbitrary rotations of the grains about an axis parallel to the grain boundary plane. (c) A pure twist grain boundary is formed by adjoining two grains with equivalent terminations but with arbitrary rotations of one grain with respect to the other about an axis perpendicular to the grain boundary plane.

A pure twist grain boundary is an interface between two grains with symmetrically equivalent grain orientations but a finite rotation about an axis perpendicular to the grain boundary plane [Fig. 2(c)]. Twisted interfaces between two-dimensional (2D) graphene flakes have recently become a subject of intense interest owing to the possibility to realize exotic and tunable electronic phases.[55] In this case, the 2D nature of the material means the structure of the graphene layers is only weakly perturbed. More generally, however, twist grain boundaries exhibit significant and complex reconstructions, particularly in semiconducting and ionic compounds where it is required to eliminate energetically unfavorable "wrong bonds," such as oxygen ions in close proximity in oxide materials.[56] While pure tilt and twist grain boundaries are often observed experimentally and are convenient for modeling, more generally planar grain boundaries can have a mixed tilt-twist character.

Historically, there has been much interest in developing general criteria for understanding the stability of certain grain boundary orientations in materials observed experimentally or computationally.[52] This led to the development of ideas, such as the coincidence site lattice (CSL),[57] and alongside Miller indices to specify grain boundary orientation, it is common in the literature to quote the Σ number. The Σ number specifies the ratio of the number of lattice points in the crystal to the number of coincident lattice points in the CSL. Low values of Σ have high site coincidence, and therefore, it might be expected the mismatch in grain orientations at the grain boundary could be more easily accommodated resulting in a higher stability. Indeed, there is experimental and computational evidence that some special low Σ grain boundaries have on average lower formation energies (in particular Σ3 twin boundaries).[52,58] However, the grain boundary formation energy is determined by atomic structure and bonding, and so Σ alone cannot be used to predict grain boundary structure, stability, or properties. The concept of "structural units" is often useful for understanding the structure and properties of grain boundaries at the atomistic level.[59,60] The idea is that across various types of grain boundaries in materials one often encounters frequently occurring local arrangements of atoms (or structural units). For example, for low angle tilt grain boundaries, the relevant structural units are corresponding edge dislocation cores.[30] Such structural units can in some sense be considered as the building blocks of more general grain boundaries. Indeed, one can predict the structure of low symmetry and therefore long period grain boundaries if one knows the structural units for the short period grain boundaries that delimit the misorientation.[61,62] This approach was more recently extended to consider structural units corresponding to metastable grain boundary structures to improve predictive accuracy.[63]

The brief introduction to grain boundary defects given above will be sufficient to engage with the material presented in the remainder of this review. However, we recommend the excellent book by Sutton and Ballufi for a more comprehensive discussion.[1]

B. Point defect segregation

All materials contain point defects. The presence of some finite concentration of intrinsic defects (such as vacancies, interstitials, and antisites) is guaranteed by thermodynamics. In practice, most materials also contain extrinsic defects, for example impurities introduced accidentally during synthesis or exposure to the environment as well as dopants added deliberately in order to modify materials properties. In general, point defects in grain boundary regions will have different stability and properties to corresponding defects in the bulk region of grains. If a particular type of point defect is more stable at a grain boundary than in the bulk, there is a thermodynamic driving force for those defects to segregate there.[64–67] Conversely, if the defect is less stable at the grain boundary, they will be repelled from the grain boundary. Whether or not that happens also depends on the activation energy for diffusion and the temperature.[68,69] Importantly, the presence of grain boundaries can themselves also have a significant effect on defect diffusion, with defect diffusion along and across grain boundaries significantly modified compared to the bulk crystal (enhanced or suppressed).[70] Aside from the local difference in structure and properties at the grain boundary itself, grain boundaries often introduce a strain field that permeates inside the grains (often several nanometers) that may also modify point defect properties.[71] The result of these effects is often an inhomogeneous variation of point defect concentrations in the vicinity of grain boundaries and a corresponding modification of material properties.

For an individual isolated defect in a given charge state (relative to the host material), one can define the segregation energy E_{seg} as the

31 January 2024 08:53:32

difference in formation energy between a defect in the bulk region and a site in the grain boundary. The segregation energy can be a useful quantity for assessing segregation of point defects in grain boundaries. It is important to recognize that grain boundaries will have a range of inequivalent sites to which point defects may segregate each characterized by different segregation energies. So it is common to see a distribution of segregation energies even for a single well-defined grain boundary.[72,73] In practice, there will be a wide distribution of grain boundary types as well, each with distributions of sites for point defect segregation. Beyond the dilute defect limit, segregation of defects can induce significant structural modifications of grain boundaries with associated modification of properties.[74] More generally grain boundary regions can host nanoscale material phases not seen in the bulk of grains due to an interplay of defect segregation and the boundary conditions imposed by the bulk grains. In some cases, such intergranular phases may even be amorphous.[75]

In semiconducting and insulating materials, the presence of a bandgap means that defects can often adopt a number of different charge states and their presence even in small quantities can significantly affect the position of the Fermi level and optoelectronic properties. Even for a perfect infinite single crystal, intrinsic defects, such as vacancies, interstitials, or antisites, can be present which act as donors or acceptors and move the Fermi level toward the valence or conduction band, respectively (making the material n- or p-type). In practice, materials are often non-stoichiometric and contain unwanted impurities as well as deliberately introduced dopants leading to much higher concentrations of defects and stronger effects on electronic properties. In equilibrium, the formation energy and hence the concentration of charged intrinsic defects depend on the Fermi energy. Therefore, the equilibrium population of defects and corresponding Fermi energy is determined self-consistently for given concentrations of extrinsic defects such that the system remains overall electrically neutral.[76]

In a polycrystalline material, the picture becomes much more complex. As discussed above, defects can segregate to grain boundaries giving rise to a spatially inhomogeneous variation of defect concentrations (and in some cases local charge density) throughout the material. However, the temperature dependent mobility of different defect species and the heterogeneity of grain boundary properties make it very difficult to predict the self-consistent local equilibrium the material will settle into for given processing conditions. However, one can gain some useful insight by considering simple one-dimensional models of defect segregation to grain boundaries that include screening of any charge density variations by free charge carriers (via the Poisson equation).[5] This is important for understanding the effect of grain boundaries on charge carrier transport and recombination and is discussed in more detail in Sec. II C.

C. Charge carrier transport

1. Effects of grain boundaries on charge-carrier transport

Charge carrier mobilities of polycrystalline materials are often significantly decreased compared with single crystals due to increased scattering of charge carriers at grain boundaries.[6] This increased scattering can have a number of different causes with their relative importance often controlled by the type of material, its synthesis, and processing. For example, in semiconductors, these can include the trapping of

charge carriers at poorly coordinated atoms at the grain boundary, modification of interfacial electronic structure, and band structure mismatch across the grain boundary planes (particularly important for materials with highly anisotropic band structures). Since all materials contain point defects, which often segregate to grain boundaries this brings a further source of charge carrier scattering. For many semiconductors, this is often the dominant mechanism as such defects can be charged leading to the introduction of electrostatic barriers to electrons or holes traveling between grains. This effect was nicely demonstrated by Stützler and Queisser[77] for p-type silicon bicrystals. Their as-grown and hydrogen treated bicrystals exhibited charge transport properties similar to those in Si single crystals. However, after segregation of impurity atoms to the grain boundaries induced by thermal annealing, the conductance across the grain boundary plane was observed to decrease. This decrease could be explained by the appearance of a barrier for one type of charge carrier (electrons or holes) at the grain boundary planes as a result of the bending of the conduction-band and valence-band edges induced by segregated impurities.

Each grain boundary plane in a polycrystalline semiconductor exhibits a certain density of point defects segregated from the grain interiors. These defects can be either charged or charge-neutral and result, as an ensemble, in a net-charge density localized at the grain boundary plane (we refer here to localized defects with a specific charge state). If the net-doping density in the semiconductor is sufficiently large, free charge carriers (electrons and holes) may redistribute around this localized charge density, leading to the formation of space-charge regions and to corresponding lateral changes of the electrostatic potential via Poisson's equation (see Fig. 3). Seto[5] derived expressions for barrier heights at semiconductor grain boundaries (see Fig. 3) for various net-doping densities (N_A) and described that two regimes need to be considered, for a given density of defects (trap states) at the grain boundary planes, N_{gb}, and average distance between grain boundary planes, d_{grain}. The charge states of the grain boundary traps are changed upon carrier trapping.

Regime I: Low net-doping densities ($d_{grain}N_A < N_{gb}$) such that the grain interiors become essentially depleted of free charge carriers and the grain boundary traps are partially filled. For this situation, the barrier height can be expressed as

$$\varphi_B = \frac{e^2 d_{grain}^2 N_A}{2\varepsilon_0 \varepsilon_r},\tag{1}$$

where φ_B depends linearly on N_A and ε_r is the relative permittivity of the material.

Regime II: High net-doping densities ($d_{grain}N_A > N_{gb}$) where all grain boundary trap states are filled and the remaining free charge carriers screen effectively the charged defects at the grain boundary plane, leading to the formation of space-charge regions around the planar defects. Now, φ_B is inversely proportional to N_A,

$$\varphi_B = \frac{e^2 N_{gb}^2}{2\varepsilon_0 \varepsilon_r N_A}.\tag{2}$$

We note that in Eqs. (1) and (2), there is a factor of 2 in the denominator, which in Ref. 5 is wrongly given as a factor of 8. We can see from Fig. 4 that for small ($< 10^{15}$ cm^{-3}) and high ($\geq 10^{17}$ cm^{-3}) net-doping densities, the barrier heights (for the given N_{gb} and d_{grain} values) reach negligible values at room temperature. Also, whenever

Grain boundaries in a *p*-type semiconductor

Redistribution of free charge carriers around charged GB
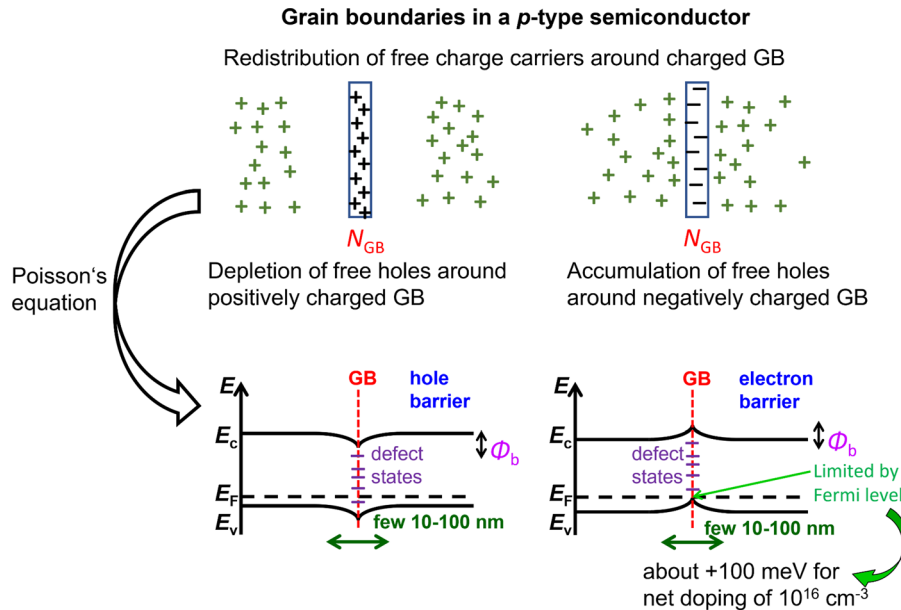

FIG. 3. Schematics of charged grain boundaries in a *p*-type semiconductor (for an *n*-type material, a similar scenario with free electrons instead of free holes can be drawn). We note that the charge density N_{gb} is the net charge density from all the individual (positively and negatively) charged defect densities at the grain boundary plane. Depending on whether N_{gb} is negative or positive, the free charge carriers (mainly holes) redistribute, forming space-charge regions by depletion or accumulation around the grain boundary plane. Via Poisson's equation, this redistribution results in a corresponding change in the distribution of the electrostatic potential, which eventually leads to the band bending depicted in the schematics. For the downward band bending, there is no lower limit; however, there is an upper limit for the upward band bending at the grain boundary plane in a *p*-type semiconductor, since the band bending must not cross the Fermi level. Since the *p*-type doping density is about the density of free holes in thermodynamical equilibrium, $n_h = N_V \exp\left[(E_F - E_V)/k_B T\right]$, the Fermi level E_F would be about 100 meV above the valence-band maximum E_V for an assumed net-doping density of 2×10^{16} cm^{-3} and an effective density of states in the valence band of $N_V = 1 \times 10^{18}$ cm^{-3}.

high-injection conditions are given, no barriers are formed since free electrons and free holes exhibit the same densities. Therefore, barriers at grain boundaries typically only make sense for low-injection conditions and for net-doping densities of about 10^{15}–10^{16} cm^{-3}. The
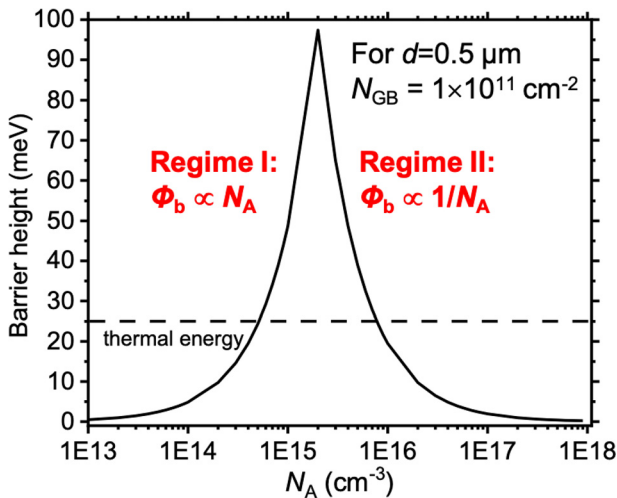

FIG. 4. Barrier at the grain boundary as a function of the net-doping density N_A. The assumed average grain size d_{grain} and (charged) defect density N_{gb} at the grain boundary plane were 0.5 μm and 1×10^{11} cm^{-2}, respectively. The thermal energy at room temperature, $k_B T \approx 25$ meV, is indicated by a horizontal, dashed line.

conductivity across a grain boundary plane and correspondingly also the current (at an applied voltage) is proportional to $\exp(-\varphi_B/k_B T)$, i.e., the charge carriers can overcome the barriers by thermionic emission.[5] For the reasons mentioned, grain boundaries have often a negligible effect on the charge-carrier transport and, thus, on the charge-carrier collection in a solar-cell device. Much stronger impacts of grain boundaries can be expected on the voltage via enhanced nonradiative recombination, as will be outlined in Sec. II C 2.

2. Recombination at grain boundaries

Greuter and Blatter[6] highlight that whether a grain boundary plane exhibits an excess charge density or is charge-neutral, which basically means that whether or not a barrier is present at a grain boundary, enhanced nonradiative (Shockley–Read–Hall) recombination almost always occurs at the planar defect. Shockley–Read–Hall recombination is facilitated by the trapping of electrons and holes at localized defect levels (associated with point defects) within the bandgap and recombination rates depend on the cross sections for charge carrier trapping and on the concentration of the defects (both of which are often enhanced at grain boundaries).[78–80] The recombination velocity was introduced in order to quantify the recombination of minority-charge carriers at semiconductor surfaces several decades ago.[81] This concept can be transferred to a grain boundary plane in a polycrystalline material assuming this plane is an internal surface. The recombination velocity of a surface or a grain boundary in a semiconductor contains basically two contributing features used for describing

the impact on free charge carriers: a recombination term specifying the nonradiative recombination via an ensemble of point defects on the surface or at the grain boundary plane (Shockley–Read–Hall recombination) and a term containing the upward or downward band bending, forming barriers or driving charge carriers to the surface or grain boundary plane. Brody and Rohatgi[82] suggested accordingly the following expression for the grain boundary recombination velocity s_{gb} in a p-type semiconductor:

$$s_{gb} = N_{gb}\sigma_{gb}v_{th}\exp(-\varphi_B/k_BT), \qquad (3)$$

where σ_{gb} is the effective capture cross section and v_{th} the thermal velocity of electrons. We note that a term similar to the prefactor in Eq. (3), $N_{gb}\sigma_{gb}v_{th}$, appears in the expression for the nonradiative bulk lifetime, $\tau_{bulk,nonrad} = (N_T\sigma_Tv_{th})^{-1}$ (where N_T and σ_T denote the density of traps and their capture cross section).[78,83] A similar term also appears in the expression for the recombination velocity at a dislocation, $g = N_d\sigma_dv_{th}$ (where N_d and σ_d denote the density of defects on a dislocation core and their capture cross section).[84] Moreover, capture and recombination rates of excited minority-charge carriers can be very different from one another at grain boundaries due to differences in defect level energies and phonon properties (see Ref. 85 for an example of grain boundaries in TiO_2).

For very small and very large N_A values, the barrier heights φ_B become much smaller than k_BT at room temperature (about 25 meV), and thus, the exponential term in Eq. (3) can be neglected. In the intermediate regime for N_A, the recombination velocity is a product of a prefactor $s_{gb,0} = N_{gb}\sigma_{gb}v_{th}$ that describes the nonradiative, Shockley–Read–Hall recombination via the trap states N_{gb}, and the exponential term $exp(-\varphi_B/k_BT)$ that exhibits an effective lever via the upward or downward band bending φ_B (forming electron or hole barriers in a p-type semiconductor) and that, thus, changes the s_{gb} value substantially (often by several orders of magnitude). Since the excess charges at various grain boundaries can generally be assumed to be both, positive or negative, correspondingly varying, negative, or positive φ_B values can be expected. It is convenient to simplify Eq. (3) using the prefactor $s_{gb,0}$,

$$s_{gb} = s_{gb,0}\exp(-\varphi_B/k_BT). \qquad (4)$$

It is important to note that the exponential function in Eqs. (3) and (4) can be neglected for very small and very large N_A values and also under high-injection conditions as no relevant barriers are present at grain boundaries. This is because under such conditions, the densities of free electrons and free holes are equal, and therefore, no redistribution of free charge carriers and no band bending at the grain boundaries occur. This fact becomes relevant when measuring the recombination velocity at grain boundaries by means of, e.g., luminescence analyses, as detailed further below in Sec. III A.

Following the discussion in Ref. 86, the lifetime of minority-charge carriers at grain boundaries bordering a cubically shaped grain with n passivated grain boundary faces can be written as

$$\tau_{gb} = \frac{d_{grain}}{(6-n)s_{gb}}, \qquad (5)$$

where the value of n depends on the situation in the polycrystalline material under consideration and may take all values from 0 to 5. The grain boundary lifetime τ_{gb} is one component of the effective lifetime

τ_{eff} for minority charge carriers in a complete semiconductor device. Assuming, e.g., a solar cell with a solar absorber and two selective contacts, τ_{eff} can be expressed using Matthiessen's rule[87] via,

$$\frac{1}{\tau_{eff}} = \frac{1}{\tau_{bulk,rad}} + \frac{1}{\tau_{bulk,nrad}} + \frac{1}{\tau_{interface}} + \frac{1}{\tau_{gb}} + \frac{1}{\tau_{disloc}}, \qquad (6)$$

where $\tau_{bulk,rad}$, $\tau_{bulk,nrad}$, $\tau_{interface}$, and τ_{disloc} are the lifetimes with respect to radiative and nonradiative recombination in the semiconductor bulk as well as to nonradiative recombination at the interfaces between absorber and contacts and at dislocations. Eventually, τ_{eff} can be linked to the open-circuit voltage V_{oc} of this assumed solar-cell device via[88]

$$V_{oc} = \frac{2n_{id}k_BT}{e}ln\left(\frac{G_L\tau_{eff}}{n_{p0}}\right), \qquad (7)$$

where G_L is the total generation rate of charge carriers integrated throughout the absorber volume under illumination, n_{id} is the diode-ideality factor, and n_{p0} is the equilibrium, unilluminated electron concentration in the p-type absorber (in a heterojunction device). Equations (4)–(7) depict the connection between microscopic material properties and the macroscopic device performance and, thus, can be employed when analyzing the impact of grain boundaries on the performance of semiconductor devices.

3. Passivation of grain boundaries

Having discussed recombination at grain boundaries in detail in Sec. II C 2, we can define a clear prerequisite for the passivation of a grain boundary using Eq. (4). In this equation, s_{gb} must always decrease significantly in the case of a successful passivation of a grain boundary.

Typically, the term describing the Shockley–Read–Hall recombination, $N_{gb}\sigma_{gb}v_{th}$, becomes decreased in the case of grain boundary passivation, i.e., the effective defect density N_{gb} and their capture cross section σ_{gb} are decreased. Decreases in the barrier heights at grain boundaries alone are not sufficient, since in this case, the median value $s_{gb,0}$ remains the same. In Sec. V, we will discuss in specific case studies whether evidence for passivation of GBs via appropriate treatments of polycrystalline absorber materials can indeed be found.

III. METHODS
A. Experimental

Characterizing the grain boundaries found in real-world materials is challenging due to their atomic-scale nature. There are only a few methods that allow for direct measurements of the properties of grain boundaries, and these methods often lack the resolution to exclusively probe the atoms making up the grain boundary.[89–91] Despite this, there is a large body of work focused on directly imaging grain boundaries with atomic resolution and correlating them with macroscopic measurements, which has led to a strong understanding of the physical properties of many types of grain boundaries in several different families of energy materials.[15,30–33,74]

This section contains an overview of some of the most commonly used techniques employed to study the properties of grain boundaries in energy materials. We will focus on electron microscope-based techniques that enable atomic resolution imaging of grain boundaries and introduce some of the complementary techniques that make it possible

to correlate atomic positions with macroscopic properties. Many techniques require specialized sample preparation methods, so we will discuss these, as well as the limitations associated with each method.

1. Electron microscope-based studies of grain boundaries

a. TEM-based techniques. Since grain boundaries are by definition atomic in nature (although their impact can be measured over nanoscopic distances), it is necessary to be able to resolve individual atoms in order to obtain a clear real-space image of a grain boundary. The most commonly used techniques to achieve this level of resolution are all based around the application of high-energy electrons in transmission electron microscopy (TEM). When accelerated with several hundred kilovolts, the wavelength of electrons reaches well below the distance between two atoms, thus enabling the imaging of individual atoms, allowing us to obtain direct information about the exact atomic makeup of grain boundaries.[92]

These techniques are particularly useful in crystalline materials, since they can resolve boundaries between periodic, ordered structures very clearly,[93] but they can also be used to distinguish domains in amorphous materials, such as those used in organic photovoltaic devices. Additionally, TEM can visualize defects in crystalline materials, and the strong interaction between the electrons and the sample produces a wealth of signals that can be collected to determine chemical information with high resolution, as illustrated by Figs. 5(a) and 5(b).[31,93–95]

All TEMs are based on the design of an evacuated tube at high vacuum with an electron gun at one end (typically the top), a sample near the middle, various detectors below the sample, and electromagnets acting as lenses below and above the sample. Electrons are extracted from the gun using heat, an electric field, or a combination of the two, and the electrons are then accelerated with a high voltage, typically between 80 and 300 kV, and often passed through an energy filter to reduce the range of energies of the electrons. At these kinetic energies, the electrons travel near 80% of the speed of light and the wavelength of an electron wave is around 0.2 nm, which is smaller than the distance between two atoms, and individual atomic columns can, therefore, be distinguished.[92]

TEM is characterized by high electron energies relative to scanning electron microscopes (SEM, typically 0.5–20 keV), and the fact that the electrons pass through the sample to be detected below it. This means that the transmitted electrons carry information from the whole
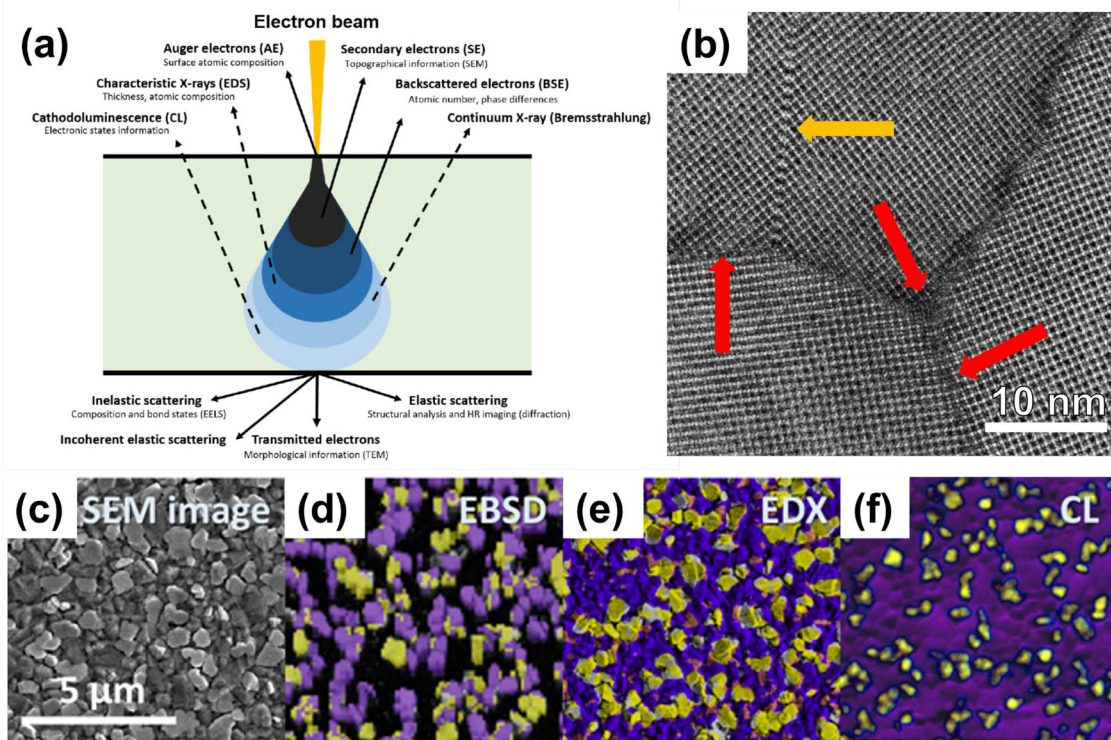
FIG. 5. Electron microscope-based techniques and their applications to crystalline photovoltaic materials. (a) Overview of the range of signals that can be generated and recorded when an electron beam interacts with a sample. Reproduced with permission from Rothmann *et al.*, Adv. Energy Mater. **7**(23), 1700912 (2017). Copyright 2017 John Wiley and Sons.[94] (b) Atomic-resolution scanning transmission electron micrograph of a thermally evaporated FAPbI$_3$ thin film showing a high-angle grain boundary, a triple junction, and a low angle grain boundary, as indicated by the red arrows from left to right, respectively, and an extended stacking fault, as indicated by the orange arrow. Reproduced with permission from Rothmann *et al.*, Science **370**, eabb5940 (2020). Copyright 2020 The American Association for the Advancement of Science.[31] (c) Scanning electron microscope image of a triple halide perovskite-type thin film and the corresponding (d) EBSD, (e) EDX, and (f) CL maps obtained from different areas to avoid beam-induced artifacts. The perovskite phase is highlighted by the purple color, and precipitated PbI$_2$ phases are highlighted by the yellow color. Reproduced from Abou-Ras *et al.*, J. Appl. Phys. **133**(12), 121101 (2023) with the permission of AIP Publishing.[64]

sample, but it also imposes some strict limitations in terms of sample dimensions and overall material stability. Since electrons are easily scattered within a material, samples must be very thin, often less than 100 nm, and ideally closer to just a few nm, in order to achieve atomic resolution imaging. Additionally, the high kinetic energies, and the electric charge, of the accelerated electrons often cause them to interact strongly with materials, causing electron beam-induced changes in the sample.[92] Many materials, like silicon and most metals, are very stable under high-energy electrons, whereas materials containing halides and/or organic/covalent bonds are susceptible to damage induced by the incoming electrons. In the case of hybrid metal halide perovskites, this effect is particularly pronounced and has led to great difficulty in characterizing the grain boundaries found in native films used for photovoltaic applications.[96]

Transmission electron microscopy is usually done either with a broad beam, where the electron illumination is distributed widely across the whole sample, or with a focused probe, where the electron beam is focused and scans across the sample in a raster pattern. Additionally, it is possible to scan a narrow, parallel beam, often called a pencil beam, across the sample, combining the two beam geometries in one setup. Each beam geometry is useful and can provide different, but complementary, information about the crystallography of a sample.

The two main ways to obtain crystallographic information from a material are either real space or diffraction imaging. Real space imaging involves various ways of measuring the intensity of the electrons passing through the sample, for example by a pixelated detector in broad beam bright-field TEM imaging, effectively taking two-dimensional "pictures" of the sample, or by an annular detector, measuring electrons scattered at a particular range of angles in annular dark field (ADF) imaging.

b. Electron backscatter diffraction (EBSD). Electron backscatter diffraction (EBSD) is a powerful tool for the determination of the local orientations and crystalline phases of individual grains in a polycrystalline material.[41] Since the orientations of two neighboring grains can be measured unambiguously, their misorientations can be calculated, from which the corresponding grain boundaries can be classified, as illustrated in Figs. 5(c) and 5(d). The technique is most commonly found in scanning electron microscopes and is based on detecting the diffraction patterns formed by inelastically scattered electrons that are diffracted subsequently at lattice planes in a crystalline sample. These inelastically scattered and diffracted electrons reside on the surfaces of (Kossel) cones, and when a planar detection device is applied, these electron waves result in two parallel lines (Kikuchi bands) for each family of lattice planes at which diffraction occurs. The ensemble of bands from the various diffraction events makes up the EBSD pattern, in which the bands exhibit a symmetry corresponding to the symmetry of the crystal at which the electrons diffracted. By knowing the crystal structure, it is possible to calculate the range of possible backscattered diffraction patterns, and by matching the measured patterns to the calculated ones, it is possible to determine the orientation of a crystal with typical spatial resolutions of tens of nanometers.

Grain boundaries exhibit five degrees of freedom in a three-dimensional space, three for the misorientation and two for the orientation of the grain-boundary plane. Thus, from two-dimensional EBSD maps, only the traces of grain boundaries (i.e., a rough estimate

of the crystallographic planes of the grain boundaries) can be extracted, apart from the misorientations between neighboring grains.[42] For a complete characterization of all five grain-boundary parameters, three-dimensional EBSD needs to be employed.[43]

It should be noted that EBSD lacks the resolution to image the exact atomic distribution at grain boundaries and cannot give direct information about the chemical environment found across them (although complementary techniques can provide this information). In spite of this, it can be used to provide excellent averaged information about the boundaries, which can be used to give experimental support to computational methods.

EBSD has certain inherent limitations to its use. Sample preparation is essential to avoid artifacts, which can be caused by charging at the sample surface or by plastic deformation of the near-surface region. As such, the sample should ideally be conductive and grounded, as with other SEM samples, but the surface should also be free from plastic deformation and very flat. This is often achieved by polishing the sample finely, by plasma etching, or by milling samples with focused ion beams (FIB), which can introduce their own artifacts by damaging or changing the sample during the preparation. As such, EBSD is commonly used to study sturdier materials, like metal and silicon, and its use has been limited in organic and hybrid perovskite solar cells.

c. Sample preparation. Preparing samples that allow for the detailed study of grain boundaries can be challenging, and particular care must be paid to ensure that the sample carries the information found in the corresponding real-life material. In general, samples for grain boundary studies come in two categories: idealized samples and real-life samples.

Idealized samples are samples formed to contain a particular grain boundary orientation, which can then be studied extensively, often in the form of bicrystals, where two known crystal orientations are combined directly. The interface then forms a known grain boundary, which eliminates the aspect of determining the grain boundary orientation being studied and simplifies the characterization notably.[97,98] The obvious limitation to this method of preparing the sample is that it is "artificial" and may, therefore, not represent the structure found in real-life samples, which makes it difficult to use bicrystals for complex structures. In particular, since there is only a single orientational grain boundary present, bicrystal samples cannot give information about the dynamic formation mechanisms that take place when materials crystallize, and they cannot provide information about what happens when crystals of a wider range of orientations intersect. That being said, bicrystals have been used widely to study many materials, including silicon.

Real-life samples are samples either cut from a piece of material that would be used in a real-life application or prepared using a similar method but to specifications that fit the technique being used. Examples of this are focused ion beam-milled cross section lamellae of stable solar cell materials for high-resolution TEM, where a small slice is cut out of a bulk of a device or material, and reduced to fit the dimensions required for HR-TEM.[32] The FIB process can introduce artifacts in some materials, but it has been used widely to study the intrinsic properties of grain boundaries in materials such as silicon and $Cu(In,Ga)Se_2$. Some materials, like hybrid perovskites, are too beam-sensitive for FIB milling to be a reliable option (although much work is currently being done to manage this), and other alternatives, like

depositing a thin film directly onto a TEM grid using solution processing or thermal evaporation, have been developed and used with great success.[96] Since real-life samples are prepared using similar methods to those used to prepare actual devices, their properties are often very similar to those found in real devices, adding an extra layer of value to real-life samples.

With the right sample preparation methods, it is possible to create well-defined samples for systematic studies of grain boundaries in a wide range of energy materials. Both idealized and real-life samples can provide important information about the properties of materials on a microscopic level, which can often lead to a more thorough understanding of the macroscopic properties of energy materials.

d. Spectroscopy techniques. We have previously discussed some of the signals generated when electrons interact with a sample, such as x-rays and visible light photons. These secondary signals can be used to extract information about the chemical composition and electronic structure and properties of a material and are a very useful complement to real-space and diffraction imaging techniques. Many electron-to-sample interactions are often needed to generate a measurable amount of secondary signals, meaning that these techniques require electron doses that can be several orders of magnitude above the safe threshold doses of many sensitive materials, which can lead to beam damage. However, when recorded carefully under the appropriate conditions, these signals can be immensely useful.

In this section, we will describe three different types of EM-based spectroscopy techniques: energy dispersive x-ray spectroscopy (EDX or EDS), electron energy loss spectroscopy (EELS), and cathodoluminescence (CL).

EDX is a technique in which the characteristic x-rays emitted by a material as a result of electron interactions are collected and analyzed. Energetic electrons from the incident electron beam can knock out electrons from core shell states in a material; electrons bound in higher orbitals can relax into the empty, energetically lower states, and x-rays with energies corresponding to the energy difference between the core-shell states are emitted. Since each element has a unique combination of possible orbitals that the electrons can move from and to, the range, or spectrum, of x-rays emitted by each element is unique, or characteristic, to the material. By measuring this spectrum of emitted x-rays, it is possible to identify the presence, distribution, and relative abundance of elements in a sample. Depending on the type of sample and microscope, the resolution can range from millimeter-sized scans divulging micrometer-sized domains, to scans determining the material composition with atomic resolution.[92,99]

In TEM, EDX can reach sub-angstroms spatial resolution,[99] whereas in SEM, it can be as low as 10–20 nm, as illustrated in Fig. 5(e).[100] Essential for achieving high spatial resolutions in SEM–EDX elemental-distribution maps is the use of small beam energies (few keV) and low-energy x-ray lines (i.e., in the order of 100 eV or smaller). Such lines exhibit small, inelastic mean-free paths, and thus, the information volume (i.e., the effective volume in the analyzed material from which characteristic x-rays are emitted and reach the EDX detector) is rather small, eventually leading to high spatial resolutions. Consequently, the spatial resolutions in EDX elemental-distribution maps are different for different x-ray lines.[64]

Electron energy loss spectroscopy relies on measuring the number and associated energies of electrons passing through a sample.

As the electrons pass through a sample, some of them will undergo inelastic scattering, losing energy and randomly changing direction slightly as a result. If the electrons are emitted with a narrow range of energies, the change in energy can be correlated with a range of possible causes, including phonon interactions, band transitions, plasmon excitation, inner shell radiation, and Cherenkov radiation. Additionally, since higher electrons can knock out inner-shell electrons, and the combination of energies required to ionize inner shell electrons is characteristic to each element, it is possible to use EELS to determine the elemental composition of a material, in some cases with atomic resolution.[92]

EELS requires a high number of electrons to generate a high enough signal to noise ratio for statistically significant spectra to be obtained, but typically, the dose needed is lower than that required for EDX. EELS is also particularly useful for studying lighter elements and can even be used to determine the oxidation state of these elements. As such, it has been used widely to study catalysts, battery materials, and inorganic solar cell materials, but the dose required is still generally too high for hybrid perovskite materials.

Cathodoluminescence (CL) is a technique in which the visible light photons emitted from a surface as a result of excitation by electrons are collected, making it possible to study the emission spectra and intensities of materials, as illustrated in Fig. 5(f).[64] It is analogous to photoluminescence (PL), except for that the electron–hole pairs are generated by electrons rather than by light. It is most commonly found in SEM, where a concave mirror is placed above the sample and a hole in the mirror allows the electron beam to reach the sample surface. As the luminescence is emitted from the sample, it is collected in the mirror and aimed toward a detector, which is usually either a spectrometer, a simpler light intensity detector, or both. Since the intensity of the luminescence emission is related to the radiative recombination rate from a material, locations of enhanced nonradiative recombination, e.g., grain boundaries or dislocations, can be identified via decreased CL intensities. The evaluation of various low-energy peaks in the CL spectra from materials allows for the characterization of defect states. The highest peak energy in a CL spectrum, resulting from the band-band transition, is not necessarily identical with the bandgap energy of the material; this is because this CL peak may be energetically shifted with respect to the bandgap energy.[101]

Since CL makes use of luminescence emission upon the excitation of electron–hole pairs by the incident electron beam, the injection level has to be regarded when interpreting the CL results (the radiative recombination is different under high-injection and low-injection conditions). In terms of the spatial resolutions of CL analyses, not only the excitation volume of electron–hole pairs, but also the diffusion of the excited charge carriers prior to their radiative recombination has to be considered. Nevertheless, at times, high spatial resolutions with length scales much smaller than that of the excitation volumes and diffusion lengths in the investigated material are demonstrated.[102] Such results can be explained by the fact that charge carriers recombine already at the position of the incident electron beam, and thus, especially in highly luminescent materials and when using effective CL recording systems, the luminescence intensity is rather high at this incidence position.

2. Measurement of the recombination velocity s_{gb}

At submicrometer length scales, the only technique able to provide values for the recombination velocities s_{gb} at individual grain

boundary planes is cathodoluminescence. The approach depicted here (see Fig. 6) was proposed by Mendis et al.[103] It is based on the assumption that free charge carriers diffuse to the grain boundary planes, where they experience enhanced nonradiative recombination by point defect segregated to grain boundaries (with densities N_{gb}) (Fig. 6). Thus, the luminescence intensity can be expected to decrease from the grain interiors to the grain boundary plane for grains adjacent to the grain boundary. Indeed, this is what CL signals across grain boundaries in polycrystalline semiconductor thin films look like. In Fig. 6, this situation is depicted for a ZnO/CdS/Cu(In,Ga)Se$_2$/Mo/glass solar-cell stack. Using the CL intensity in the grain interior, I_{GI}, as a reference value, the difference in CL intensity $I(x)$ as a function of the distance x from the grain boundary plane can be expressed as

$$ln\left(\frac{1 - I(x)}{I_{GI}}\right) = ln\left(\frac{S}{S+1}\right) - \frac{x}{L}, \qquad (8)$$

where L is the effective diffusion length of the minority-charge carriers (electrons in a p-type semiconductor), and S is the reduced recombination velocity with $S = s_{gb}\tau_{bulk}/L$. Here, τ_{bulk} is the bulk lifetime within a grain. Equation (8) exhibits a linear form with the fit parameter L. The bulk lifetime τ_{bulk} needs to be measured by an additional analysis in order to determine the value of s_{gb} from the evaluation of the CL intensity distribution.

The determination of τ_{bulk} is not as straightforward as it seems. It is much simpler to measure the effective lifetime τ_{eff} via (e.g.,) time-resolved photoluminescence (TRPL). Nevertheless, we can obtain a good estimate of τ_{bulk} by using a simplified version of Eq. (6). Assuming that $\tau_{bulk}^{-1} \approx \tau_{bulk,rad}^{-1} + \tau_{bulk,nrad}^{-1} + \tau_{disloc}^{-1}$ and neglecting recombination at interfaces, this equation can be rewritten as

$$\frac{1}{\tau_{eff}} \approx \frac{1}{\tau_{bulk}} + \frac{1}{\tau_{gb}}. \qquad (9)$$

The approach for the determination of τ_{bulk} is as follows:

1. Measurement of τ_{eff} (e.g., by TRPL).
2. Measurement of the average grain size d_{grain} by electron back-scatter diffraction or from scanning electron micrographs.
3. Estimation of τ_{bulk} and τ_{gb} in Eq. (9).
4. Refinement of these values using the fact that τ_{bulk} is used in Eq. (8) to determine s_{gb}, and s_{gb} again is used in Eq. (5) to calculate τ_{gb}, which needs to agree with the estimated τ_{gb} value.

Thus, not only values for s_{gb} and τ_{gb} but also a rough estimate for τ_{bulk} are obtained. A prerequisite for the successful application of the presented approach is that in the region of interest, the average grain size is sufficiently large to extract appropriate CL linescans across grain boundaries. Since the spatial resolution of CL analyses for many
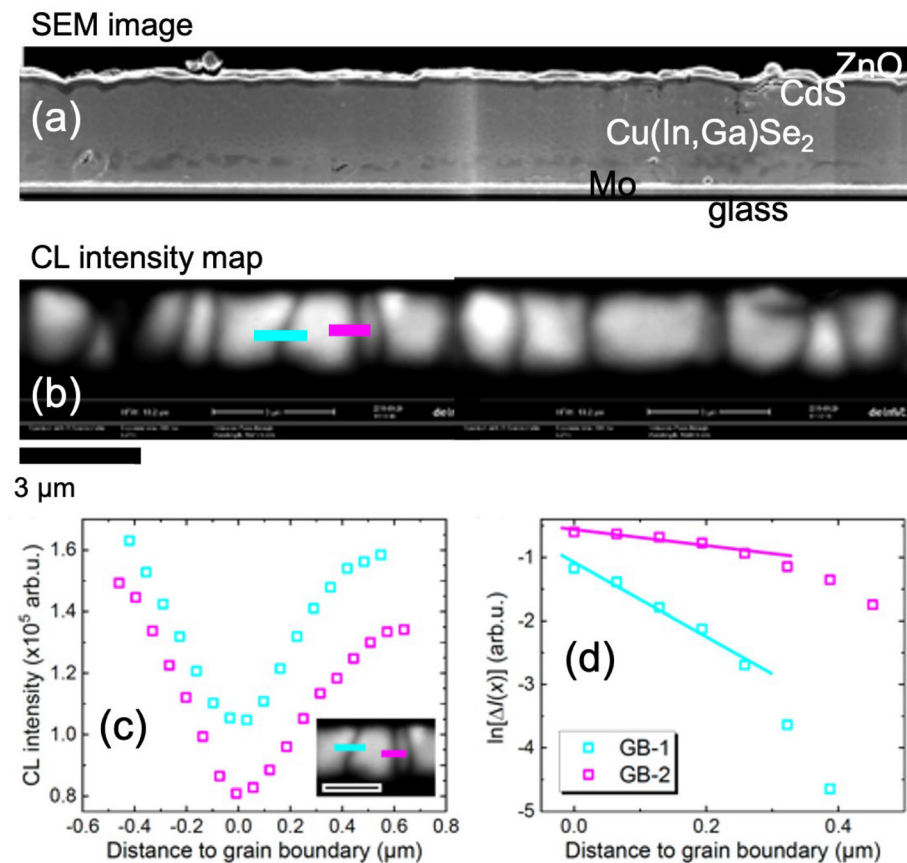
FIG. 6. (a) SEM image and (b) intensity distribution extracted from a hyperspectral cathodoluminescence (CL) image, both acquired on the identical area of a cross-sectional specimen prepared from a ZnO/CdS/Cu(In,Ga)Se$_2$/Mo/glass solar-cell stack. Along the blue and pink lines across the grain boundaries in (b), line-scans (c) were extracted (integration widths of 10 pixels each). (d) Difference in intensity as a function of the distance to the grain boundary plane, plotted in the semilogarithmic scale. Linear functions were fitted to the curves in (d).

semiconductor materials is roughly around 100 nm (always depending on the diffusion of excited charge carriers before their radiative recombination, which may be different at different measurement conditions and for different materials), the average grain size should be about few 100 nm.

The recombination velocities at the grain boundaries determined by cathodoluminescence can be simulated successfully using Eq. (4), as shown further below for grain boundaries in Si and $(Ag,Cu)(In,Ga)(S,Se)_2$. However, care is advised in the case of high-injection conditions during the cathodoluminescence characterization. Such conditions can be expected whenever the analyzed semiconductor material exhibits a low net-doping density of smaller than about 10^{15} cm^{-3} (for which high-injection conditions cannot be avoided) and for combinations of beam energies and beam currents that lead to high densities of generated electron–hole pairs (i.e., small beam energies and large beam currents). The consequence of high-injection conditions is that the density of free electrons and free holes is equal, leading to maximum values for the radiative recombination rate and thus, for the cathodoluminescence intensity. The resulting exponential decay of this intensity from the grain interiors to the grain boundary planes [Eq. (8)] becomes much larger than that for low-injection conditions, in addition to decreased bulk lifetimes with increased injection level,[50] suggesting very high recombination velocities. From cathodoluminescence experiments with various injection conditions, it is found that the difference between s_{gb} values determined under low-injection and high-injection conditions may be one to two orders of magnitude. Good indications for high-injection conditions during luminescence or other analyses of polycrystalline semiconductor materials are recombination velocities that vary only within one order of magnitude, i.e., Eq. (4) becomes $s_{gb} \approx s_{gb,0}$ (the s_{gb} values differ only slightly from one another for different grain boundaries). This finding agrees basically with discussions on this issue by Brendel.[104]

An alternative approach to calculate recombination velocities at grain boundaries from photoluminescence (PL) imaging was provided by Sio et al.[105] These authors modeled PL-intensity profiles across grain boundaries in two dimensions, for which s_{gb} is one of the fit parameters. Riepe et al.[106] as well as Stokkan et al.[107] reported the application of carrier density imaging (CDI) together with electron backscatter diffraction to determine recombination velocities at dislocations and grain boundaries in a combined manner from the obtained charge-carrier lifetimes.

Laser-beam-induced (LBIC) (e.g., Ref. 108) as well as electron-beam-induced-current (EBIC) measurements (see Refs. 109–111) have been employed for the determination of recombination velocities at grain boundaries. The evaluation of both techniques is based on the fundamental work by Donolato,[112] describing the diffusion of minority charge carriers in a polycrystalline semiconductor to the grain boundary planes, where they experience enhanced nonradiative recombination. As in the case of cathodoluminescence measurements, the injection levels in the investigated semiconductor material affected by the applied beam parameters in the LBIC and EBIC experiments have to be controlled carefully in order to be able to interpret the measured signals correctly.

B. Theoretical modeling

1. Grain boundary models

Computational modeling of the atomic scale structure and properties of grain boundaries in materials has a long history spanning

more than 50 years. The first examples in the early 1970s focused on the structure and stability of high symmetry grain boundaries in metals with interatomic interactions described by simple models such as the Morse potential.[113,114] In the following decades, the complexity and accuracy of interatomic potentials progressively improved allowing grain boundary modeling for a wider range of materials and properties. The 1980s saw the development of a range of more advanced interatomic potentials for metals, covalent semiconductors, and ionic materials. The embedded atom method[115,116] and related many-body potentials[117] provide a more accurate description of interatomic interactions in metals supporting numerous applications to grain boundaries still to this day. The earliest examples of successful comparison between computed and experiential grain boundary structures were for monatomic metals, e.g., the {112} twin grain boundary in Al with HRTEM[118] and [110] tilt grain boundary in Au.[119] More advanced models for covalent materials, such as Stillinger–Weber,[120] Tersoff,[121–123] and bond-order potentials,[124] were developed and subsequently applied to model tilt and twist grain boundaries in a wide range of materials.[125,126] In the 1980s, the first atomistic models of grain boundaries in ionic materials were produced with interionic interactions described using Buckingham potentials and the shell model to capture ion polarizability.[127,128] In the following decade, the first code specifically developed to model extended defects in materials using interatomic potentials, METADISE, was developed[129] and subsequently applied to model grain boundaries in a diverse range of ionic materials. As clear from this brief discussion, interatomic potentials have played a key role in modeling the structure and properties of grain boundaries, providing insight into the factors, which govern their stability, mechanical, and thermal properties as well as other more complex phenomena such as the segregation and diffusion of impurities and intrinsic defects. There has been an ongoing effort over the last half century to improve the quality of interatomic potentials including, for example, reactive potentials to describe changes in the oxidation state (e.g., as relevant for metal oxidation) as well as the more recent explosion of interest in machine learning potentials.[130] However, as such potentials become more complex so does their parameterization/fitting/training and care must be taken to ensure they are not employed outside of their domain of validity. Simulations of grain boundaries using interatomic potentials remain popular today, and with the power of modern supercomputers and highly parallelized simulation codes, they allow the simulation of systems containing millions of atoms and the modeling of dynamic processes that take place over long timescales.

As illustrated above, atomistic simulation of grain boundaries using interatomic potentials can be a very powerful technique particularly for predicting structure or modeling the dynamics of atoms; however, its major drawback is that it provides no direct information on the electronic properties of materials. For that, one needs to turn to a quantum mechanical method that explicitly considers the nuclei and associated electrons in materials. The first examples of this type of approach employed the tight-binding method to study high angle tilt grain boundaries (hence requiring relatively small supercells) in semiconductors such as Si.[131] Subsequently, the wide availability of density functional theory (DFT) codes and increases in computer power has enabled DFT models of grain boundaries in materials covering a wide range of materials and with supercells routinely containing hundreds of atoms.[132,133] Nowadays, it is possible to model grain boundary

31 January 2024 08:53:32

properties using approximations that go beyond local or semi-local approximations for exchange and correlation, such as hybrid functionals,[134] in order to more accurately describe electronic properties.

There are two general types of approach to the atomistic modeling of grain boundaries in polycrystalline materials. One can either attempt to model a given volume of polycrystalline material containing multiple grains and grain boundaries or instead attempt to model a single planar grain boundary with well defined orientation. As an example of the former approach, one could consider a molecular dynamics simulation of a large volume of material and gradually cool the system down from a high temperature with randomly oriented seed grains to nucleate grain growth.[135] Alternatively molecular dynamics could be used to simulate the growth of a polycrystalline film on a substrate. In both cases, the very large number of atoms required (typically many thousands) requires computationally efficient interatomic potentials for these approaches to be practical. An advantage of these approaches is that one can obtain a wide distribution of grain boundary types with complex features such as grain boundary junctions included in the model. On the other hand, the complexity of the models makes systematic investigation of grain boundary properties beyond the atomic structure challenging (especially electronic properties).

Approaches for modeling a single planar grain boundary are closely analogous to those widely used for modeling surfaces. One starts by creating a two-dimensionally periodic slab containing a grain of finite thickness (thick enough that the center of the slab is bulklike) terminated by two surfaces of defined orientation. By adjoining two such slabs, a grain boundary defect is created at the interface [see Fig. 7(a)]. This approach is analogous to the experimental bicrystal approach discussed above. There are then several options available for dealing with the boundary conditions on the other sides of the slabs: (1) create a three-dimensionally periodic supercell with the length in the direction perpendicular to the grain boundary plane chosen such that the two remaining surfaces are separated by a vacuum gap such that interactions between the surfaces are negligible [see Fig. 7(b)]. (2) Create a three-dimensionally periodic supercell with the length in the direction perpendicular to the grain boundary plane chosen such that the two remaining surfaces form a second grain boundary [see Fig. 7(c)]. (3) Attach much thicker two-dimensionally periodic slabs to each side to represent the grains. The atoms in these regions (region II) would typically be treated more simply (for example, held rigidly in bulk-like positions) in the spirit of the Mott–Littleton approach for modeling point defects [see Fig. 7(d)]. Approaches 1 and 2 are suited for modeling using interatomic potentials or DFT. The former may be preferred if approach 2 would result in two inequivalent grain boundaries in the supercell (for example, for an asymmetric grain boundary). Option 3 has been implemented in the METADISE code and applied extensively for modeling ionic materials where long range polarization effects are important and not easy to capture in a three-dimensionally periodic supercell approach.

In principle, one can construct models for any planar symmetric tilt, twist or mixed grain boundary. However, a major practical consideration is the area of the two-dimensional supercell required. Very low angle tilt and twist grain boundary have large areas meaning that slabs of sufficient thickness can easily contain many thousands of atoms (often prohibitive for DFT approaches). For asymmetric grain boundaries, the situation is even more challenging. One can construct
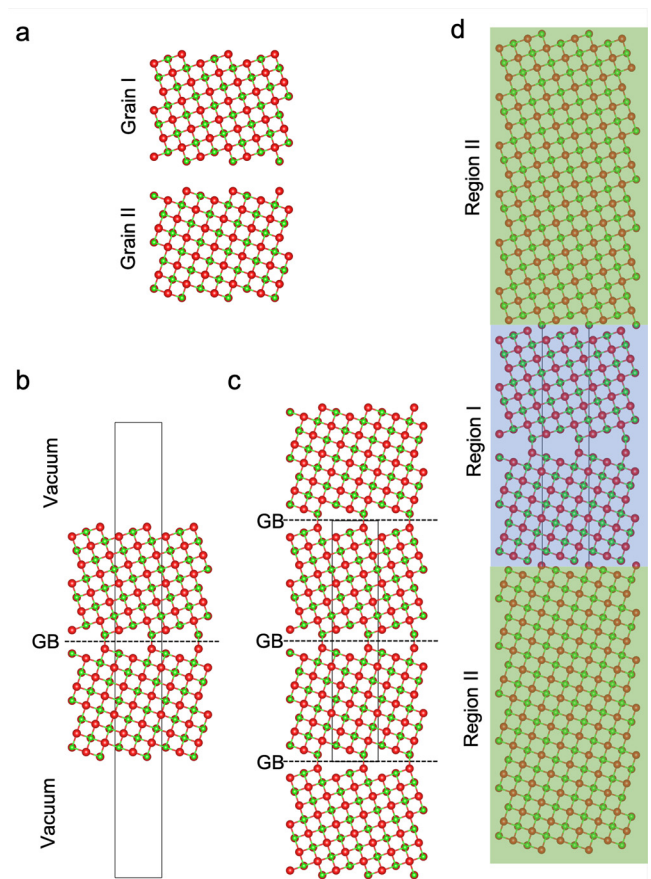

FIG. 7. (a) Two-dimensionally periodic slabs representing grains of finite thickness can be adjoined to model a planar grain boundary. Here, we show example slabs for the symmetric (310) grain boundary in a rock salt crystal. (b) A single grain boundary can be modeled in a three-dimensionally periodic supercell by adjoining the two slabs and choosing the length of the supercell lattice vector in the direction perpendicular to the grain boundary plane chosen such that the two remaining surfaces are separated by a vacuum gap. (c) Alternatively, the vacuum gap can be removed to generate a supercell with two (in this case equivalent) grain boundaries. (d) Another approach which allows longer range strain and polarization effects to be captured is to describe the interface as two-dimensionally periodic (parallel to the interface) but much thicker finite grains. The grains can be separated into different regions (regions I and II), which could be described at different levels of theory to minimize computational cost.

commensurate supercells for asymmetric grain boundaries, but they too are often too large for practical calculations. Alternatively, by applying a small amount of strain to the slabs parallel to the grain boundary, one can construct smaller commensurate supercells for asymmetric grain boundaries. However, whether this is feasible (for a given level of theory) depends on the specific orientation of the asymmetric grain boundary being considered. A number of tools are available for the construction of planar grain boundary models such as METADISE,[129,136] grain boundary code,[137] Aimsgb,[138] and GBMaker.[139]

With a planar grain boundary model constructed, the next step would be determining the most stable structure and computing associated properties (see Secs. III B 2–III B 4). For that one needs to choose

a level of theory for describing the interatomic interactions. As discussed above, interatomic potentials can be a very computationally efficient approach and in some cases also very accurate. However, potentials are rarely designed and parameterized with grain boundary structures in mind and care must be taken that the potential is not pushed outside of the limits of its accuracy. Nevertheless, they can be a valuable tool for studying very large numbers of different grain boundary structures, grain boundary structures involving large numbers of atoms, as well as helping to find the most stable grain boundary structure by prescreening candidates prior to application of a higher level of theory. On the other hand, for understanding optoelectronic, chemical, or magnetic properties, a quantum mechanical approach is required. DFT offers an excellent balance between computational cost and predictive accuracy, and calculations on systems with up to 1000 atoms are routinely accessible with current computational resources. Approaches like tight-binding DFT and linear scaling DFT can enable grain boundary calculations on systems with many more atoms, while higher levels of theory, such as GW, become accessible for systems with up to a few hundred atoms.

2. Finding stable grain boundaries

Determining the most stable atomic configuration for a given planar grain boundary is a very challenging problem as there are many degrees of freedom to consider including the position of atoms in the grain boundary region, the local stoichiometry of the grain boundary region, and the relative translation between the two grains. For the following, we will assume we are employing a three-dimensionally periodic supercell with two equivalent grain boundaries as described in Sec. II B 1. However, similar approaches are employed for other grain boundary models. In general, the aim is to minimize the Gibbs free energy of formation per unit area,

$$\gamma = \frac{1}{2A}\left(G_{gb} - \sum_i n_i \mu_i\right), \qquad (10)$$

where G_{gb} is the Gibbs free energy of the grain boundary supercell, i labels atomic species, μ_i is the chemical potential, n_i is the number of atoms of species i, and A is the cross-sectional area of the grain boundary (the factor of 2 arises in this case as there are two grain boundaries in this supercell). In practice, the Gibbs free energy is usually approximated as the total energy (at 0 K), and for a stoichiometric supercell, there is no explicit dependence on the chemical potentials of the species since the sum on the right of Eq. (10) reduces to NE_{bulk}, where N is the number of formula units in the supercell cell and E_{bulk} is the total energy per formula unit for the bulk crystal. The usual approach to minimizing the free energy of formation with respect to stoichiometry is to consider a set of supercells with different compositions and minimize the total energy of each. Then, one can plot the dependence of the free energy of formation on chemical potential for different compositions in order to determine the most stable in different conditions. So, the challenge is reduced to finding the minimum energy of a supercell with fixed composition with respect to the position of all atoms near the grain boundary and translation of one grain with respect to the other (still a formidable challenge).

The gamma-surface method is a popular approach to tackle the above-mentioned problem (Fig. 8). The idea is to create initial grain boundary supercells for different intergrain translations (in general, both parallel and perpendicular to the grain boundary plane).

For example, one might consider all inequivalent translation vectors on a grid with a separation between points of 0.1 Å. Then, one employs standard energy minimization algorithms (e.g., conjugate gradients) to optimize each structure. The gamma-surface can then be computed, which gives the minimum formation energy for each in-plane translation, and the minimum of this surface is the most stable grain boundary structure. In applying this approach, it is often necessary to consider different possible grain terminations as well in order to identify the most stable grain boundary structure. There are also variations in the application of the method: for example, optimization only performed for a subset of the atoms in the system or constrained from optimizing in certain directions. Figures 8(b)–8(d) show examples of gamma-surface scans for symmetric and asymmetric grain boundaries in anatase TiO_2. This type of approach often works well providing that structural distortions (with respect to the bulk crystal) are well localized near the grain boundary plane and relatively mild. However, for large area grain boundary supercells, the systematic grid search can quickly become computationally prohibitive.

In cases where the structure near the grain boundary plane exhibits more significant deviations with respect to the bulk crystal, the gamma surface approach is unlikely to identify the most stable structure (or perhaps even a reasonable metastable one). For such problems, one must turn to alternative methods more suited to challenging global optimization problems. For example, molecular dynamics and simulated annealing have been employed to search for the structures of twist grain boundaries in silicon identifying more stable ordered structures.[126] Minima-hopping methods have also been adapted and applied to identify stable structures of symmetric and asymmetric tilt boundaries in polycrystalline silicon.[140] Particle swarm optimization methods have been employed to identify the structures of grain boundaries in rutile TiO_2[141] as well as *ab initio* random structure searching.[142] Genetic algorithm approaches have been used to model grain boundaries in $SrTiO_3$.[143] These are just a few examples, and almost any global optimization approach can be adapted to study grain boundaries. The main challenge with these approaches is that they are often very computationally expensive as the total energy of many different configurations must be computed in order to properly explore the multidimensional potential energy surface. As a result, they are often employed in conjunction with interatomic potentials, with approximate quantum mechanical treatments such as tight-binding, or with DFT only if the number of atoms and degrees of freedom in the supercell is small enough.

If electron microscopy images of the grain boundary are available, it is often possible to assess consistency with the predicted atomic structure by directly over-laying the atomic coordinates on the experimental image. However, for a more reliable comparison, it is possible to use the predicted structure as input for an electron microscopy image simulation (Sec. III B 3). Figure 9 shows the predicted structure of a number of grain boundaries in anatase TiO_2 obtained using the gamma surface approach (see Fig. 8). In Fig. 9(c), the optimized structure of one of the grain boundaries is used to produce a simulated ABF STEM image and compared directly against a corresponding experimental demonstrating very good agreement. We note that a number of studies have shown that it is not always the case that only the most stable structure is realized experimentally. Often there are several low-formation energy grain boundary structures that can be observed reflecting the fact that real systems can fall into local metastable minima.
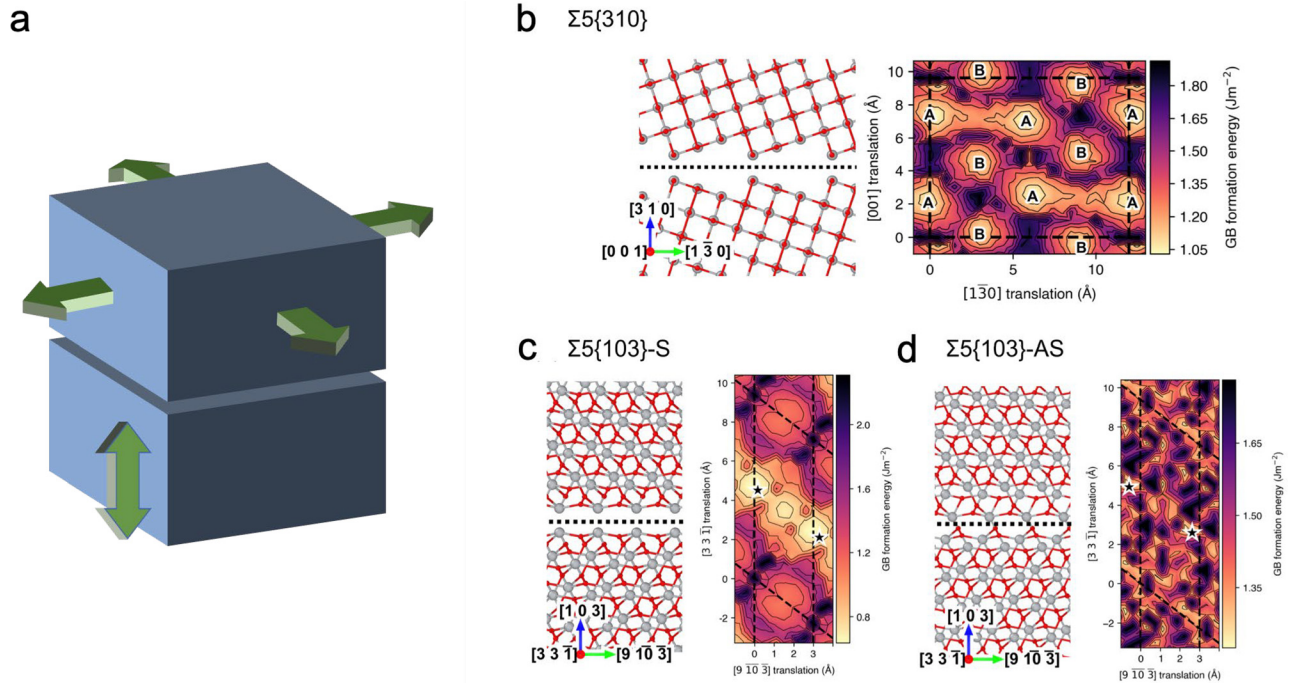
31 January 2024 08:53:32

FIG. 8. (a) One approach to identify the most stable planar grain boundary structure for given orientation is to consider different grain terminations and calculate the grain boundary formation energy, ꭓ, by energy minimization starting from different initial translations of one grain with respect to the other (in general, both parallel and perpendicular to the grain boundary plane). Initial structures and their associated rigid-body translation formation energy surfaces for the (b) [001]Σ5{310} grain boundary where uppercase A and B labeled on the energy surface plot indicate minima inequivalent minima, (c) [331]Σ5{103}-S grain boundary, and (d) [331]Σ5{103}-AS grain boundary where the star-shaped markers on the energy surface plot indicate the energy minima. Large gray spheres are titanium and small red spheres are oxygen, where the dotted line indicates the grain boundary plane separating each grain. Dashed lines on the energy surface plots mark the boundary of the simulation supercells used in the scans. Reproduced with permission from Quirk *et al.*, Nano Lett. **21**(21), 9217–9223 (2021). Copyright 2021 Authors, licensed under a Creative Commons Attribution (CC BY) License.[150]

3. Simulating electron microscopy

The interpretation of transmission electron microscopy (TEM) images is complicated by the fact that they are two-dimensional projections of a three-dimensional structure. First-principles models do provide insight, but comparing a computer-rendered image of atomic positions with an experimental image is not always straightforward, in part because the experimental image depends strongly on the specific parameters of the microscope and detectors. Producing the simulated image that corresponds to a computational model provides far more quantitative—and convincing—comparisons with experiment. One such method that allows the simulation of TEM images is the multislice method, which shall be described in this section.

The electrons used in TEM are sufficiently energetic that a precise description would require the relativistic Dirac equation. However, a simple approach that yields a reasonable description is to substitute the relativistic electron mass and wavelength in the non-relativistic time-independent Schrödinger equation (TISE). Then, we can write the TISE for this system (using Hartree atomic units) as

$$\left(-\frac{1}{2\gamma}\nabla^2 - V(\boldsymbol{r}) \right)\Psi_f(\boldsymbol{r}) = E\Psi_f(\boldsymbol{r}), \tag{11}$$

where $V(\boldsymbol{r})$ is the potential due to the specimen, $\gamma = \left(1 - \frac{v^2}{c^2}\right)^{-\frac{1}{2}}$ is the Lorentz factor for an electron with velocity v, and $E = \left(\frac{4\pi^2}{2\gamma\lambda}\right)$ is the

energy of an electron assuming all processes are elastic. The full wavefunction of the relativistic electron, $\Psi_f(\boldsymbol{r})$, is described by

$$\Psi_f(\boldsymbol{r}) = \exp\left(\frac{2\pi i z}{\lambda}\right)\varphi(\boldsymbol{r}), \tag{12}$$

where z is the Cartesian direction normal to the sample, i.e., in the direction of travel of the wave, and $\varphi(\boldsymbol{r})$ is a factor describing the portion of the wavefunction that varies slowly in z. Given the fact that the incident electrons have very high velocity in z, λ is very small, and $\varphi(\boldsymbol{r})$ varies very slowly in z we can note that

$$\left|\frac{\partial^2 \varphi}{\partial z^2}\right| \ll \left|\frac{1}{\lambda}\frac{\partial \varphi}{\partial z}\right|. \tag{13}$$

Then, Eq. (11) can be simplified through a rearrangement of terms (e.g., see Ref. 144) to obtain an approximate TISE for fast electrons moving as a first-order differential equation of the following form:

$$\frac{\partial \varphi(\boldsymbol{r})}{\partial z} = \left(\frac{i\lambda}{4\pi}\nabla^2_{xy} + i\sigma V(r)\right)\varphi(\boldsymbol{r}), \tag{14}$$

where $\nabla^2_{xy} = \frac{\partial^2}{\partial x^2} + \frac{\partial^2}{\partial y^2}$ and $\sigma = \frac{2\gamma\lambda}{4\pi}$ is the interaction parameter. This form is referred to as a high-energy approximation or paraxial approximation to the TISE.
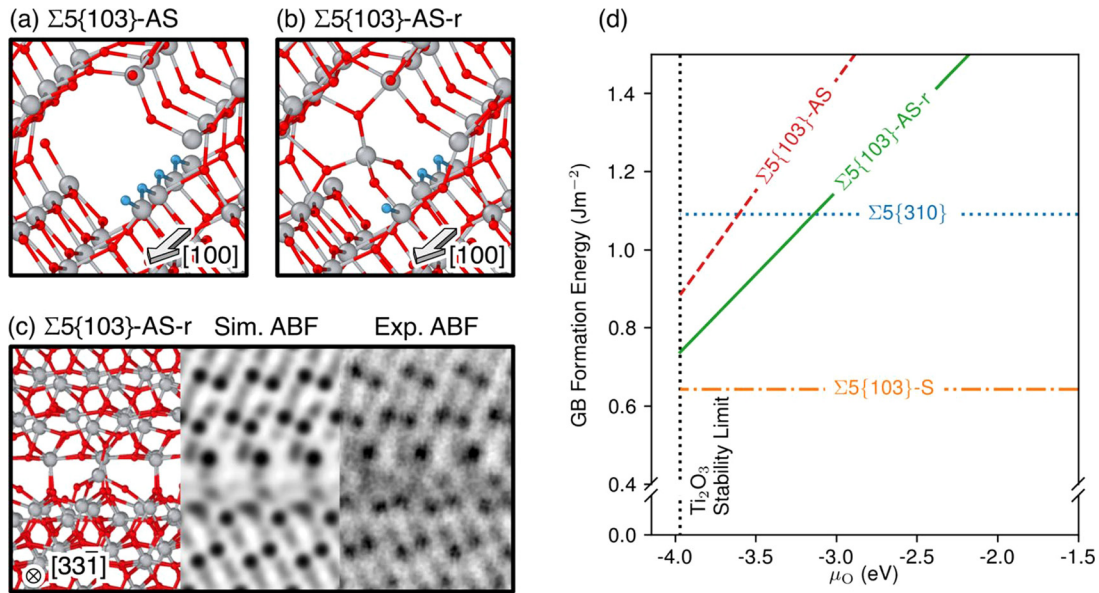
FIG. 9. Structural models of the (a) Σ5{103}-AS and (b) Σ5{103}-AS-r grain boundaries. Large gray spheres are titanium, small red spheres are oxygen, and bridging O atoms have been highlighted in blue. Projection indicated by arrows in the bottom right of the panels. (c) Structural model of the Σ5{103}-AS-r grain boundary with corresponding simulated and experimental ABF STEM images. (d) Formation energies of the grain boundaries, as a function of the oxygen chemical potential, μ_O, showing that, in the O-poor limit, the Σ5{103}-AS-r grain boundary has a similar formation energy to the Σ5{103}-S grain boundary. Note that the full range of μ_O up to the oxygen-rich limit of $\mu_O = 0.0$ eV is not shown. Reproduced with permission from Quirk *et al.*, Nano Lett. **21**(21), 9217–9223 (2021). Copyright 2021 authors, licensed under a Creative Commons Attribution (CC BY) License.[150]

The multi-slice solution to Eq. (14) opts to break the problem down into small specimen slices. Instead of solving across all z, the problem is integrated from z to $z + \Delta z$, where Δz is the width of a slice. It can then be shown (see Ref. 144) that $\varphi(r)$ takes the following form:

$$\varphi(x, y, z + \Delta z) = \exp\left(\frac{i\lambda\Delta z}{4\pi}\nabla_{xy}^2\right)t(x, y, z)\varphi(x, y, z) + O(\Delta z^2),$$

(15)

where $t(x, y, z)$ is the transmission function for the designated slice of the specimen, given by

$$t(x, y, z) = \exp\left(i\sigma\int_z^{z+\Delta z} V(x, y, z')dz'\right).$$

(16)

Defining the problem in this way effectively treats the specimen as a series of planes separated by vacuum with a thickness of Δz (Fig. 10). This approximation may appear quite severe, but the errors introduced by the multi-slice method can be reduced through careful placement of slices. Ideally, each slice would contain one plane of atoms such that each slice contains an averaged potential of one atomic plane. Then, the propagation through vacuum is a reasonable model for the propagation of the electron beam through the interstitial regions between the planes.
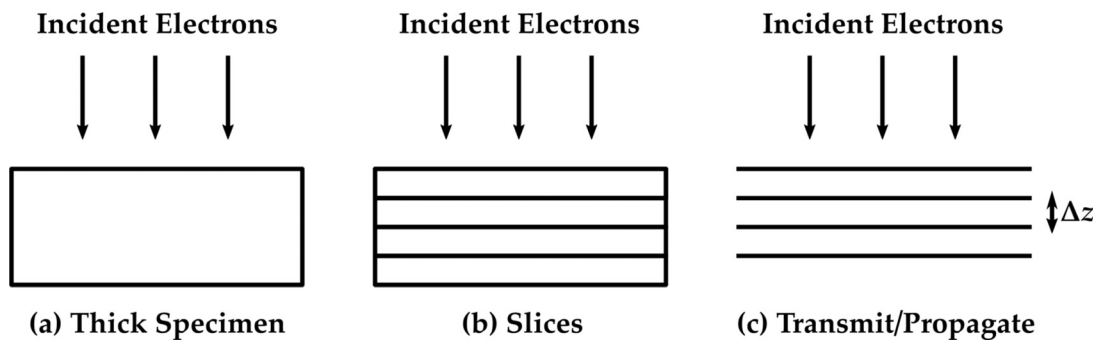

FIG. 10. Diagrams showing (a) the full specimen, (b) the specimen separated into thin slices, and (c) how each slice involves transmission through a slice, followed by propagation through vacuum of thickness Δz.

The potential that the electron beam interacts with, $V(x, y, z)$, is the Coulomb potential of the nuclei and the electrons. From first-principles calculations, it is possible to obtain this potential directly from the converged charge density for a given geometry. In practice, however, it is common to employ an independent atom model, which neglects the effects of bonding and treats the potential as being a simple superposition of atomic potentials. Such an approach is justified by the fact that the scattering is dominated by the atomic core (especially for heavy atoms) and has the added advantage of easily allowing the simulation of images from models obtained from classical methods, which will contain no information regarding the charge density. There are various codes available for carrying out multi-slice simulations, such as QSTEM[145] and abTEM,[146] both of which have interfaces with the Python Atomic Simulation Environment package.[147]

4. Property calculations

Once a stable grain boundary structure has been determined (and possibly confirmed through complementary experimental imaging as described above), a wide range of associated grain boundary properties can be calculated and quantitatively compared to corresponding bulk properties. Characterization of the spatial variation of properties near extended defects at the atomic scale is often very challenging using experimental methods alone, but by combining experiment and modeling deep and valuable insight into the role of grain boundaries in determining the properties of polycrystalline materials can be provided.

As well as predicting grain boundary formation energy and atomic structure close to the grain boundary plane (which can be compared directly to experimental images, e.g., from STEM), an optimized atomic model can also provide additional information on the longer range strain field associated with the grain boundary. The spatial extent and magnitude of the strain field can have a significant impact on defect segregation and diffusion as well as on electronic properties. Predictions can also be compared with differential phase contrast imaging. Another useful property of grain boundaries that is straightforward to calculate from an optimized model is the excess volume. The grain boundary excess volume is defined as the additional volume per unit area of the grain boundary compared to the volume of the same quantity of material in a bulk crystal. Grain boundaries typically have lower density in the vicinity of the interface (associated with dislocation-core-like features) and together with the longer range strain field lead to a positive excess volume. The excess volume has long been considered as one of the driving forces for defect segregation; the idea being that the additional space at grain boundaries can more easily accommodate the relaxation field around point defects. The average excess volume in polycrystalline metals has been measured by high-precision difference dilatometry[148,149] and compared to high-throughput calculations on a large number of grain boundary types to help explain differences in excess volume between materials.[53]

Methods for modeling grain boundaries that include an explicit quantum mechanical treatment of the electrons (such as tight-binding or DFT) allow the electronic structure of grain boundaries to be investigated. For example, the electronic density of states (DOS) projected onto different regions of the system can be calculated, or a two-dimensional band structure calculation can be performed to identify the nature of the interfacial bands introduced by the grain boundary. Often this analysis is performed for three-dimensionally periodic supercells containing one or two planar grain boundaries (as described in Sec. II B 1) since these can be constructed with a small enough number of atoms that quantum mechanical approaches are feasible. If such a supercell contains sufficiently thick grains, the center of the grains will have a bulk-like structure and the DOS or band structure projected onto this region will be almost indistinguishable from that of a perfect bulk crystal. The grain thickness that is required depends on the material and the specific grain boundary (with its associated strain field), but typically >15 Å is sufficient. With this bulk reference established, the DOS or band structure projected onto the grain boundary region can be computed, analyzed, and compared. Grain boundaries can introduce a number of different perturbations to the electronic structure of a bulk crystal, including shifts in the energies of core and semi-core states, modification of the energies and dispersion of bands (both occupied and unoccupied) as well as introduction of localized states in the band gaps of semiconductors and insulators (for example, associated with dangling bonds). For magnetic materials, electronic structure calculations also provide information on the magnetic ordering of the material, which can be modified in the vicinity of extended defects.[15]

The modification of electronic structure at extended defects affects corresponding spectroscopic properties, and in principle, this also provides an experimental avenue for probing grain boundaries. For example, core loss EELS can provide information on the elemental composition of grain boundaries with close to atomic resolution. Although more challenging, core loss EELS can also be used to distinguish different oxidation states [e.g., Ti^{3+} or Ti^{4+} in TiO_2 (Ref. 150)] and low loss EELS can provide information on the vibrational properties of grain boundaries.[151] Interpreting EELS spectra quantitatively in this way is very challenging but significantly aided by first principles calculations.[152,153] Excitation spectra relevant to other spectroscopies, such as XPS, UPS, and UV/optical absorption, can also be computed using first principles methods.[154]

While characterization of strain fields and excess volume can provide indirect information on the impact of grain boundaries on point defects, explicit consideration of defect segregation and associated properties is needed to provide a complete picture. To compute the segregation energy for point defects (Sec. II B), one can simply compare the total energy of a defect located in the bulk region of the supercell (i.e., the center of a grain) and one located at the grain boundary. There will be many possible grain boundary sites, which must be considered in order to identify those that are most stable. In general, the formation energy of a defect X with charge q with respect to the ideal crystal is defined as

$$E_f(X^q) = E(X^q) - \sum_i n_i \mu_i + q E_F, \qquad (17)$$

where $E(X^q)$ is the total energy of the grain boundary supercell containing the defect X^q, i labels atomic species, μ_i is the chemical potential, n_i is the number of atoms of species i, and E_F is the Fermi energy. Interatomic potential approaches are usually restricted to considering defects in a fixed charge state with respect to the host crystal, whereas for quantum mechanical approaches, multiple charge states may be accessible (for example, in semiconductors and insulators). In such cases by plotting the variation of formation energy with electron Fermi energy for different defect charge states, one can identify charge transition levels (CTLs), the Fermi energy for which the most stable charge state of a defect changes. The position of defect CTLs within the gap

31 January 2024 08:53:32

plays a critical role in processes such as charge trapping and electron–hole recombination. It is also possible to quantify the impact of such defects on recombination processes, either by computing recombination rates by mapping the problem onto an effective one-dimensional system and calculating corresponding vibrational wavefunctions and Hamiltonian matrix elements[85] or by direct simulation of the electron and hole dynamics by nonadiabatic molecular dynamics.[155]

IV. CASE STUDIES I: ATOMISTIC STRUCTURE OF GRAIN BOUNDARIES BY MICROSCOPY AND SIMULATION

A. Antimony sulfoselenides

Antimony selenide (Sb_2Se_3) and related sulfoselenide materials have seen a recent surge of interest for application as solar absorbers for thin film photovoltaic and photoelectrochemical cells. They offer a number of advantages including strong absorption ($>10^5\,cm^{-1}$), optimal band gaps, binary stoichiometry as well as relatively low cost. Despite being relatively unexplored compared to other established and emerging materials (around 1000 research articles published by the end of 2021[156]), there are already multiple reports of PV device efficiencies in excess of 10%.[157–159] This rapid progress has been attributed both to the quasi-one-dimensional (1D) crystal structure of these materials as well as to features of their electronic structure, which suggest they might be intrinsically tolerant to both point and extended defects.

The crystal structure of Sb_2Se_3 (here we consider the Pbnm space group[160]) consists of 1D $(Sb_4Se_6)_n$ ribbons oriented along the [001] direction. The bonding between ribbons is comparatively weaker with significant (but importantly not exclusively) van der Waals character. It was suggested that grain boundaries in such materials would be intrinsically benign since they would preferentially form on planes parallel to (001) without introduction of deleterious dangling bond defects commonly found in other semiconductors.[160] However, in practice, most Sb_2Se_3 films consist of columnar grains with preferential {211} and {221} orientation in the growth direction.[34,160–165] As a result, the 1D ribbons are expected to be oriented at angles of ~40 deg to the growth direction with grain boundaries that must inevitably cut ribbons and likely introduce dangling bonds.

Turning to the electronic structure of Sb_2Se_3, DFT calculations predict an indirect bandgap of ~1.3 eV, but the direct gap is only a few tens of meV higher resulting in strong optical absorption suitable for thin-film PV applications.[165] The carrier mobility is also highly anisotropic, with the [001] ribbon axis being the preferred direction for charge transport.[166] However, more recent calculations have highlighted that the charge carrier transport is not expected to be 1D due to non-negligible intra-ribbon interactions.[167] The valence and conduction band edges in Sb_2Se_3 have antibonding $Sb\,5s-Se\,4p$ contributions, a feature that has been connected to defect tolerance in other materials containing lone pair cations such as Pb^{2+} or Bi^{3+}.[168] However, explicit DFT calculations for the properties of intrinsic defects in Sb_2Se_3 have shown it to be far from defect tolerant with a number of problematic antisite defects introducing deep levels in the gap.[169]

Recently, Williams *et al.* employed aberration corrected STEM and DFT calculations to provide direct information on the structure and electronic properties of grain boundary defects in Sb_2Se_3.[34] By combining TEM imaging and electron diffraction, the orientation of individual grains relative to the substrate was determined for polycrystalline Sb_2Se_3 films grown on two different substrates (TiO_2 and CdS) using close space sublimation. Both films exhibited a mixed {211}/{221} texture. Aberration corrected STEM was then applied to resolve the atomic structure of an asymmetric grain boundary. The grain boundary plane was found to be approximately parallel to the (041) and (273) planes in each grain (with steps also present) such that the 1D ribbons terminate at the grain boundary from both sides (Fig. 11). To provide further insight into the structure and electronic properties of such grain boundaries, complementary DFT calculations were also performed. Unfortunately, the low symmetry of the particular grain boundary observed experimentally prohibited a one-to-one calculation. Instead DFT calculations were performed for (001) and (041) (273) free surfaces to represent the grain boundary steps and average grain boundary plane, respectively. A calculation for a higher symmetry (041) symmetric tilt boundary was also carried out. These models showed that although dangling bonds are introduced by truncating the 1D ribbons, structural relaxation involving rebonding of under-coordinated atoms (termed "self-healing") readily eliminates all associated defect states within the bandgap. After reconstruction, the valence band maximum and conduction band minimum are also unperturbed compared to the bulk meaning that there is no intrinsic energetic barrier to electron or hole transport. A subsequent study provides further analysis of the effect for a wider range of surface defects in both Sb_2Se_3 and Sb_2S_3.[170] These intriguing results show that it is not only grain boundaries formed parallel to [001] that are benign in Sb_2Se_3. Similar effects have been observed previously for the (110) surfaces of III–V semiconductors[171] and also CdS nanoparticles[172] but what is unusual here is that the reconstructions seem to be effective for all surface and grain boundary terminations considered.

Further insight into the electronic properties of grain boundary defects in Sb_2Se_3 has been obtained via deep level transient spectroscopy (DLTS).[173] Hobson *et al.* showed that very similar defect levels are observed in both bulk crystals and polycrystalline thin films supporting the concept of benign grain boundaries. Kelvin probe force microscopy has also been employed to examine surface potential variation across grain boundaries in Sb_2Se_3 films (Fig. 12). Vashishtha *et al.* found the variation to be $< 50\,mV$, which is small in comparison with other chalcogenide semiconductors such as $Cu(In,Ga)Se_2$ and CdTe, where grain boundaries are known to be deleterious.[174] In fact, such small surface potential variations are more commonly found in halide perovskites, where grain boundaries are also believed to be benign allowing for high efficiencies in polycrystalline films. Both of the above-mentioned studies provide information on the nature of point defects at grain boundaries. While the properties of bulk point defects in Sb_2Se_3 have been studied by DFT,[169] further work is needed to understand the interaction of point defects with grain boundaries, which will provide deeper atomistic insight into the above-mentioned observations as well as aid the interpretation of future electron microscopy and spectroscopy studies of polycrystalline Sb_2Se_3.

B. Metal halide perovskites

Grain boundaries in metal halide perovskites have been studied extensively and have been shown to influence the performance and stability of perovskite solar cell devices significantly, but there is still no real consensus about whether they are beneficial, neutral, or detrimental to the overall performance of perovskite solar cell devices.[175,176] As such, a much more thorough understanding of grain boundaries is
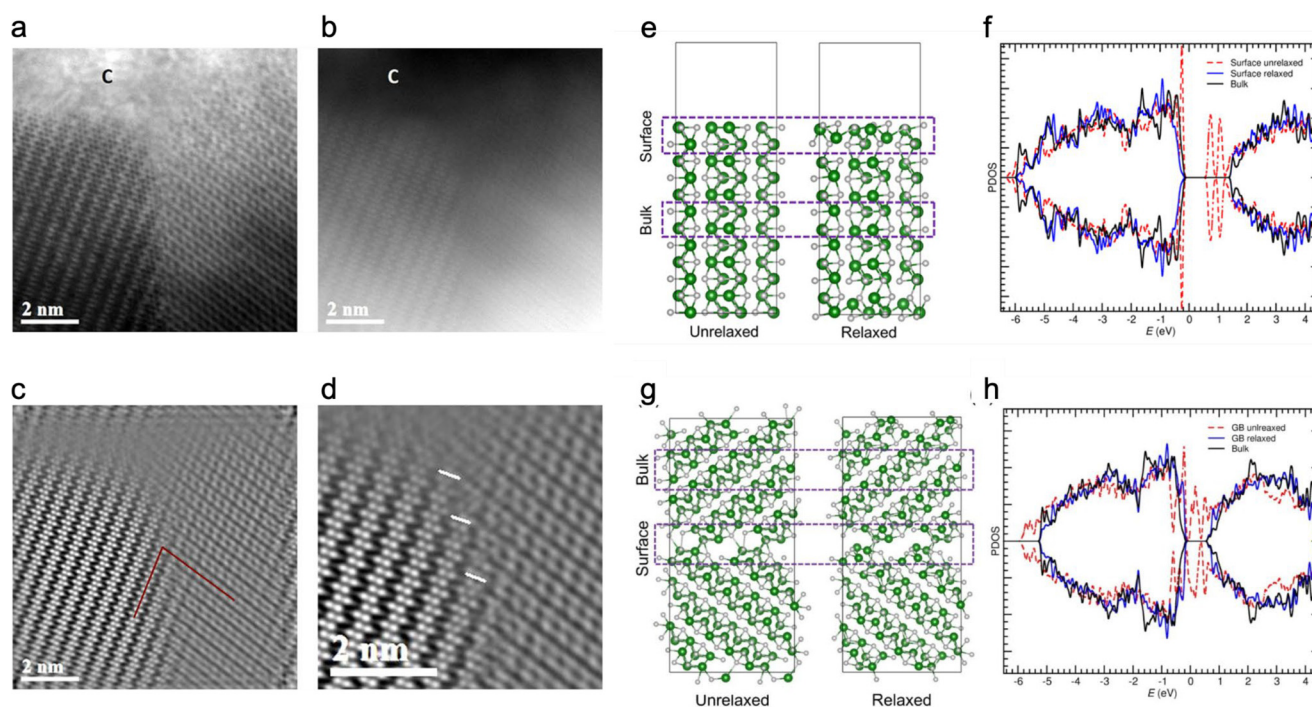
31 January 2024 08:53:32

FIG. 11. AC-STEM images of a Sb_2Se_3 grain boundary in the close space sublimated Sb_2Se_3–CdS device. The simultaneously acquired bright-field and HAADF images are shown in (a) and (b), respectively. The carbon protective layer, used for TEM sample preparation, is annotated with the letter "C." The Fourier filtered image of (b) is shown in (c) with the red lines representing the projected direction of the $(Sb_4Se_6)_n$ ribbons on either side of the grain boundary. (d) An enlarged image of the grain boundary region in (c), where the presence of (001) steps is indicated by the white line segments. (e) Structure of the (001) Sb_2Se_3 free surface (shown in [100] projection) before and after geometry optimization at the HSE + D3 level. The box regions enclose the atoms used for extracting the bulk and surface DOS, respectively. (f) The superimposed spin-polarized DOS plots for the (001) free surface (before and after relaxation) and the bulk. (g) The structure of a (041) Sb_2Se_3 symmetric tilt boundary before and after geometry optimization at the HSE+D3 level. The box regions enclose the atoms used for extracting the bulk and tilt boundary "surface" DOS, respectively. (h) Superimposed spin polarized DOS plots for the (041) tilt boundary (before and after relaxation) and the bulk. Adapted with permission from Williams *et al.*, ACS Appl. Mater. Interfaces **12**(19), 21730–21738 (2020). Copyright 2020 American Chemical Society.[34]

needed, ideally based on an understanding of the atomically derived properties. Rothmann *et al.* were the first to image native hybrid perovskite thin films with atomic resolution using scanning TEM, and they observed a wide range of geometries and grain boundary angles present in all the films, as can be seen in Figs. 13(a) and 13(b).[31] This showed that hybrid perovskite films contain no "standard" grain boundaries, but a wide range, and that there is likely to be a corresponding range of grain boundary properties.

A good way to approach this issue is to use atomic-resolution microscopy to observe real-world grain boundaries and use simulations to understand their various properties. While the wide range of boundaries makes this a large endeavor, work has been done to correlate specific observed boundaries with its corresponding electronic properties. Cai *et al.* did just this, when they combined atomic-resolution STEM imaging of a twin boundary with *ab initio* calculations of its electronic structure.[32]

They used focused ion beam (FIB) milling to create electron transparent lamellae of $FA_{1-x}Cs_xPbI_3$ thin films with x varying from 0 to 1, identifying $x = 0.5$ as the optimal composition in terms of power conversion efficiency. FIB preparation of hybrid halide perovskite TEM sample often causes a large amount of beam damage, but the authors manage to obtain films that still had parts of the pristine

perovskite structure contained within. They then capped the films with a thin layer of amorphous carbon, which improved the stability of the sample under the electron beam.[32] These samples allowed them to observe a range of extended defects within the films, including stacking faults and twin boundaries, a special case of highly symmetric grain boundaries shown in Fig. 13(c). From their micrographs, they were able to construct an atomic model of the twin boundary using the pymatgen package, as seen in Fig. 13(d), which they were able to use for density functional theory (DFT) calculations. To obtain the twin boundary, they performed a mirror operation along the (011) plane, connecting the Pb-I octahedra through common shared faces.[32] They observed negligible gap states at the twin boundary, with the valence band maximum (VBM) mainly being attributed to the antibonding I p states and partially from the Pb s states near the interface. The conduction band maximum (CBM), on the other hand, is dominated by the Pb p states inside the grains, as illustrated by the yellow areas in Fig. 13(e).[32] Since the two domains are effectively mirror images of each other, the partial density of states are almost identical, as shown in Fig. 13(f), and the authors concluded that the twin boundary has little detrimental effect on the performance of the perovskite solar cell devices from an electronic structure perspective. They did, however,
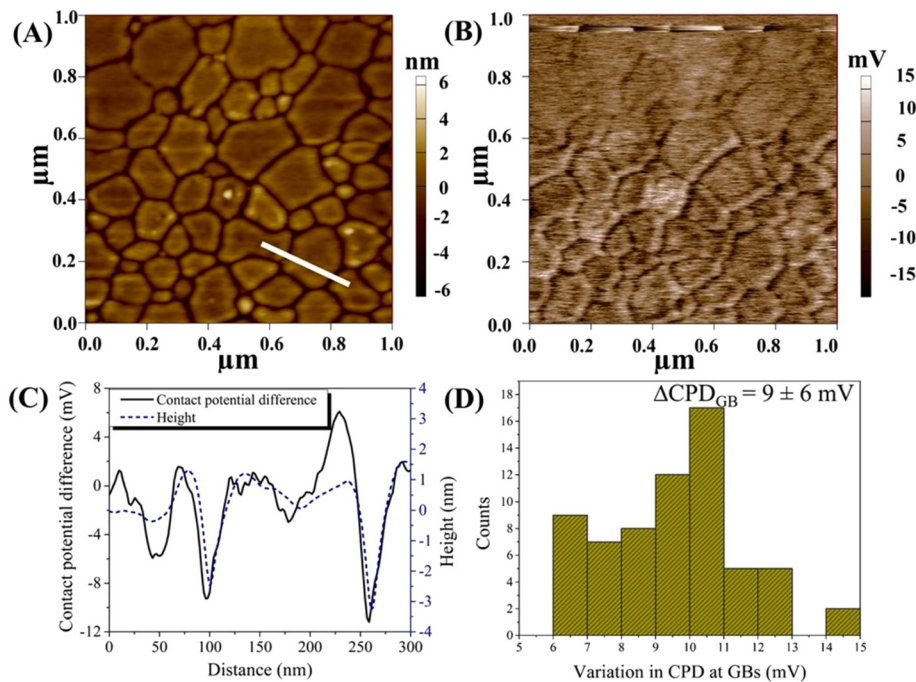
FIG. 12. (a) Topographic atomic force microscopy image of the back side of antimony triselenide film deposited on hydrophobic Si. (b) Kelvin probe force microscopy image of the same region. White line is used to show the contact potential difference (CPD) variation at the grain boundaries and at the edges (c) Line scan of topography and CPD of region marked by white line in (a). (b) Histograms of the CPD variation at the grain boundaries, the ΔCPD is the average CPD variation at the grain boundaries with the standard deviation of n = 65 grain boundaries. Reproduced with permission from Vashishtha *et al.*, J. Alloys Compd. **948**, 169714 (2023). Copyright 2023 Elsevier.[174]

find that the bandgap could be reduced at this interface due to the breaking of inversion symmetry.[32]

Since ions are mobile within the perovskite structure, especially under external stimuli like solar cell operating conditions, the authors also simulated what would happen if an iodine vacancy were to form at the twin boundary. They found a sharp peak in the DOS plot near the valence band edges, but attributed this to p states of the iodine atoms within the grains, which they considered to be benign [Fig. 13(g)]. Introducing Pb interstitials at the twin boundary interface, however, led to localized trap states, mostly due to the p orbitals of the Pb and I atoms close to the boundary [Fig. 13(h)]. The authors concluded that these trap states would be detrimental to solar cell device performance and should be reduced, either by introducing low-dimensional perovskites or by passivating surface defects.[32]

In another first principles study, the structure and properties of the (111) twin grain boundary in $FAPbI_3$ were investigated where it was predicted to be highly stable yet relatively benign in terms of its impact on electronic properties in the absence of any point defects, with only small barriers (<100 meV) to transport of electrons and holes.[35] Nonadiabatic molecular dynamics simulations have also shown such stoichiometric twin boundary defects do not enhance non-radiative recombination.[177] However, in mixed phases with Cs, I, and Br present (111) twin boundaries were predicted as preferential locations for the formation of deleterious secondary phases with reduced bandgap. Subsequent electron microscopy studies have confirmed the presence of (111) twin defects as well as their impact on device performance.[178–180]

C. Cu(In,Ga)Se₂

Atomistic modeling of grain boundaries in polycrystalline Cu(In, Ga)Se₂ has been performed so far using highly symmetric twin boundaries with Σ values of 3. The two different types of Σ3 twin boundaries in *ab initio* simulations are those with (112) and (114) twin boundary planes. The ones with (112) interface can exhibit cation–cation, anion–anion, and cation–anion terminations, which imply different reconstructions.[181] The Σ3-(114) twin boundary contains a dislocation core. An overview of these atomic structures can be found in Ref. 182.

Yan *et al.*[36–38] studied Σ3-(114) twin boundaries in Cu(In,Ga)Se₂ by means of electron microscopy and *ab initio* calculations. These authors concluded that the formation enthalpy of Cu vacancies is by about 0.2 eV lower at the grain boundary than in the grain interior. Moreover, Yan *et al.* found that Na exhibits a negative energy of segregation from the grain interiors to the grain boundary (this result can be understood since Na in NaInSe₂ is octahedrally bonded, while Cu in CuInSe₂ is tetrahedrally bonded; consequently, the solubility of Na in CuInSe₂ is low even in the case of substantial densities of Cu vacancies in the lattice and considering that Na and Cu have very similar ionic radii; it is energetically more favorable for the Na ions to reside at grain boundaries). Yan *et al.* also reported that the deep gap states at Σ3-(114) twin boundaries present due to the dislocation cores can be reduced by inserting Cu_{In} and O_{Se} point defects to the twin boundary. Recently, Raghuwanshi *et al.*[183] showed that Σ3-(112) twin boundaries with cation–anion termination behave electrically as the Cu(In,Ga)Se₂ bulk, whereas those with cation–cation termination exhibited electrical activities, which are reduced by the formation of Cu vacancies. The effect of Cs post-deposition treatments of Cu(In,Ga)Se₂ absorbers on the properties of grain boundaries were analyzed by Schöppe *et al.* using various microscopy techniques in combination with *ab initio* calculations.[182] These authors found that Cs segregates in significant concentrations at grain boundaries and they predicted based on their calculation results that Cs passivates these grain boundaries.
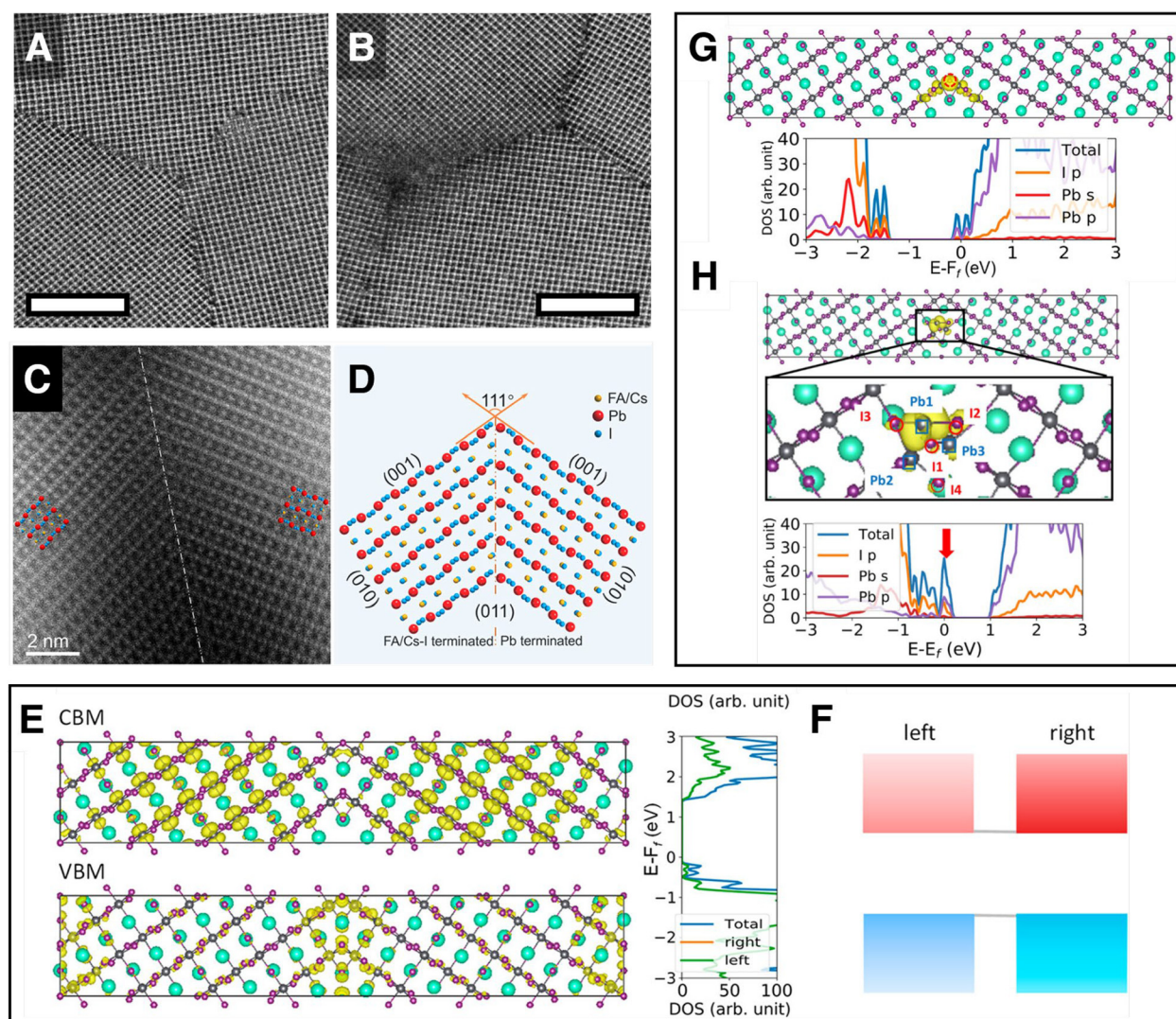
FIG. 13. Atomic-scale STEM characterization and DFT simulation of hybrid perovskite thin films. (a) and (b) Atomic-resolution micrographs of FAPbI$_3$ showing a wide range of grain boundary angles. Used with permission from.[31] (c) and (d) Atomic-resolution micrograph of a twin boundary found in FA$_{0.5}$Cs$_{0.5}$PbI$_3$ and corresponding atomic model used for DFT calculations, respectively. (e) Charge density maps corresponding to the CBM and VBM and the total and partial density of states across the twin boundary. (f) Band alignment diagrams across the interface, upper red rectangle represents the CBM, and the lower blue rectangle represents the VBM. (g) and (h) Charge density map of the shoulder peak near the band edges, total DOS, and partial DOS for Pb s and p orbitals and I p orbitals across the twin boundary with one I and one Pb vacancy added per supercell, respectively. Reproduced with permission from Cai *et al.*, J. Am. Chem. Soc. **144**(4), 1910–1920 (2022). Copyright 2022 Authors, licensed under a Creative Commons Attribution (CC BY) License.[32]

Grain boundary passivation by Rb ions were reported by Chugh *et al.*,[184] also based on *ab initio* calculations.

The results from TEM imaging and electron holography acquired on a Σ9 grain boundary in a CuGaSe$_2$ bicrystal were correlated with multislice simulations as well as with *ab initio* modeling.[185] A mean-inner potential well of 0.8 V in depth and 1.3 nm in width was determined at the Σ9 grain boundary [Figs. 14(a) and 14(b)]. In earlier works, potential wells with depths of 0.2 and 1.1–1.5 V at Σ3 grain boundaries and at randomly oriented grain boundaries were detected.[186,187] These results suggest an increased potential-well depth

with lower symmetry of the grain boundary. In contrast to the depths of the potential wells, their widths are always about the same (1–2 nm), which is in good agreement with the assumption that the atomic planes adjacent to the grain boundary planes in Cu(In,Ga)Se$_2$ are reconstructed (see also Sec. V B). Thus, the presence of the potential wells at grain boundaries in polycrystalline Cu(In,Ga)Se$_2$ thin films, including also the Σ9 grain boundary in the CuGaSe$_2$ bicrystal, can be explained by decreased densities of atoms at the neighboring atomic planes as a result of the reconstruction, which was confirmed for the Σ9 grain boundary by means of *ab initio* modeling [Figs. 14(c) and 14(d)].
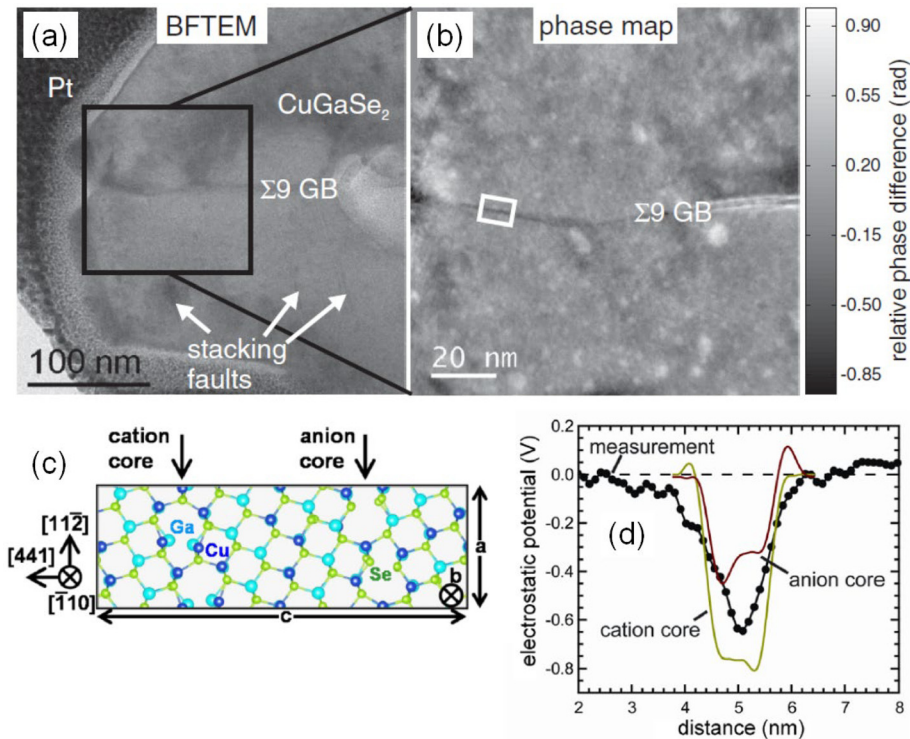
FIG. 14. (a) Bright-field TEM image of a $\Sigma 9$ grain boundary in a CuGaSe$_2$ bicrystal and (b) corresponding gray-value map of the phase of the object wave function. (c) Crystal model of the CuGaSe$_2$ $\Sigma 9$ grain boundary cores after *ab initio* DFT calculations. (d) Multislice-simulated, electrostatic potential profiles across the anion and cation grain boundary cores after a tilt of 1.5 deg, as well as the measured potential profile extracted across the grain boundary in (b). Adapted with permission from Schmidt *et al.*, Phys. Rev. Lett. **109**, 095506 (2012). Copyright 2012 American Physical Society.[185]

D. Titanium dioxide

Titanium dioxide (TiO$_2$) is a nontoxic and earth-abundant semiconductor that finds a number of photocatalytic and renewable energy applications, for example, as a photocatalyst suitable for hydrogen production[188] and wastewater remediation;[189] or as an electron transport medium in dye-sensitized[190] and perovskite solar cells.[191] Typically, TiO$_2$ for use in devices is produced as nanoparticles which are then sintered to produce a colloidal film. Such films necessarily contain large numbers of grain boundaries where particles come into contact with one another, meaning that understanding grain boundaries is essential for improving device efficiency.

There are numerous polymorphs of TiO$_2$, with rutile and anatase the most common. There are various studies of extended defects in rutile including edge dislocations[192] as well as twin[193] and lower-symmetry grain boundaries.[142] A recent investigation of a $\Sigma 13$ grain boundary in rutile TiO$_2$ is particularly of note as a first principles global optimization procedure (*ab initio* random structure searching) was required to successfully identify the grain boundary structure (Fig. 15). It was demonstrated that the boundary had local bonding similar to that of the other common TiO$_2$ phase anatase as well as exhibiting electronic structure that is much more reminiscent of anatase than it is of rutile. Compared to rutile, anatase has garnered significantly more interest due to its higher charge carrier mobility and superior photocatalytic activity.[194] However, anatase poses an experimental problem in that it is unstable except as nano-sized particles; beyond sizes of around 13 nm the particles begin to undergo an irreversible phase transition into rutile.[195] This behavior means that large films cannot be reliably grown, and, for a long time, the only boundary in anatase that had been studied in detail was the $\Sigma 3\{112\}$ twin boundary (TB) that forms frequently by oriented attachment of nanoparticles during hydrothermal coarsening.[196,197] These boundaries are technologically relevant, partly because they act as nucleation sites for the anatase-rutile phase transition; such behavior is unsurprising as much like the anatase-like boundary in rutile, the anatase $\{112\}$ twin boundary exhibits local bonding which is very similar to rutile. Also, because they are extremely prolific in the sort of nanocrystalline anatase samples that would be employed in devices, the properties of such boundaries should be a priority for study.

A first-principles computational study produced a model and complementary simulated TEM image [Fig. 16(a)] showing excellent agreement with experimental observations.[39] The $\Sigma 3\{112\}$ twin is revealed to be a very high-symmetry boundary, with very little deviation from the bulk in terms of bonding aside from some local resemblance to the coordination of rutile. These small deviations also come with small perturbations to the electronic structure, with a very slightly higher density of states near the top of the valence band in the vicinity of the boundary, but no significant change to the bandgap [Fig. 16(b)], in spite of its superficial similarity to rutile. Even though there are no deep trap states in the equilibrium geometry of the boundary, it is predicted that formation of hole polarons is much more favorable at the boundary than in the bulk by around 0.2 eV, which would impact the ability of photogenerated holes to be able to travel to the surface to engage in catalytic processes, but would be benign for *n*-type electron transport applications.

Despite the importance and prevalence of the $\Sigma 3\{112\}$ TB, predictions made based on very high-symmetry defects are not applicable to more general low-symmetry defects that should also be expected to occur. The standard approach of fabricating arbitrary bicrystals is not
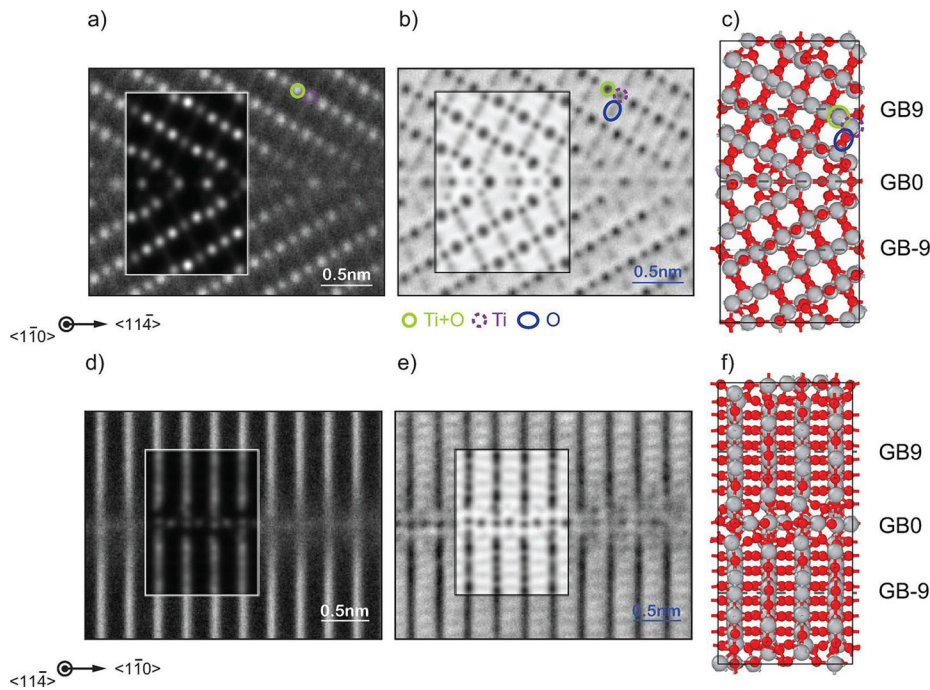
31 January 2024 08:53:32

FIG. 15. (a) Atomic-resolution HAADF. (b) ABF STEM images and (c) the theoretical atomic structure (A∗) of the Σ13 grain boundary along the [1$\bar{1}$0] direction. (d) Atom-resolved HAADF. (e) ABF STEM images and (f) the theoretical atomic structure (A∗) of the Σ13 grain boundary along the [11$\bar{4}$] direction. Image simulations based on the atomic structure of structure A∗ are shown as insets in the experimental HAADF and ABF STEM images. Gray and red spheres represent Ti and O atoms, respectively. Columns of Ti + O, Ti, and O atoms are marked by solid green circles, dashed purple circles, and blue ellipsoids, respectively. Reproduced with permission from Schusteritsch *et al.*, Nano Lett. **21**(7), 2745–2751 (2021). Copyright 2021 Authors, licensed under a Creative Commons Attribution (CC BY) License.[142]

possible due to the instability of anatase, but it is possible to generate anatase bicrystals by exploiting the fact that anatase can be grown epitaxially on strontium titanate. By fabricating a strontium titanate bicrystal, and then using this as a substrate it is possible to encourage the growth of anatase bicrystals in the same orientation as the bicrystalline substrate, an approach employed in a combined experimental and computational study of Σ5 grain boundaries.[150]

The substrate consisted of a Σ5{310} strontium titanate bicrystal which is reflected in the Σ5{310} boundary in the anatase film. However, the anatase film also exhibits two variants (one symmetric and one asymmetric) of a Σ5{103} grain boundary, which can be rationalized by twinning along the Σ3{112} occurring in the grains, causing different crystal planes to appear at the grain boundary (Fig. 17). The asymmetric Σ5{103} grain boundary is produced from the
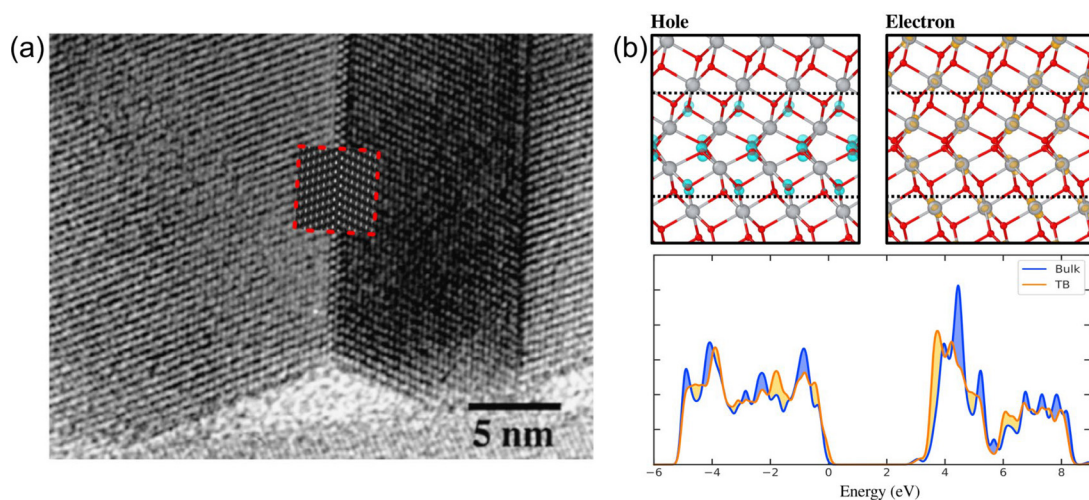
FIG. 16. (a) HRTEM image of a twinned anatase nanoparticle, viewed down {131}.[196] The inlaid image (red dashed border) is a simulated HRTEM image, demonstrating close agreement with experiment. (b) Charge density isosurfaces for vertically added electrons and holes (top), where the area bounded by dashed lines indicates the "TB region." Also shown is the PDOS for a charge-neutral system, projected across the bulk-like region (blue) and the TB region (orange) of the {112}. Shaded areas on the PDOS indicate where a region has a greater number of states of a given energy. Titanium and oxygen ions are represented by gray spheres and red spheres, respectively. Reproduced with permission from Quirk *et al.*, Adv. Theory Simul. **2**(12), 1900157 (2019). Copyright 2019 Authors, licensed under a Creative Commons Attribution (CC BY) License.[39]

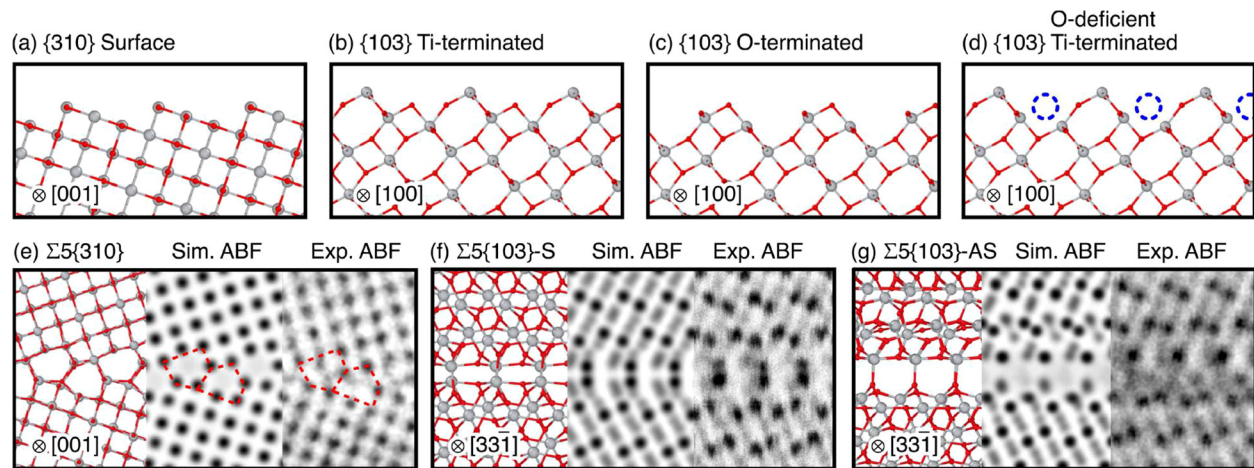**FIG. 17.** Structural models for the surface termination of grains: (a) {310} (b) Ti-terminated {103} (c) O-terminated {103}, and (d) O-deficient Ti-terminated {103}. In all structural models, large gray spheres are titanium and small red spheres are oxygen. The projections for each view are given in the bottom left of each panel. Also shown are corresponding simulated and experimental ABF STEM images for the (e) Σ5{310}, (f) Σ5{103}-S, and (g) Σ5{103}-AS grain boundaries. Reproduced with permission from Quirk *et al.*, Nano Lett. **21**(21), 9217–9223 (2021). Copyright 2021 Authors, licensed under a Creative Commons Attribution (CC BY) License.[150]

combination of an O-terminated {103} grain and an O-deficient Ti-terminated grain, leading to the grain boundary being reduced. O-deficient {103} facets—alongside {102} facets—have been observed through TEM in certain anatase nanoparticle morphologies and oriented attachment along these facets is one way such O-deficient grain boundaries could form.[198] Much like the Σ3{112} twin, projected density of states both the Σ5{310} grain boundary

and the symmetric Σ5{103} grain boundary show very little changes with regard to electronic structure, but the O-deficient asymmetric structure presents electron trap states that appear ∼0.5 eV below the CBM (Fig. 18). The reduced nature of the grain boundary was then confirmed using EELS, which showed an increased presence of Ti^{3+} species in the vicinity of the boundary which was not observed in the other grain boundaries.
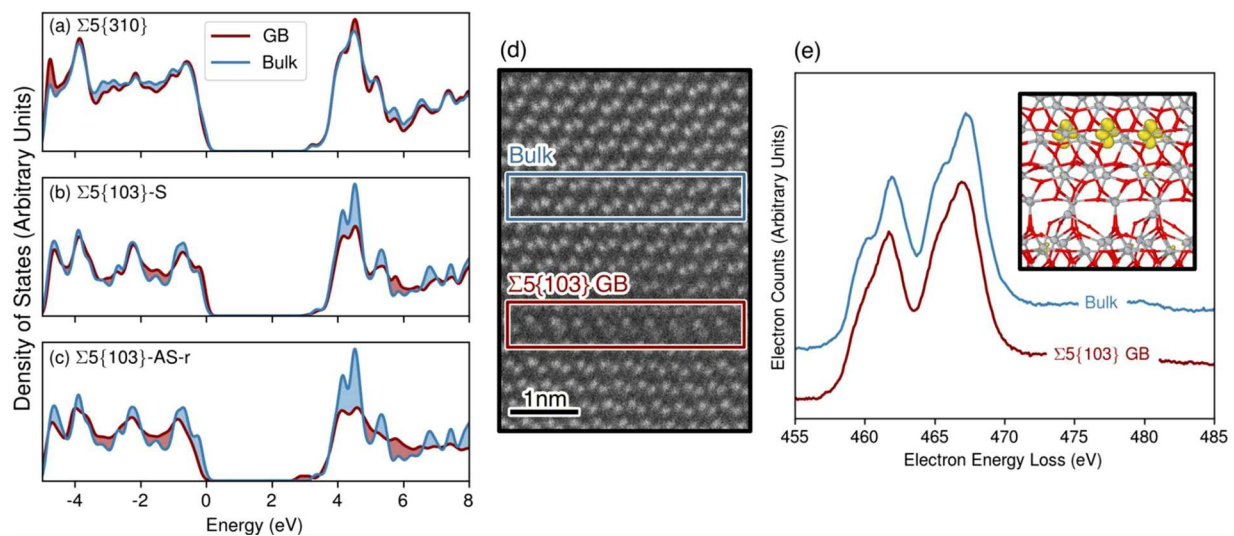

FIG. 18. Projected density of states for the (a) Σ5{310}, (b) Σ5{103}-S, and (c) Σ5{103}-AS-r grain boundaries. For each plot, energy is relative to the valence band maximum, the blue curve represents the bulklike region, and the red curve represents the grain boundary region. The shaded portions indicate where a region has more states of a given energy. For the Σ5{310} and symmetric Σ5{103} grain boundaries, no states appear in the gap, but for the reduced asymmetric Σ5{103}, grain boundary states appear at ∼0.5 eV below the conduction band minimum. (d) STEM image with boxes showing regions corresponding to electron energy-loss spectroscopy (EELS) spectra. (e) EELS spectrum for the bulklike region and the Σ5{103}-S grain boundary region showing the Ti L$_{2,3}$ edge. Curves have been offset vertically for clarity. Note that, in the grain boundary region, the two doublets are replaced by two broad peaks, indicating increased presence of Ti^{3+}. The image shown in the top right is the absolute spin density isosurface (displayed at 0.05 a$_0^{-3}$) associated with electrons trapped in the vicinity of the Σ5{103}-S grain boundary. Reproduced with permission from Quirk *et al.*, Nano Lett. **21**(21), 9217–9223 (2021). Copyright 2021 Authors, licensed under a Creative Commons Attribution (CC BY) License.[150]

The general consensus of the results is that near-stoichiometric anatase grain boundaries introduce few trap states, which goes some way to explain the high performance of polycrystalline anatase as a charge transport layer in PV technologies. Highly O-deficient grain boundaries, however, can introduce significant numbers of traps and may preferentially form in O-poor synthesis conditions or through oriented attachment of defective surfaces, indicating a need to suppress these grain boundaries via, for example, directed doping of the nanoparticle surfaces prior to sintering.

E. Lithium lanthanum titanium oxide

Many of the safety problems that plague lithium-ion batteries (LIB) are promised to be solved by exchanging the flammable liquid electrolyte for a solid-state electrolyte (SSE). Huge efforts have been made to design materials, which exhibit Li-ion conductivity that is competitive with conventional liquid electrolytes while also remaining chemically and mechanically stable during operation, but detailed microscopy studies of SSE materials are faced with two major challenges. First, lithium is an extremely light element making it difficult to observe in STEM except by annular bright field (ABF), a problem also encountered when trying to image the O ions in oxides.[199] Second, LIB materials are often extremely sensitive to beam damage, limiting atomic-resolution (S)TEM studies to materials that are reasonably stable under beam irradiation.[200] Computational insight is invaluable in situations where experiments tend to struggle, experimental results from beam-tolerant materials are vital in order to highlight properties that must be considered when designing computational studies. Here, we shall outline what has been learned from such experiments and how this information can guide the design of computational studies.

Lithium lanthanum titanium oxide (LLTO) is a beam-tolerant double perovskite material with the formula $Li_{3x}La_{(2/3-x)}TiO_3$, where $0 < x < 0.16$, consisting of alternating layers of La-rich and La-poor layers. In the La-poor layer, La ions are replaced with either Li ions or with vacancies, where these vacant sites enable Li diffusion throughout the layer. An atomic force microscopy (AFM) study on polycrystalline LLTO has provided qualitative evidence of loss of Li-ion conductivity at grain boundaries,[201] by exploiting the AFM tip to move Li-ions in a

material and measure the subsequent change in strain, a method referred to as electromechanical strain microscopy (ESM).[202] A subsequent ESM study also provided complementary atomic-resolution STEM images of Σ5 and a Σ13 grain boundaries of LLTO, where it was found that the Σ13 caused far more severe reductions in Li-ion conductivity compared to the Σ5. EELS measurements indicated that a portion of the Ti^{4+} was reduced to Ti^{3+} at the boundary, indicating the presence of oxygen vacancies. The segregation of large numbers of positive defects, such as v_O^{1+} or v_O^{2+}, to the boundary will lead to the development of a positive space charge region, which will inhibit the transport of the like-charged Li^+ ions into and through the grain boundary region. Segregation energies and space charge potentials are straightforwardly extracted from computational models and represent a relatively simple way of gauging possible impacts of grain boundaries in beam-sensitive SSEs where high-quality experimental data are lacking. Space charge regions are not the only way in which defect segregation can affect conductivity as ion diffusion is often vacancy-mediated, meaning that Li diffuses by hopping into vacant sites. If the concentration of v_{Li}^{1-} is different at the grain boundary, this will have large effects on the diffusion as demonstrated by a phase-field modeling study of the antiperovskite-structured SSE Li_3OCl.[203]

Of course, one should not expect space charge regions to be the only source of lowered ionic transport at grain boundaries; large deviations from the bulk in terms of structure will also play a role even in the absence of other point defects. A prevalent extended defect in LLTO is the 90° domain boundary, which was investigated in a combined computational and experimental study which aimed to elucidate its effects on ionic diffusion (Fig. 19).[27] Ionic conductivity is related to the diffusion coefficient, D, which is defined as

$$D = D_0 \exp\left(\frac{E_a}{kT}\right), \tag{18}$$

where E_a is the activation energy of the pathway that the ion is moving through. Since LLTO has a perovskite structure and the domain boundary is relatively high-symmetry, the character of this pathway can be reasonably assumed, allowing for the use of nudged elastic band (NEB) theory. In NEB, the migration path is divided in several
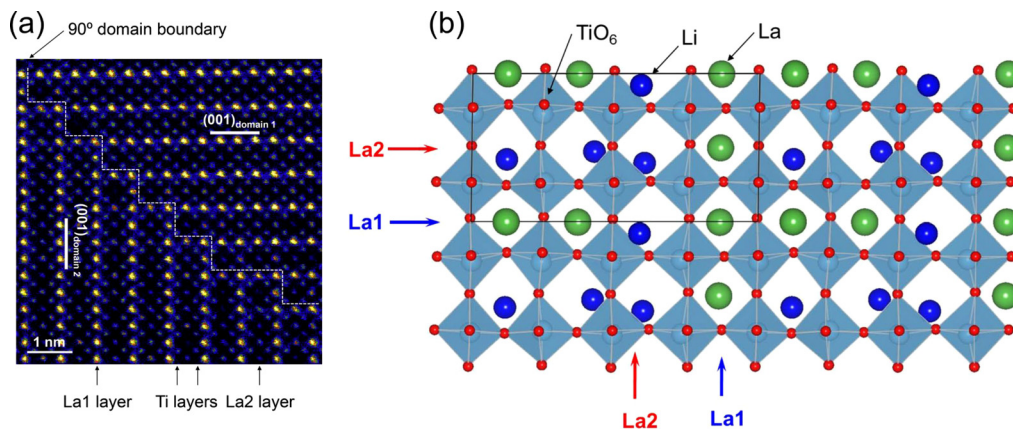
FIG. 19. (a) Structure of a 90° domain boundary within an $La_{0.62}Li_{0.16}TiO_3$ grain obtained by aberration-corrected HAADF-STEM. (b) Computational model of this domain boundary used for Li-ion migration calculations. The boundary model represents the boundaries marked by dotted lines in (a), replicating the arrangement of the La-rich and La-poor layers. Reproduced with permission from Moriwake *et al.*, J. Power Sources **276**, 203–207 (2015). Copyright 2015 Elsevier.

equidistant images that interpolate between the initial and final geometry, which are then subjected to a geometry optimization constrained with spring forces to prevent the images falling into minima. It is found that the activation energy for diffusion through the domain boundary is 0.58 eV, which is in reasonable agreement with experimental values of around 0.45 eV, but much higher than the theoretical value in bulk of 0.19 eV, highlighting that the performance of LLTO is severely limited by domain boundaries. The NEB method is computationally cheap, making it an extremely valuable tool for determining barriers to ionic migration which has seen use in a computational study which demonstrates that stoichiometric Li_3OCl grain boundaries impede ion conductivity,[204] as well as in studies of materials that, while not all strictly SSEs, strongly rely on ionic mobility for their operation such as solid-oxide fuel cell materials[205] and oxide cathode materials.[206,207] It must of course be noted that NEB can only be employed in cases where the pathway is either well-known or can be reasonably assumed. For lower-symmetry interfaces or more complex materials, molecular dynamics (MD) can be employed to calculate D as

$$D = \frac{MSD(t)}{6t}, \quad (19)$$

where MSD(t) is the mean-squared displacement at time t. Typically, D will be determined from the gradient of a straight line fitted to MSD (t) vs t. Then, by calculating D at a range of temperatures, the activation energy can be calculated from the Arrhenius relation. Such an approach is employed extensively and also shows that severe reduction in Li^+ conductivity also occurs in lower symmetry boundaries in LLTO,[208] as well as in other oxide materials such as Li_3OCl.[209]

While LLTO is an excellent material for case studies, its value in real-world applications is limited by the issues posed by extended defects, which reduce its excellent bulk conductivity of around 10^{-3} Scm^{-1} to a poor total conductivity on the order of 10^{-5} Scm^{-1}.[210] Fortunately, the related garnet-type material lithium lanthanum zirconium oxide (LLZO) with formula $Li_7La_3Zr_2O_{12}$ exhibits a higher total conductivity on the order of 10^{-4} Scm^{-1} (Ref. 211) while also being sufficiently beam-tolerant for TEM studies. The structure of LLZO poses some problems for computational studies as it has a very large primitive cell containing 96 atoms for the tetragonal phase and an even larger 192 atoms for the disordered (and highly conductive) cubic phase. Building grain boundary models from such cells while still retaining a proper bulk-like region can quickly lead to systems containing many thousands of atoms.

Even if it is not possible to build computational models which exactly correspond to experiment, it should still be possible to build sensible and representative models based on observations. For example, a HRTEM study on hot-pressed LLZO pellets indicated that, despite the complexity of the primitive cell, the majority of the grains were directly connected through grain boundaries, free of secondary or amorphous phases,[212] which provides justification for the use of standard bicrystal models of tilt grain boundaries. Such bicrystal models were employed in a classical MD study which demonstrated that room temperature Li-ion diffusion normal to the boundary plane is severely reduced while, in some cases, diffusion is increased parallel to the boundary plane. These results are attributed to the decreased density at the boundary, providing a clear strategy of higher processing sintering temperatures to increase the crystallinity at the boundary.[213]

The use of classical potentials allows diffusion coefficients to be determined for large supercells at realistic temperatures, but it does not allow access to electronic structure. While not relevant to ionic conductivity, electronic structure plays a crucial role in a major degradation mechanism of SSEs, where undesirable electronic conductivity allows Li^+ ions to combine with electrons, being reduced to Li and nucleating the formation of Li metal dendrites within the material, which can eventually lead to short-circuiting of the device.[214] Experimental observations indicate that dendrites preferentially nucleate at grain boundaries and that some grain boundaries have severely narrowed band gaps.[212] A first-principles study of the thermodynamics of intrinsic defects in LLZO predicted that it should show low electrical conductivity,[215] further reinforcing that observed electrical conductivity in LLZO occurs at extended defects. Due to computational cost, first-principles studies of LLZO are restricted to high-symmetry $\Sigma 1$ and $\Sigma 3$ grain boundaries, but calculations have shown that under-coordinated Zr at the boundary correspond to gap states which may partly explain the reduction in band gaps.[33]

Evidence from these LLTO and LLZO studies highlights the importance of grain boundaries in the operation and failure of SSEs. For beam-sensitive materials, computational work is making progress in enriching the understanding of the properties of grain boundaries. For example, *ab initio* methods have been successfully applied to the $Li_2OHCl_{1-x}Br_x$ family of solid electrolytes, where the computational prediction of higher grain boundary resistance was then realized experimentally by showing that synthesis that results in larger grains leads to higher Li-ion conductivity.[216] Other studies go beyond simple bicrystal models of symmetric tilt boundaries into truly polycrystalline models of randomly arranged grains containing a wide variety of asymmetric tilt and twist boundaries. Such an approach was taken for the sulfide Na_3PS_4 and the isostructural oxide Na_3PO_4 and demonstrating that, as grain size decreases, the conductivity drops significantly for the oxide but increases slightly for the sulfide, which is attributed to less strong coordination to the more diffuse S^{2-} anions.[217] The field of SSEs is rich and challenging, but a concerted effort between theory and experiment is capable of providing material design principles which can guide the engineering of devices.

V. CASE STUDIES II: IMPACT OF GRAIN BOUNDARIES IN FUNCTIONAL MATERIALS ON DEVICE PERFORMANCE

A. Silicon

The topic of grain boundaries in multicrystalline Si wafers or in polycrystalline Si thin films has been treated by numerous reports in the literature (e.g., Refs. 4 and 218). Correspondingly, the electronic properties of these grain boundaries are influenced strongly by impurities segregating to the grain boundary planes. The segregation process may even lead to the formation of precipitates composed of impurity atoms as well as of impurity oxides or silicides.[219,220] Of these impurities, Fe has been reported as particularly detrimental in p-type Si, due to the large capture cross section of the corresponding defect states for electrons (as compared with that for holes, which is why the use of n-type Si has been considered for optoelectronic devices[221]). On the other hand, defects related to Co, Cr, and Ni impurities were highlighted as considerably recombination active in n-type Si.[222]

Most grain boundaries in polycrystalline Si exhibit low Σ values,[223,224] i.e., they are highly symmetric. Due to this high symmetry,

they do not offer much space for impurity atoms, which is why no or only slightly enhanced nonradiative recombination with respect to the bulk occurs.[225] Two- and three-dimensional device simulations of multicrystalline Si solar cells[226,227] confirm substantial deterioration of the open-circuit voltage by enhanced nonradiative recombination at randomly oriented (i.e., low-symmetry) grain boundaries.

Recombination velocities for random grain boundaries in multicrystalline Si wafers or polycrystalline Si thin films have been reported to be as high as 10^3–10^5 cm/s.[108,109,228,229] By means of gettering as well as by hydrogenation, it is possible to decrease these high values to about 10^2–10^3 cm/s.[230]

We can reproduce in a rough manner recombination velocities measured on grain boundaries in multicrystalline Si wafers by means of photoluminescence imaging[231] by applying Eq. (4). The result is shown in Fig. 20. For the sake of simplicity, the prefactor $s_{gb,0}$ is assumed to be equal for all grain boundaries of an individual Si wafer and set to the median of the experimentally measured values. (Actually, this prefactor can be expected to vary slightly from grain boundary to grain boundary within the same order of magnitude. Thus, a correspondingly large error must be supposed for $s_{gb,0}$.) The resulting values for upward or downward band bending, φ_B, are given in red next to the simulated recombination velocities. The values range from several -10 meV to several $+10$ meV and thus, agree well (in terms of orders of magnitude) with the barrier heights published by S. Tsurekawa *et al.*[232] (measured on Si wafers by means of scanning Kelvin-probe force microscopy) and by Scheller and Nickel[233] (measured in Si thin films as barriers for charge-carrier transport).

It is noteworthy that by photoluminescence imaging, no s_{gb} values smaller than 200 cm/s can be determined.[231] Nevertheless, the situation depicted in Fig. 20 agrees well with recombination at grain boundaries at which the recombination activities via the defect densities N_{gb} are very similar to one another, and the recombination velocities at

various grain boundaries differ only via different, positive or negative net-charge densities, driving free charge carriers to or repelling them from the grain boundary planes. We also note that a significant passivation effect at grain boundaries via gettering or hydrogenation cannot be confirmed.

B. Cadmium telluride

Grain boundaries in CdTe thin films were reviewed by Major.[28] Clear V_{oc} losses (probably via enhanced, nonradiative recombination) via grain boundaries were demonstrated by Burst *et al.*[234,235] when comparing polycrystalline and single-crystalline CdTe by means of experiments and simulation. Exhibiting an adamantine, cubic crystal structure, most grain boundaries in CdTe thin films exhibit low Σ values,[236,237] similar to multicrystalline Si. Various atoms/ions have been reported to segregate to grain boundaries.[28] Among the impurity atoms/ions, Cl was reported to exhibit the highest concentrations at grain boundaries, in case the CdTe layer was treated by $CdCl_2$ post-deposition.[238] Regarding the region of changes in composition around the grain boundary plane, it was found to be very narrow (about 1–2 nm from electron energy-loss spectroscopy in scanning transmission electron microscopy).[238] This result together with the fact that no clustering has been reported suggests that no extended, secondary phase is present at grain boundaries in CdTe. Rather, the atomic planes adjacent to these planar defects are atomically reconstructed, as also the case for grain boundaries in polycrystalline Cu(In,Ga)Se$_2$ thin films (see Sec. V C).

EBIC combined with EBSD analyses at grain boundaries[239] show enhanced EBIC signals at grain boundaries. However, this feature has been identified as possible artifact in EBIC measurements in the case of high-injection conditions,[111] which are likely to be present if small beam energies are used (only 3 kV in Ref. 239, leading to high densities
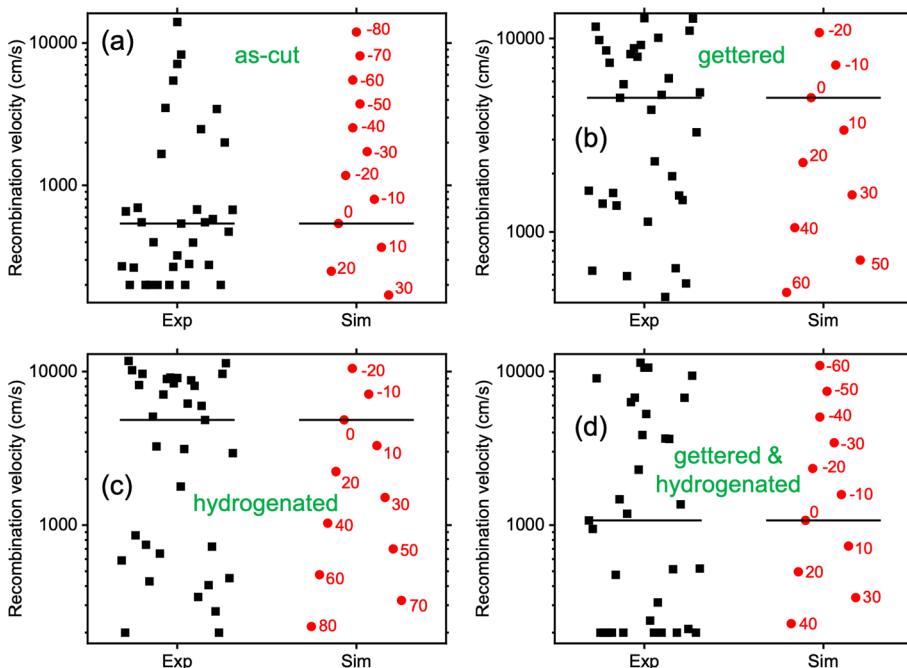

FIG. 20. Experimental (Exp) recombination velocities from Ref. 231 (*p*-type mc-Si) and simulated (Sim) values using Eq. (4). The median value for each sample series is highlighted by a horizontal, solid line and used as $s_{gb,0}$ in Eq. (4). The barrier heights obtained from Eq. (4) are given in red next to the simulated recombination velocities.

31 January 2024 08:53:32

of electron–hole pairs generated by the electron beam in CdTe, exceeding the net-doping density). Moreover, strong band bending with barrier heights of up to several 100 meV has been reported by various authors (see Ref. 28 and references therein). In view of the rather low net-doping densities of 10^{14}–10^{15} cm^{-3} (Ref. 156) and with respect to the discussions in Sec. II C 1, it is probable that (almost) all free charge carriers are trapped in the defect states at the grain boundary plane and thus, no significant band bending is present at the grain boundary planes in CdTe thin films. The reported band bending with values of several 100 meV can be understood by the fact that the applied methods are surface-sensitive; when assuming larger net-doping densities at the surface, still sufficiently small to remain in regime I (Sec. II C 1), they would indeed lead to higher barrier heights as described by Eq. (1).

CL intensities at CdTe grain boundaries have been found to be decreased with respect to the grain interiors,[240,241] which, assuming that no extended, secondary phases are present at or around the grain boundaries, is a clear indication for enhanced nonradiative recombination at these planar defects. The reported recombination velocities s_{gb} are on the order of 10^4–10^5 cm/s (actually, Stechmann et al.[241] only give reduced recombination velocities and effective diffusion lengths; but the s_{gb} values can be estimated via Eq. (8), assuming bulk lifetimes of about 10 ns as given in Ref. 240). The large magnitudes of these s_{gb} values are probably due to high-injection conditions during the CL analyses (Stechmann et al.[241] give 3 nA as applied beam current), which is corroborated by the fact that the recombination velocities for various grain boundaries in the same CdTe thin film vary only slightly within the same order of magnitude. As already outlined in Sec. III A 1, the s_{gb} values under low-injection conditions can be assumed to be about 1–2 orders of magnitude smaller. Moreover, Kanevce et al.[240] found that a CdCl$_2$ post-deposition treatment leads to slightly smaller recombination velocities. This result cannot be interpreted as a strong grain boundary passivation effect of this treatment; rather, the CdCl$_2$ treatment is known to increase the average grain size and the bulk lifetime,[242] which can be expected to lead to the decreased recombination velocities detected in the CL experiment. In contrast to these results, Moseley et al.[243] reported significant decreases of the recombination velocities at grain boundaries for CdCl$_2$-treated as well as for CdCl$_2$- and Cu-treated samples as compared with as-deposited CdTe thin films. Thus, whether or not CdCl$_2$ treatments have indeed a passivating effect on grain boundaries remains ambiguous, probably also since it can be assumed that CdCl$_2$ treatments performed in different laboratories are not the same.

C. Copper indium gallium selenide

Review papers on the impact of grain boundaries in Cu(In,Ga)(S, Se)$_2$ were published by Rau et al.,[244] by Abou-Ras et al.,[245] and by Cojocaru-Mirédin et al.[246] In contrast to grain boundaries in multicrystalline Si, these planar defects in polycrystalline Cu(In,Ga)(S,Se)$_2$ thin films feature atomic reconstructions of the atomic planes adjacent to the grain boundary planes.[181,187] All matrix elements and also impurities such as O, Na, or K participate in this reconstruction, and always different grain boundary compositions are found for different grain boundaries. However, there are two distinguished patterns always detected when analyzing the grain boundary compositions as compared with that of the grain interiors. Either the grain boundary plane is Cu-depleted, then it is enriched in In and also in Se. Or it is

Cu-enriched, then it is In-depleted and Se-depleted; only in the latter case, oxygen is found at the grain boundary (for Se-enriched grain boundaries, i.e., Se^{2-} ions on interstitial sites, all anion sites are occupied, and no space is available for oxygen ions). This highly reproducible pattern[247] can be interpreted by either In$_{Cu}^{2+}$ and Se^{2-} or Cu$_{In}^{2-}$ and V$_{Se}^{2+}$ as dominant point-defect pairs that compensate one another; all other point defects (anti-site defects, vacancies, impurity-related) merely contribute to the defect ensemble of each grain boundary.

Raghuwanshi et al.[248,249] showed a systematic correlation between Cu-poor (Cu-rich) grain boundaries and enhanced (reduced) EBIC signals at grain boundaries. Thus, these authors suggested that Cu-poor grain boundaries are benign, whereas Cu-rich grain boundaries are detrimental to the device performance. Although the correlation between the grain boundary composition and the change in the EBIC signal can be assumed real, enhanced EBIC signals at grain boundaries have already been identified as artifacts for surfaces prepared by a focused-ion beam or in the case of high-injection conditions during the EBIC analysis[111] (i.e., low beam energy and high beam current). It is still not clear whether there is indeed a direct correlation between the composition, the crystal facet at the grain boundary plane, and the collection/recombination properties of the grain boundary.

Since the chalcopyrite-type crystal structure of (Ag,Cu)(In,Ga)(S, Se)$_2$ is adamantine (i.e., similar to the face-centered cubic structure of Si), also in this material, most grain boundaries exhibit low Σ values.[250] The recombination velocities s_{gb} determined at randomly oriented Cu (In,Ga)Se$_2$ grain boundaries by means of cathodoluminescence[44,45] follow a similar pattern as found for grain boundaries in multicrystalline Si. The values of s_{gb} range typically between 10^1 and 10^4 cm/s and can be described, as in the case of Si grain boundaries, by using Eq. (4). Figure 21 provides an example of recombination velocities obtained at Cu(In,Ga)Se$_2$ grain boundaries in a high-efficiency solar cell (21% conversion efficiency without anti-reflection coating). As can be seen in Fig. 21, the s_{gb} values vary between 10^1 and 10^3 cm/s, with a median value $s_{gb,0}$ of about 300 cm/s, and the upward or downward band bendings, φ_B, range from several -10 meV to several $+10$ meV (as in the case of Si). These barrier heights are similar to those determined by
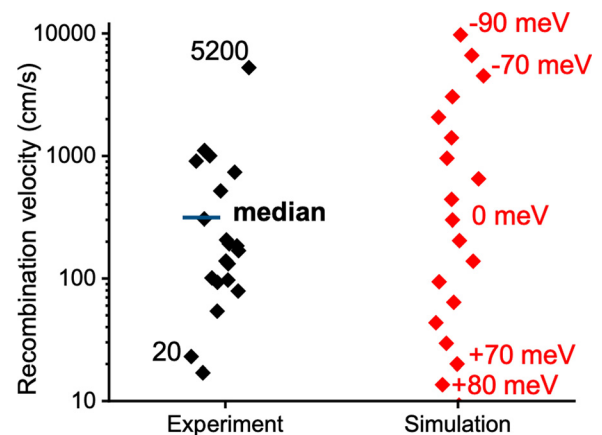

FIG. 21. Experimental recombination velocities from Ref. 51 and simulated values using Eq. (4). The median value of about 300 cm/s is highlighted by a horizontal, solid line and used as $s_{gb,0}$ in Eq. (4). The barrier heights obtained from Eq. (4) are given in red next to the simulated recombination velocities.

31 January 2024 08:53:32

conductive atomic force microscopy,[251] but differ from those measured by means of Kelvin-probe force microscopy (KPFM),[252] for which the φ_B values are often larger by about one order of magnitude. This discrepancy can be explained by the surface sensitivity of the KPFM technique and, using Eq. (4), by a smaller net-doping density N_A or also by a higher density of (charged) defects N_{gb} at the film surface.

The s_{gb} values shown in Fig. 21 are the ones published in the work by Krause et al.[51] These authors used a real microstructure extracted from an electron backscatter diffraction map for a two-dimensional device simulation. It was found that the photovoltaic parameters of the Cu(In,Ga)Se$_2$ solar cell were reproduced successfully by the simulation for $s_{gb,sim} \approx$ 200–500 cm/s and assuming barrier heights φ_B varying between -50 and $+50$ meV, in good agreement with the median value of $s_{gb,0} \approx$ 300 cm/s (Fig. 21). The approach of describing the recombination activities of grain boundaries in CIGSe thin films via Eq. (4) was confirmed successfully by these two-dimensional device simulations. It is noteworthy that the V_{oc} values were found to be strongly affected by the presence of grain boundaries [decreased substantially with increasing s_{gb}, as can be expected from Eqs. (4)–(7)], while the short-circuit current density j_{sc} hardly changed. Thus, the main effect of grain boundaries in Cu(In,Ga)Se$_2$ thin films is enhanced nonradiative recombination, leading to corresponding V_{oc} losses.

Nicoara et al.[252] showed by means of KPFM measurements that post-deposition treatments using KF, RbF, and CsF after the Cu(In,Ga)Se$_2$ deposition can lead to decreased barrier heights φ_B at grain boundaries and interpreted this result as evidence for grain boundary passivation by the alkali-metal post-deposition treatment. However, with respect to the discussion in Sec. II C 3, a decrease in φ_B alone is an insufficient criterion; it may be that simply, the net-doping density at the Cu(In,Ga)Se$_2$ film surface (which was probed using KPFM) becomes larger by the alkali-metal post-deposition treatment, which according to Eq. (2) would result in a decreased barrier height (assuming N_{gb} remains the same). In contrast, Abou-Ras et al.[44] were not able to confirm decreased s_{gb} values for the NaF or KF post-deposition treatments of Cu(In,Ga)Se$_2$ absorber layers.

D. Halide perovskites

Some of the first studies on hybrid halide perovskite grain boundaries were done using Kelvin probe force microscopy (KPFM) and atomic force microscopy (AFM), and showed that grain boundaries helped efficiently separate and collect charges.[253,254] Additionally, grain boundaries in films containing no passivating additives have been shown to have lower contact potential difference (CPD) than the grain interior when no bias voltage is applied. However, applying a positive bias increases the CPD of the grain boundaries to above that of the grain interiors, and applying a negative bias has the opposite effect, indicating that there are either more ions present intrinsically at grain boundaries, or the boundaries allow for easy ion migration,[255] and this effect can be modulated by additives.[256]

Other studies have shown that grain boundaries have a detrimental effect on the performance of perovskite solar cell devices. For example, fluorescence lifetime measurements have shown that the photoluminescence (PL) intensity decreases near grain boundaries, indicating that grain boundaries act as centers for non-radiative recombination, and various passivating additives, like pyridine,
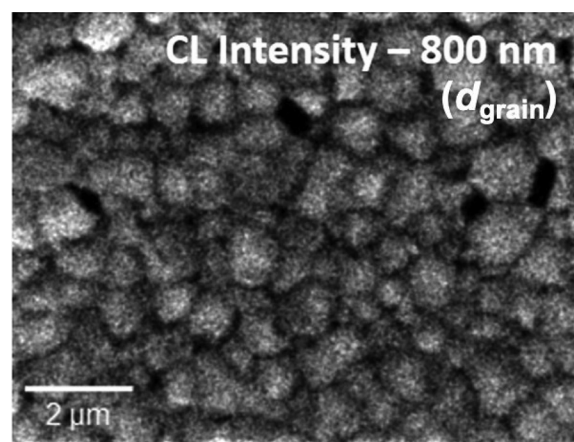

FIG. 22. CL intensity distribution acquired on a Cs$_{0.05}$(FA$_{0.95}$MA$_{0.05}$)$_{0.95}$Pb(I$_{0.95}$Br$_{0.05}$)$_3$ thin film using a bandpass filter at 800 nm (± 50 nm), corresponding to the bandgap energy of the halide-perovskite thin films of about 1.54 eV. Reproduced with permission from Gutierrez-Partida et al., ACS Energy Lett. **6**, 1045–1054 (2021). Copyright 2021 American Chemical Society.[260]

increase the PL intensity of grain boundaries.[29] Grain boundaries in hybrid halide films have also been associated with increased hysteresis, by increasing the low-frequency capacitance of a film,[257] and reduced long-term stability, as grain boundaries can assist hydration of the perovskite grains, eventually leading to irreversible degradation.[258]

Owing to the very low net-doping densities in halide-perovskite thin films [about 10^{12} cm^{-3} (Ref. [259])] high-injection conditions during cathodoluminescence analyses cannot be avoided. Thus, corresponding recombination velocities can be expected to be all on the same order of magnitude (Sec. III A 2). In view of very high bulk lifetimes in halide perovskites of several μs or even several 10 μs, the recombination velocities are very low, only a few cm/s. Nevertheless, also at grain boundaries in halide-perovskite thin films, enhanced nonradiative recombination contributes to a V_{oc} loss in the respective solar-cell devices. Figure 22 shows a cathodoluminescence intensity-distribution map from a Cs$_{0.05}$(FA$_{0.95}$MA$_{0.05}$)$_{0.95}$Pb(I$_{0.95}$Br$_{0.05}$)$_3$ thin film with effective lifetime of about 18 μs.[260] The high-injection conditions let the decrease in CL intensity at the grain boundaries appear much stronger than it actually is (owing to high-injection conditions, the radiative recombination rates are very large, leading to very strong decreases of the CL intensity from the grain interiors to the grain boundaries).

VI. CHALLENGES AND FUTURE DIRECTIONS
A. First principles modeling

It is now commonplace to employ first principles materials modeling to identify materials suitable for particular applications. For example, a prospective solar absorber for photovoltaic applications should be stable and composed of abundant and nontoxic elements, exhibit strong absorption with a bandgap well matched to the solar spectrum on the Earth's surface, and have good charge carrier mobility with low rates of non-radiative recombination. It is relatively straightforward to screen both bulk crystal properties and also those of intrinsic point defects against these requirements. However, screening based on the properties of grain boundary defects is a much more difficult

31 January 2024 08:53:32

challenge. Real polycrystalline materials contain a wide variety of grain boundary defects (both low and high symmetry). The structure and properties of these grain boundaries (including space charge layers) depends on the overall concentrations of intrinsic defects and impurities as well as the material's processing history. Most of the examples of modeling presented in this review consider a small number of relatively high symmetry grain boundaries (often those identified by microscopy) initially without any point defects. Some also consider point defect segregation as a second step but a global structural minimization for non-stoichiometric grain boundaries is far less common and extremely computationally demanding due to the vast configuration space. To properly screen against grain boundary properties, one would need to do this not just for one high symmetry grain boundary model but a representative set of grain boundaries some of which may have very low symmetry and therefore increase the computational cost even further. Such a comprehensive screening of grain boundary properties is beyond the reach of first principles approaches today. Even if it were, there is also the challenge that we have no reliable way to predict which set of grain boundaries could be considered representative.

While we are a long way from a solution to all of the challenges summarized above there are some encouraging recent developments that may allow us to take some steps in the right direction. The most ambitious attempts to model grain boundaries in materials, in terms of the number of grain boundary types and the size of models considered, have been carried out using interatomic potentials due to their lower computational cost. However, as discussed in Sec. III B 1, although they work well for some materials there are challenges with parameterization, accuracy and transferability in general. Machine learning potentials that are trained on first principles calculations have the potential to solve this problem and make grain boundary investigations exploring much larger parameter spaces feasible while retaining the accuracy of first principles approaches. We will soon enter the exascale era of high performance computing (i.e., supercomputers capable of performing 10^{18} double precision operations per second). In parallel with this growth in processing power, first principles modeling codes and approximations are continuing to evolve to take full advantage of the new hardware enabling calculations on much larger systems, longer-timescale dynamics or high-levels of accuracy than has been possible to date.

B. Electron microscopy

Obtaining direct information about the properties of grain boundaries found in energy materials can be challenging, but with appropriate care and appreciation of the abilities and limitations of a range of techniques, it is possible to extract a wealth of information about grain boundaries. Integrating multiple techniques allows for a comprehensive understanding of grain boundaries, as we have seen. While many of the microscopic characterization techniques require careful consideration of the influence of the measurement itself on the properties of the material being studied, we have shown that there is a range of conditions under which it is possible to study technologically important energy materials with high enough resolution to be able to distinguish the properties of the grain boundaries separately from those of the bulk.

Combining this variety of techniques makes it possible to identify critical factors affecting the overall performance of solar cell devices, such as the local crystallography, chemical makeup, and electronic properties of grain boundaries.

It is clear that there is a wide space for improving grain boundary-specific techniques and protocols, as evidenced by the many restrictions in resolution, signal generation, and damage caused by the currently available techniques. Grain boundaries in silicon have been thoroughly studied, but applying the same level of radiation to other, less stable materials, like hybrid perovskites, initially led to a wealth of information being obtained from damaged materials. As such, particularly the field of electron microscopy of perovskite solar cell materials has had to focus on imaging reliably first, and then decide which information can be obtained within those parameters.

Similarly, advances in data analysis techniques can help further generate information and knowledge. Advances in manipulating large amounts of data can be, and is being, applied to microscopy, particularly the types where low signal-to-noise ratios make it difficult to extract reliable information from a single measurement. Combining the data recorded from many grain boundary measurements with low signal-to-noise ratio might make it possible to generate reliable statistics about the average distribution and properties of grain boundaries found in fragile materials. Coupled with recent advances in detection technology, lowering the amount of signal needed to generate actual measurements, means that we are likely going to experience a rapid increase in our ability to obtain and process large amounts of noisy data, turning it into useful information. Machine learning approaches are also now finding applications in STEM image analysis.[261]

Microscopic studies should always be focused on understanding the properties of bulk materials in the way that they are used. To this end, there will likely be an increase in the number of *in situ* and operando characterizations of solar cell materials, where a sample or device is exposed to the conditions it would experience in real-life operation, and then studied, either during or after the exposure. This type of microscopy introduces another level of complexity in terms of sample preparation and overall experimental setup, but undeniably provides a large amount of invaluable information about the microscopic mechanisms that govern the properties of energy materials.

In situ EM is commonly done for solution and electrochemistry, and it is likely that we will see more work studying photoactive materials in electron microscopes under illumination or other adverse conditions, enabling an understanding of the live operating mechanisms found within a material. This obviously exacerbates the potentially damaging influence of electron beams, and it is essential that it is possible to distinguish intrinsic properties from beam-induced ones.

Correlating grain boundary properties to device performance is the ultimate goal of any grain boundary studies, and the last several years of intense research has made it possible to optimize in particular, silicon solar cells by optimizing the grain boundary concentrations and properties. Grain boundaries in silicon are also very thoroughly understood through excellent work on modeling them in great detail, and similar work is currently being done to understand perovskite grain boundaries. The added degrees of freedom in hybrid perovskite in particular, adds additional complexities to this, however, in particular since the rotation of organic molecules has to be kept fixed, and the ionic conductivity of hybrid perovskites makes it difficult to make the same assumptions as used for silicon solar cells. As such, the field currently relies strongly on empirical evidence from microstructural studies to explain the properties of grain boundaries in perovskite solar cell

devices, but both theoretical and experimental techniques are improving rapidly.

Finally, by understanding the properties of grain boundaries, and understanding how to control their presence and properties, it is possible to guide the development and optimization of future energy materials. For example, there is evidence that some grain boundaries are beneficial to perovskite solar cells, but others are detrimental. It is therefore likely that solar cells containing many, or exclusively, the beneficial types of grain boundaries will have improved performance, and optimizing material deposition methods for this type of grain boundaries will be a desirable step in the preparation of solar cell devices.

VII. SUMMARY AND CONCLUSIONS

This review has introduced some basic concepts concerning the structure, stability, and properties of grain boundaries and described a range of first principles modeling and electron microscopy techniques that are powerful tools for understanding grain boundaries in real polycrystalline materials. Brief case studies focusing mainly on materials of relevance to energy materials (mainly for photovoltaic and photoelectrochemical applications but also including a material relevant for rechargeable batteries) provide examples of how these techniques are highly complementary and can provide insight into the impact of grain boundaries on material properties and ultimately device performance. We hope this will serve as an informative introduction for both theoretical and experimental researchers interested in understanding the properties of grain boundaries as well as a useful resource for those already experienced but wishing to learn more about methods used by current or prospective collaborators. While we have considered a relatively small number of materials, here the synergistic application of such methods can be employed for almost any polycrystalline material to understand the impact of grain boundaries on a wide range of materials properties relevant to diverse applications (e.g., including magnetic, thermoelectric, and chemical, for example). While the capabilities of both first principles modeling and electron microscopy techniques continue to advance rapidly as outlined in Sec. VI, many open challenges remain. However, there are also excellent prospects for further progress toward a more complete understanding of grain boundaries making this an exciting time to work on these problems.

AUTHOR DECLARATIONS
Conflict of Interest
The authors have no conflicts to disclose.

Author Contributions
James Quirk: Conceptualization (equal); Project administration (lead); Writing – original draft (equal); Writing – review & editing (equal). **Mathias Uller Rothmann:** Conceptualization (equal); Writing – original draft (equal); Writing – review & editing (equal). **Wei Li:** Conceptualization (equal); Supervision (equal); Writing – original draft (equal); Writing – review & editing (equal). **Daniel Abou-Ras:** Conceptualization (equal); Writing – original draft (equal); Writing – review & editing (equal). **Keith Patrick McKenna:** Conceptualization (equal); Project administration (lead); Supervision (equal); Writing – original draft (equal); Writing – review & editing (equal).

DATA AVAILABILITY

Data sharing is not applicable to this article as no new data were created or analyzed in this study.

REFERENCES

[1] A. P. Sutton and R. W. Balluffi, *Interfaces in Crystalline Materials* (Clarendon Press, Oxford, 2006).

[2] J. P. Hirth, "The influence of grain boundaries on mechanical properties," Metall. Trans. **3**(12), 3047–3067 (1972).

[3] R. Grantab, V. B. Shenoy, and R. S. Ruoff, "Anomalous strength characteristics of tilt grain boundaries in graphene," Science **330**(6006), 946–948 (2010).

[4] C. H. Seager, "Grain boundaries in polycrystalline silicon," Annu. Rev. Mater. Sci. **15**(1), 271–302 (1985).

[5] J. Y. W. Seto, "The electrical properties of polycrystalline silicon films," J. Appl. Phys. **46**(12), 5247–5254 (1975).

[6] F. Greuter and G. Blatter, "Electrical properties of grain boundaries in polycrystalline compound semiconductors," Semicond. Sci. Technol. **5**(2), 111–137 (1990).

[7] S. E. Babcock, X. Y. Cai, D. L. Kaiser, and D. C. Larbalestier, "Weak-link-free behaviour of high-angle $YBa_2Cu_3O_{7-\delta}$ grain boundaries in high magnetic fields," Nature **347**(6289), 167–169 (1990).

[8] K. P. McKenna and A. L. Shluger, "Electron-trapping polycrystalline materials with negative electron affinity," Nat. Mater. **7**(11), 859–862 (2008).

[9] O. Hunderi, "Influence of grain boundaries and lattice defects on the optical properties of some metals," Phys. Rev. B **7**(8), 3419–3429 (1973).

[10] W. B. Jackson, N. M. Johnson, and D. K. Biegelsen, "Density of gap states of silicon grain boundaries determined by optical absorption," Appl. Phys. Lett. **43**(2), 195–197 (1983).

[11] L. L. Kazmerski, M. Hallerdt, P. J. Ireland, R. A. Mickelsen, and W. S. Chen, "Optical properties and grain boundary effects in $CuInSe_2$," J. Vac. Sci. Technol. A **1**(2), 395–398 (1983).

[12] E. Bonetti, L. Del Bianco, D. Fiorani, D. Rinaldi, R. Caciuffo, and A. Hernando, "Disordered magnetism at the grain boundary of pure nanocrystalline iron," Phys. Rev. Lett. **83**(14), 2829–2832 (1999).

[13] S. Sugimoto, "Current status and recent topics of rare-earth permanent magnets," J. Phys. Appl. Phys. **44**(6), 064001 (2011).

[14] T. T. Sasaki, T. Ohkubo, and K. Hono, "Structure and chemical compositions of the grain boundary phase in Nd-Fe-B sintered magnets," Acta Mater. **115**, 269–277 (2016).

[15] K. P. McKenna, F. Hofer, D. Gilks, V. K. Lazarov, C. Chen, Z. Wang, and Y. Ikuhara, "Atomic-scale structure and properties of highly stable antiphase boundary defects in Fe_3O_4," Nat. Commun. **5**(1), 5740 (2014).

[16] D. M. Rowe and V. S. Shukla, "The effect of phonon-grain boundary scattering on the lattice thermal conductivity and thermoelectric conversion efficiency of heavily doped fine-grained, hot-pressed silicon germanium alloy," J. Appl. Phys. **52**(12), 7421–7426 (1981).

[17] E. Isotta, S. Jiang, G. Moller, A. Zevalkink, G. J. Snyder, and O. Balogun, "Microscale imaging of thermal conductivity suppression at grain boundaries," Adv. Mater. **35**(38), 2302777 (2023).

[18] J. Hu, Y. N. Shi, X. Sauvage, G. Sha, and K. Lu, "Grain boundary stability governs hardening and softening in extremely fine nanograined metals," Science **355**(6331), 1292–1296 (2017).

[19] C. H. Seager, D. S. Ginley, and J. D. Zook, "Improvement of polycrystalline silicon solar cells with grain-boundary hydrogenation techniques," Appl. Phys. Lett. **36**(10), 831–833 (1980).

[20]C. H. Seager, "Grain boundary recombination: Theory and experiment in silicon," J. Appl. Phys. **52**(6), 3960–3968 (1981).

[21]A. J. Minnich, M. S. Dresselhaus, Z. F. Ren, and G. Chen, "Bulk nanostructured thermoelectric materials: Current research and future prospects," Energy Environ. Sci. **2**(5), 466 (2009).

[22]C. Gayner and K. K. Kar, "Recent advances in thermoelectric materials," Prog. Mater. Sci. **83**, 330–382 (2016).

[23]Y. Yan, R. Noufi, and M. M. Al-Jassim, "Grain-boundary physics in polycrystalline CuInSe₂ revisited: experiment and theory," Phys. Rev. Lett. **96**(20), 205501 (2006).

[24]O. M. Rigby, T. Richards-Hlabangana, Q. M. Ramasse, I. MacLaren, R. A. Lomas-Zapata, M. S. Rumsey, K. P. McKenna, and B. G. Mendis, "Structure and electronic properties of domain walls and stacking fault defects in prospective photoferroic materials bournonite and enargite," J. Appl. Phys. **132**(18), 185001 (2022).

[25]M. Grätzel, "Photoelectrochemical cells," Nature **414**(6861), 338–344 (2001).

[26]J. Li and N. Wu, "Semiconductor-based photocatalysts and photoelectrochemical cells for solar fuel generation: A review," Catal. Sci. Technol. **5**(3), 1360–1384 (2015).

[27]H. Moriwake, X. Gao, A. Kuwabara, C. A. J. Fisher, T. Kimura, Y. H. Ikuhara, K. Kohama, T. Tojigamori, and Y. Ikuhara, "Domain boundaries and their influence on Li migration in solid-state electrolyte (La,Li)TiO3," J. Power Sources **276**, 203–207 (2013).

[28]J. D. Major, "Grain boundaries in CdTe thin film solar cells: A review," Semicond. Sci. Technol. **31**(9), 093001 (2016).

[29]D. W. de Quilettes, S. M. Vorpahl, S. D. Stranks, H. Nagaoka, G. E. Eperon, M. E. Ziffer, H. J. Snaith, and D. S. Ginger, "Impact of microstructure on local carrier lifetime in perovskite solar cells," Science **348**(6235), 683–686 (2015).

[30]Z. Wang, M. Saito, K. P. McKenna, and Y. Ikuhara, "Polymorphism of dislocation core structures at the atomic scale," Nat. Commun. **5**(1), 3239 (2014).

[31]M. U. Rothmann, J. S. Kim, J. Borchert, K. B. Lohmann, C. M. O'Leary, A. A. Sheader, L. Clark, H. J. Snaith, M. B. Johnston, P. D. Nellist, and L. M. Herz, "Atomic-scale microstructure of metal halide perovskite," Science **370**(6516), eabb5940 (2020).

[32]S. Cai, J. Dai, Z. Shao, M. U. Rothmann, Y. Jia, C. Gao, M. Hao, S. Pang, P. Wang, S. P. Lau, K. Zhu, J. J. Berry, L. M. Herz, X. C. Zeng, and Y. Zhou, "Atomically resolved electrically active intragrain interfaces in perovskite semiconductors," J. Am. Chem. Soc. **144**(4), 1910–1920 (2022).

[33]B. Gao, R. Jalem, H.-K. Tian, and Y. Tateyama, "Revealing atomic-scale ionic stability and transport around grain boundaries of garnet Li₇La₃Zr₂O₁₂ solid electrolyte," Adv. Energy Mater. **12**(3), 2102151 (2022).

[34]R. E. Williams, Q. M. Ramasse, K. P. McKenna, L. J. Phillips, P. J. Yates, O. S. Hutter, K. Durose, J. D. Major, and B. G. Mendis, "Evidence for self-healing benign grain boundaries and a highly defective Sb₂Se₃–CdS interfacial layer in Sb₂Se₃ thin-film photovoltaics," ACS Appl. Mater. Interfaces **12**(19), 21730–21738 (2020).

[35]K. P. McKenna, "Electronic properties of {111} twin boundaries in a mixed-ion lead halide perovskite solar absorber," ACS Energy Lett. **3**(11), 2663–2668 (2018).

[36]Y. Yan, C.-S. Jiang, R. Noufi, S.-H. Wei, H. R. Moutinho, and M. M. Al-Jassim, "Electrically benign behavior of grain boundaries in polycrystalline CuInSe₂ films," Phys. Rev. Lett. **99**(23), 235504 (2007).

[37]Y. Yan, K. M. Jones, C. S. Jiang, X. Z. Wu, R. Noufi, and M. M. Al-Jassim, "Understanding the defect physics in polycrystalline photovoltaic materials," Physica B **401–402**, 25–32 (2007).

[38]Y. Yan, W.-J. Yin, Y. Wu, T. Shi, N. R. Paudel, C. Li, J. Poplawsky, Z. Wang, J. Moseley, H. Guthrey, H. Moutinho, S. J. Pennycook, and M. M. Al-Jassim, "Physics of grain boundaries in polycrystalline photovoltaic semiconductors," J. Appl. Phys. **117**(11), 112807 (2015).

[39]J. A. Quirk, V. K. Lazarov, and K. P. McKenna, "Electronic properties of {112} and {110} twin boundaries in anatase TiO₂," Adv. Theory Simul. **2**(12), 1900157 (2019).

[40]Y. Sato, T. Mizoguchi, F. Oba, M. Yodogawa, T. Yamamoto, and Y. Ikuhara, "Identification of native defects around grain boundary in Pr-doped ZnO bicrystal using electron energy loss spectroscopy and first-principles calculations," Appl. Phys. Lett. **84**(26), 5311–5313 (2004).

[41]J. K. Mason and C. A. Schuh, in *Electron Backscatter Diffraction in Materials Science*, edited by A. J. Schwartz, M. Kumar, B. L. Adams, and D. P. Field (Springer, Boston, MA, 2009), pp. 35–51.

[42]A. J. Wilkinson and T. B. Britton, "Strains, planes, and EBSD in materials science," Mater. Today **15**(9), 366–376 (2012).

[43]A. Khorashadizadeh, D. Raabe, S. Zaefferer, G. S. Rohrer, A. D. Rollett, and M. Winning, "Five-parameter grain boundary analysis by 3D EBSD of an ultra fine grained CuZr Alloy processed by equal channel angular pressing," Adv. Eng. Mater. **13**(4), 237–244 (2011).

[44]D. Abou-Ras, A. Nikolaeva, S. Caicedo Dávila, M. Krause, H. Guthrey, M. Al-Jassim, M. Morawski, and R. Scheer, "No evidence for passivation effects of Na at grain boundaries in polycrystalline Cu(In,Ga)Se₂ thin films for solar cells," Sol. RRL **3**(8), 1900095 (2019).

[45]Thomas *et al.*, "Probing the changes in microscopic properties of Cu(In,Ga)Se₂ absorber in thin-film solar cells with respect to Ga variation and their effect on the open circuit voltage deficit," Sol. RRL (submitted).

[46]S. Siebentritt, M. Igalson, C. Persson, and S. Lany, "The electronic structure of chalcopyrites-bands, point defects and grain boundaries," Prog. Photovoltaics Res. Appl. **18**(6), 390–410 (2010).

[47]T. Kirchartz, K. Ding, and U. Rau, in *Advanced Characterization of Thin Film Solar Cells*, edited by D. Abou-Ras, T. Kirchartz, and U. Rau, 1st ed. (Wiley, 2011), pp. 33–60.

[48]C. R. Osterwald, *Practical Handbook of Photovoltaics* (Elsevier, 2003), pp. 793–816.

[49]K. Emery, in *Handbook of Photovoltaic Science and Engineering*, edited by A. Luque and S. Hegedus, 1st ed. (Wiley, 2003), pp. 701–752.

[50]T. Kirchartz, J. A. Márquez, M. Stolterfoht, and T. Unold, "Photoluminescence-based characterization of halide perovskites for photovoltaics," Adv. Energy Mater. **10**(26), 1904134 (2020).

[51]M. Krause, A. Nikolaeva, M. Maiberg, P. Jackson, D. Hariskos, W. Witte, J. A. Márquez, S. Levcenko, T. Unold, R. Scheer, and D. Abou-Ras, "Microscopic origins of performance losses in highly efficient Cu(In,Ga)Se₂ thin-film solar cells," Nat. Commun. **11**(1), 4189 (2020).

[52]A. P. Sutton and R. W. Balluffi, "Overview no. 61 On geometric criteria for low interfacial energy," Acta Metall. **35**(9), 2177–2201 (1987).

[53]J. J. Bean, M. Saito, S. Fukami, H. Sato, S. Ikeda, H. Ohno, Y. Ikuhara, and K. P. McKenna, "Atomic structure and electronic properties of MgO grain boundaries in tunnelling magnetoresistive devices," Sci. Rep. **7**(1), 45594 (2017).

[54]W. T. Read and W. Shockley, "Dislocation models of crystal grain boundaries," Phys. Rev. **78**(3), 275–289 (1950).

[55]Y. Cao, V. Fatemi, A. Demir, S. Fang, S. L. Tomarken, J. Y. Luo, J. D. Sanchez-Yamagishi, K. Watanabe, T. Taniguchi, E. Kaxiras, R. C. Ashoori, and P. Jarillo-Herrero, "Correlated insulator behaviour at half-filling in magic-angle graphene superlattices," Nature **556**(7699), 80–84 (2018).

[56]P. W. Tasker and D. M. Duffy, "On the structure of twist grain boundaries in ionic oxides," Philos. Mag. A **47**(6), L45–L48 (1983).

[57]R. W. Balluffi, A. Brokman, and A. H. King, "CSL/DSC lattice model for general crystalcrystal boundaries and their line defects," Acta Metall. **30**(8), 1453–1470 (1982).

[58]D. L. Olmsted, S. M. Foiles, and E. A. Holm, "Survey of computed grain boundary properties in face-centered cubic metals: I. Grain boundary energy," Acta Mater. **57**(13), 3694–3703 (2009).

[59]M. F. Ashby, F. Spaepen, and S. Williams, "The structure of grain boundaries described as a packing of polyhedra," Acta Metall. **26**(11), 1647–1663 (1978).

[60]H. Gleiter, "On the structure of grain boundaries in metals," Mater. Sci. Eng. **52**(2), 91–131 (1982).

[61]D. Schwartz, V. Vitek, and A. P. Sutton, "Atomic structure of (001) twist boundaries in f.c.c metals Structural unit model," Philos. Mag. A **51**(4), 499–520 (1985).

[62]A. P. Sutton, "On the structural unit model of grain boundary structure," Philos. Mag. Lett. **59**(2), 53–59 (1989).

[63]J. Han, V. Vitek, and D. J. Srolovitz, "The grain-boundary structural unit model redux," Acta Mater. **133**, 186–199 (2017).

[64]D. Abou-Ras, U. Bloeck, S. Caicedo-Dávila, H. Funk, A. Eljarrat, A. Hammud, S. Thomas, D. R. Wargulski, T. Lunkenbein, and C. T. Koch, "Correlative microscopy and monitoring of segregation processes in optoelectronic semiconductor materials and devices," J. Appl. Phys. **133**(12), 121101 (2023).

[65] W. Shan and W. A. Saidi, "Segregation of native defects to the grain boundaries in methylammonium lead iodide perovskite," J. Phys. Chem. Lett. **8**(23), 5935–5942 (2017).

[66] A. Stoffers, O. Cojocaru-Mirédin, W. Seifert, S. Zaefferer, S. Riepe, and D. Raabe, "Grain boundary segregation in multicrystalline silicon: Correlative characterization by EBSD, EBIC, and atom probe tomography: Grain boundary segregation in multicrystalline silicon," Prog. Photovoltaics Res. Appl. **23**(12), 1742–1753 (2015).

[67] W.-J. Yin, Y. Wu, R. Noufi, M. Al-Jassim, and Y. Yan, "Defect segregation at grain boundary and its impact on photovoltaic performance of CuInSe$_2$," Appl. Phys. Lett. **102**(19), 193905 (2013).

[68] J. H. Westbrook, "Segregation at grain boundaries," Metall. Rev. **9**(1), 415–471 (1964).

[69] X. Tingdong and C. Buyuan, "Kinetics of non-equilibrium grain-boundary segregation," Prog. Mater. Sci. **49**(2), 109–208 (2004).

[70] J. H. Harding, "Short-circuit diffusion in ceramics," Interface Sci. **11**(1), 81–90 (2003).

[71] M. J. Hÿtch, J.-L. Putaux, and J. Thibault, "Stress and strain around grain-boundary dislocations measured by high-resolution electron microscopy," Philos. Mag. **86**(29–31), 4641–4656 (2006).

[72] C.-J. Tong and K. P. McKenna, "Passivating grain boundaries in polycrystalline CdTe," J. Phys. Chem. C **123**(39), 23882–23889 (2019).

[73] N.-J. Hao, R.-X. Ding, C.-J. Tong, and K. P. McKenna, "Heterogeneity of grain boundary properties in Cu$_2$ZnSnS$_4$: A first-principles study," J. Appl. Phys. **133**(14), 145002 (2023).

[74] Z. Wang, M. Saito, K. P. McKenna, L. Gu, S. Tsukimoto, A. L. Shluger, and Y. Ikuhara, "Atom-resolved imaging of ordered defect superstructures at individual grain boundaries," Nature **479**(7373), 380–383 (2011).

[75] D. R. Clarke, "Grain boundaries in polycrystalline ceramics," Annu. Rev. Mater. Sci. **17**(1), 57–74 (1987).

[76] J. Buckeridge, "Equilibrium point defect and charge carrier concentrations in a material determined through calculation of the self-consistent Fermi energy," Comput. Phys. Commun. **244**, 329–342 (2019).

[77] F. J. Stützler, L. Tapfer, and H. J. Queisser, "Charged defect states at silicon grain boundaries," Mater. Sci. Forum **10–12**, 229–234 (1986).

[78] W. Shockley and W. T. Read, "Statistics of the recombinations of holes and electrons," Phys. Rev. **87**(5), 835–842 (1952).

[79] R. N. Hall, "Electron-hole recombination in germanium," Phys. Rev. **87**(2), 387–387 (1952).

[80] A. Alkauskas, Q. Yan, and C. G. Van De Walle, "First-principles theory of nonradiative carrier capture via multiphonon emission," Phys. Rev. B **90**(7), 075202 (2014).

[81] W. Van Roosbroeck, "Injected current carrier transport in a semi-infinite semiconductor and the determination of lifetimes and surface recombination velocities," J. Appl. Phys. **26**(4), 380–391 (1955).

[82] J. Brody and A. Rohatgi, "Analytical approximation of effective surface recombination velocity of dielectric-passivated p-type silicon," Solid-State Electron. **45**(9), 1549–1557 (2001).

[83] R. N. Hall, "Recombination processes in semiconductors," Proc. Inst. Electr. Eng. - Part B: Electr. Commun. Eng. **106**(17S), 923–931 (1959).

[84] J. P. McKelvey, "Experimental determination of injected carrier recombination rates at dislocations in semiconductors," Phys. Rev. **106**(5), 910–917 (1957).

[85] J. A. Quirk and K. P. McKenna, "Small-polaron mediated recombination in titanium dioxide from first principles," Phys. Rev. Res. **5**(2), 023072 (2023).

[86] J. Li, J. Huang, F. Ma, H. Sun, J. Cong, K. Privat, R. F. Webster, S. Cheong, Y. Yao, R. L. Chin, X. Yuan, M. He, K. Sun, H. Li, Y. Mai, Z. Hameiri, N. J. Ekins-Daukes, R. D. Tilley, T. Unold, M. A. Green, and X. Hao, "Unveiling microscopic carrier loss mechanisms in 12% efficient Cu$_2$ZnSnSe$_4$ solar cells," Nat. Energy **7**(8), 754–764 (2022).

[87] J. Bass, "Deviations from Matthiessen's rule," Adv. Phys. **21**(91), 431–604 (1972).

[88] B. J. Stanbery, D. Abou-Ras, A. Yamada, and L. Mansfield, "CIGS photovoltaics: Reviewing an evolving paradigm," J. Phys. Appl. Phys. **55**(17), 173001 (2022).

[89] J. B. Li, V. Chawla, and B. M. Clemens, "Investigating the role of grain boundaries in CZTS and CZTSSe thin film solar cells with scanning probe microscopy," Adv. Mater. **24**(6), 720–723 (2012).

[90] J.-W. Lee, S.-H. Bae, N. De Marco, Y.-T. Hsieh, Z. Dai, and Y. Yang, "The role of grain boundaries in perovskite solar cells," Mater. Today Energy **7**, 149–160 (2018).

[91] I. Visoly-Fisher, S. R. Cohen, K. Gartsman, A. Ruzin, and D. Cahen, "Understanding the beneficial role of grain boundaries in polycrystalline solar cells from single-grain-boundary scanning probe microscopy," Adv. Funct. Mater. **16**(5), 649–660 (2006).

[92] C. B. Carter and D. B. Williams, *Transmission Electron Microscopy: Diffraction, Imaging, and Spectrometry* (Springer, 2016).

[93] M. U. Rothmann, K. B. Lohmann, J. Borchert, M. B. Johnston, K. P. McKenna, L. M. Herz, and P. D. Nellist, "Atomistic understanding of the coherent interface between lead iodide perovskite and lead iodide," Adv. Mater. Interfaces **10**, 2300249 (2023).

[94] M. U. Rothmann, W. Li, J. Etheridge, and Y. Cheng, "Microstructural characterisations of perovskite solar cells – from grains to interfaces: Techniques, features, and challenges," Adv. Energy Mater. **7**(23), 1700912 (2017).

[95] H.-Q. Du, Y. Jiang, M. U. Rothmann, U. Bach, Y.-B. Cheng, and W. Li, "Transmission electron microscopy studies of organic–inorganic hybrid perovskites: Advances, challenges, and prospects," Appl. Phys. Rev. **10**(2), 021314 (2023).

[96] M. U. Rothmann, W. Li, Y. Zhu, A. Liu, Z. Ku, U. Bach, J. Etheridge, and Y.-B. Cheng, "Structural and chemical changes to CH$_3$NH$_3$PbI$_3$ induced by electron and gallium ion beams," Adv. Mater. **30**(25), 1800629 (2018).

[97] T. Ohno, S. Ii, N. Shibata, K. Matsunaga, Y. Ikuhara, and T. Yamamoto, "High resolution microscopy study for [001] symmetric tilt boundary with a tilt angle of 66° in Rutile-type TiO$_2$ bicrystal," Mater. Trans. **45**(7), 2117–2121 (2004).

[98] C. Sun, T. Paulauskas, F. G. Sen, G. Lian, J. Wang, C. Buurma, M. K. Y. Chan, R. F. Klie, and M. J. Kim, "Atomic and electronic structure of Lomer dislocations at CdTe bicrystal interface," Sci. Rep. **6**(1), 27009 (2016).

[99] B. Goodge, A. Carlsson, M. Bischoff, A. Mohammadi-Gheidari, G. Fallag, G. Schwind, C. Maunders, D. Muller, and L. Kourkoutis, "Sub-Ångstrom EDX mapping enabled by a high-brightness cold field emission source," Microsc. Microanal. **26**(S2), 1508–1511 (2020).

[100] Z. Liu, C. Sun, W. Wu, R. Gauvin, H. Demers, and Y. Zeng, "High spatial resolution EDS mapping of nanoparticles at low accelerating voltage," J. Test. Eval. **44**(6), 2285–2292 (2016).

[101] U. Rau, B. Blank, T. C. M. Müller, and T. Kirchartz, "Efficiency potential of photovoltaic materials and devices unveiled by detailed-balance analysis," Phys. Rev. Appl. **7**(4), 044016 (2017).

[102] D. Abou-Ras, M. Bär, R. Caballero, R. Gunder, C. Hages, M. D. Heinemann, C. A. Kaufmann, M. Krause, S. Levcenko, and R. Mainz, "Advanced characterization and in-situ growth monitoring of Cu(In,Ga)Se$_2$ thin films and solar cells," Sol. Energy **170**, 102–112 (2018).

[103] B. G. Mendis, L. Bowen, and Q. Z. Jiang, "A contactless method for measuring the recombination velocity of an individual grain boundary in thin-film photovoltaics," Appl. Phys. Lett. **97**(9), 092112 (2010).

[104] R. Brendel and A. Goetzberger, *Thin-Film Crystalline Silicon Solar Cells: Physics and Technology* (Wiley-VCH, Weinheim, 2003).

[105] H. C. Sio, T. Trupke, and D. Macdonald, "Quantifying carrier recombination at grain boundaries in multicrystalline silicon wafers through photoluminescence imaging," J. Appl. Phys. **116**(24), 244905 (2014).

[106] S. Riepe, G. Stokkan, T. Kieliba, and W. Warta, "Carrier density imaging as a tool for characterising the electrical activity of defects in pre-processed multicrystalline silicon," Solid State Phenom. **95–96**, 229–234 (2003).

[107] G. Stokkan, S. Riepe, O. Lohne, and W. Warta, "Spatially resolved modeling of the combined effect of dislocations and grain boundaries on minority carrier lifetime in multicrystalline silicon," J. Appl. Phys. **101**(5), 053515 (2007).

[108] G. Micard, G. Hahn, A. Zuschlag, S. Seren, and B. Terheiden, "Quantitative evaluation of grain boundary activity in multicrystalline semiconductors by light beam induced current: An advanced model," J. Appl. Phys. **108**(3), 034516 (2010).

[109] R. Corkish, T. Puzzer, A. B. Sproul, and K. L. Luke, "Quantitative interpretation of electron-beam-induced current grain boundary contrast profiles with application to silicon," J. Appl. Phys. **84**(10), 5473–5481 (1998).

[110] M. Nichterwitz, D. Abou-Ras, K. Sakurai, J. Bundesmann, T. Unold, R. Scheer, and H. W. Schock, "Influence of grain boundaries on current collection in Cu(In,Ga)Se$_2$ thin-film solar cells," Thin Solid Films **517**(7), 2554–2557 (2009).

31 January 2024 08:53:32

[111]D. Abou-Ras and T. Kirchartz, "Electron-beam-induced current measurements of thin-film solar cells," ACS Appl. Energy Mater. **2**(9), 6127–6139 (2019).

[112]C. Donolato, "Theory of beam induced current characterization of grain boundaries in polycrystalline solar cells," J. Appl. Phys. **54**(3), 1314–1322 (1983).

[113]G. C. Hasson, J. B. Guillot, B. Baroux, and C. Goux, "Structure and energy of grain boundaries: Application to symmetrical tilt boundaries around [100] in aluminium and copper," Phys. Status Solidi A **2**(3), 551–558 (1970).

[114]G. Hasson, J.-Y. Boos, I. Herbeuval, M. Biscondi, and C. Goux, "Theoretical and experimental determinations of grain boundary structures and energies: Correlation with various experimental results," Surf. Sci. **31**, 115–137 (1972).

[115]M. S. Daw and M. I. Baskes, "Embedded-atom method: Derivation and application to impurities, surfaces, and other defects in metals," Phys. Rev. B **29**(12), 6443–6453 (1984).

[116]M. S. Daw, S. M. Foiles, and M. I. Baskes, "The embedded-atom method: A review of theory and applications," Mater. Sci. Rep. **9**(7–8), 251–310 (1993).

[117]M. W. Finnis and J. E. Sinclair, "A simple empirical N-body potential for transition metals," Philos. Mag. A **50**(1), 45–55 (1984).

[118]J. M. Pénisson, U. Dahmen, and M. J. Mills, "HREM study of a $\sum = 3\{112\}$ twin boundary in aluminium," Philos. Mag. Lett. **64**(5), 277–283 (1991).

[119]H. Ichinose and Y. Ishida, "Observation of [110] tilt boundary structures in gold by high resolution HVEM," Philos. Mag. A **43**(5), 1253–1264 (1981).

[120]F. H. Stillinger and T. A. Weber, "Computer simulation of local order in condensed phases of silicon," Phys. Rev. B **31**(8), 5262–5271 (1985).

[121]J. Tersoff, "New empirical approach for the structure and energy of covalent systems," Phys. Rev. B **37**(12), 6991–7000 (1988).

[122]J. Tersoff, "Empirical interatomic potential for silicon with improved elastic properties," Phys. Rev. B **38**(14), 9902–9905 (1988).

[123]J. Tersoff, "Modeling solid-state chemistry: Interatomic potentials for multicomponent systems," Phys. Rev. B **39**(8), 5566–5568 (1989).

[124]D. W. Brenner, "Empirical potential for hydrocarbons for use in simulating the chemical vapor deposition of diamond films," Phys. Rev. B **42**(15), 9458–9471 (1990).

[125]M. Kohyama, "Computational studies of grain boundaries in covalent materials," Model. Simul. Mater. Sci. Eng. **10**(3), R31–R59 (2002).

[126]S. von Alfthan, P. D. Haynes, K. Kaski, and A. P. Sutton, "Are the structures of twist grain boundaries in silicon ordered at 0 K?," Phys. Rev. Lett. **96**(5), 055505 (2006).

[127]D. M. Duffy and P. W. Tasker, "Computer simulation of ⟨001⟩ tilt grain boundaries in nickel oxide," Philos. Mag. A **47**(6), 817–825 (1983).

[128]D. M. Duffy, "Grain boundaries in ionic crystals," J. Phys. C **19**(23), 4393–4412 (1986).

[129]G. W. Watson, E. T. Kelsey, N. H. De Leeuw, D. J. Harris, and S. C. Parker, "Atomistic simulation of dislocations, surfaces and interfaces in MgO," J. Chem. Soc. Faraday Trans. **92**(3), 433 (1996).

[130]T. Nishiyama, A. Seko, and I. Tanaka, "Application of machine learning potentials to predict grain boundary properties in fcc elemental metals," Phys. Rev. Mater. **4**(12), 123607 (2020).

[131]R. E. Thomson and D. J. Chadi, "Theoretical study of the electronic structure of a high-angle tilt grain boundary in Si," Phys. Rev. B **29**(2), 889–892 (1984).

[132]D. P. DiVincenzo, O. L. Alerhand, M. Schlüter, and J. W. Wilkins, "Electronic and structural properties of a twin boundary in Si," Phys. Rev. Lett. **56**(18), 1925–1928 (1986).

[133]T. A. Arias and J. D. Joannopoulos, "Electron trapping and impurity segregation without defects: *Ab initio* study of perfectly rebonded grain boundaries," Phys. Rev. B **49**(7), 4525–4531 (1994).

[134]J. Li, D. B. Mitzi, and V. B. Shenoy, "Structure and electronic properties of grain boundaries in earth-abundant photovoltaic absorber $Cu_2ZnSnSe_4$," ACS Nano **5**(11), 8613–8619 (2011).

[135]H. Van Swygenhoven, D. Farkas, and A. Caro, "Grain-boundary structures in polycrystalline metals at the nanoscale," Phys. Rev. B **62**(2), 831–838 (2000).

[136]J. H. Harding, D. J. Harris, and S. C. Parker, "Computer simulation of interfaces in ceramics," Mater. Res. Soc. Symp. Proc. **492**, 85–96 (1997).

[137]R. Hadian, B. Grabowski, and J. Neugebauer, "GB code: A grain boundary generation code," J. Open Source Software **3**(29), 900 (2018).

[138]J. Cheng, J. Luo, and K. Yang, "Aimsgb: An algorithm and open-source python library to generate periodic grain boundary structures," Comput. Mater. Sci. **155**, 92–103 (2018).

[139]Dataset: A. Kerrigan and K. McKenna (2022). "GBMaker," Zenodo. https://doi.org/10.5281/zenodo.6334740.

[140]L. Sun, M. A. L. Marques, and S. Botti, "Direct insight into the structure-property relation of interfaces from constrained crystal structure prediction," Nat. Commun. **12**(1), 811 (2021).

[141]B. Gao, P. Gao, S. Lu, J. Lv, Y. Wang, and Y. Ma, "Interface structure prediction via CALYPSO method," Sci. Bull. **64**(5), 301–309 (2019).

[142]G. Schusteritsch, R. Ishikawa, A. R. Elmaslmane, K. Inoue, K. P. McKenna, Y. Ikuhara, and C. J. Pickard, "Anataselike grain boundary structure in rutile titanium dioxide," Nano Lett. **21**(7), 2745–2751 (2021).

[143]A. L.-S. Chua, N. A. Benedek, L. Chen, M. W. Finnis, and A. P. Sutton, "A genetic algorithm for predicting the structures of interfaces in multicomponent systems," Nat. Mater. **9**(5), 418–422 (2010).

[144]E. J. Kirkland, *Advanced Computing in Electron Microscopy* (Springer Science & Business Media, 2010).

[145]C. T. Koch, "Determination of core structure periodicity and point defect density along dislocations," Ph.D. thesis (Arizona State University, 2002).

[146]J. Madsen and T. Susi, "The abTEM code: Transmission electron microscopy from first principles," Open Res. Eur. **1**, 24 (2021).

[147]A. H. Larsen, J. J. Mortensen, J. Blomqvist, I. E. Castelli, R. Christensen, M. Dułak, J. Friis, M. N. Groves, B. Hammer, C. Hargus, E. D. Hermes, P. C. Jennings, P. B. Jensen, J. Kermode, J. R. Kitchin, E. L. Kolsbjerg, J. Kubal, K. Kaasbjerg, S. Lysgaard, J. B. Maronsson, T. Maxson, T. Olsen, L. Pastewka, A. Peterson, C. Rostgaard, J. Schiøtz, O. Schütt, M. Strange, K. S. Thygesen, T. Vegge, L. Vilhelmsen, M. Walter, Z. Zeng, and K. W. Jacobsen, "The atomic simulation environment—A Python library for working with atoms," J. Phys. Condens. Matter **29**(27), 273002 (2017).

[148]E.-M. Steyskal, B. Oberdorfer, W. Sprengel, M. Zehetbauer, R. Pippan, and R. Würschum, "Direct experimental determination of grain boundary excess volume in metals," Phys. Rev. Lett. **108**(5), 055504 (2012).

[149]B. Oberdorfer, D. Setman, E.-M. Steyskal, A. Hohenwarter, W. Sprengel, M. Zehetbauer, R. Pippan, and R. Würschum, "Grain boundary excess volume and defect annealing of copper after high-pressure torsion," Acta Mater. **68**, 189–195 (2014).

[150]J. A. Quirk, B. Miao, B. Feng, G. Kim, H. Ohta, Y. Ikuhara, and K. P. McKenna, "Unveiling the electronic structure of grain boundaries in anatase with electron microscopy and first-principles modeling," Nano Lett. **21**(21), 9217–9223 (2021).

[151]E. R. Hoglund, D. Bao, A. O'Hara, T. W. Pfeifer, M. S. B. Hoque, S. Makarem, J. M. Howe, S. T. Pantelides, P. E. Hopkins, and J. A. Hachtel, "Direct visualization of localized vibrations at complex grain boundaries," Adv. Mater. **35**(13), 2208920 (2023).

[152]J. Wei, T. Ogawa, B. Feng, T. Yokoi, R. Ishikawa, A. Kuwabara, K. Matsunaga, N. Shibata, and Y. Ikuhara, "Direct measurement of electronic band structures at oxide grain boundaries," Nano Lett. **20**(4), 2530–2536 (2020).

[153]R. J. Nicholls and A. J. Scott, "Practical approaches to the accurate modelling of EELS edges using density functional theory," J. Phys. Conf. Ser. **126**, 012038 (2008).

[154]S. Körbel, D. Kammerlander, R. Sarmiento-Pérez, C. Attaccalite, M. A. L. Marques, and S. Botti, "Optical properties of Cu-chalcogenide photovoltaic absorbers from self-consistent *GW* and the Bethe-Salpeter equation," Phys. Rev. B **91**(7), 075134 (2015).

[155]R. Long, J. Liu, and O. V. Prezhdo, "Unravelling the effects of grain boundary and chemical doping on electron–hole recombination in $CH_3NH_3PbI_3$ perovskite by time-domain atomistic simulation," J. Am. Chem. Soc. **138**(11), 3884–3890 (2016).

[156]P. J. Dale and M. A. Scarpulla, "Efficiency versus effort: A better way to compare best photovoltaic research cell efficiencies?," Sol. Energy Mater. Sol. Cells **251**, 112097 (2023).

[157]R. Tang, X. Wang, W. Lian, J. Huang, Q. Wei, M. Huang, Y. Yin, C. Jiang, S. Yang, G. Xing, S. Chen, C. Zhu, X. Hao, M. A. Green, and T. Chen, "Hydrothermal deposition of antimony selenosulfide thin films enables solar cells with 10% efficiency," Nat. Energy **5**(8), 587–595 (2020).

[158]X. Wang, R. Tang, C. Jiang, W. Lian, H. Ju, G. Jiang, Z. Li, C. Zhu, and T. Chen, "Manipulating the electrical properties of $Sb_2(S,Se)_3$ film for high-efficiency solar cell," Adv. Energy Mater. **10**(40), 2002341 (2020).

[159]Y. Zhao, S. Wang, C. Jiang, C. Li, P. Xiao, R. Tang, J. Gong, G. Chen, T. Chen, J. Li, and X. Xiao, "Regulating energy band alignment via alkaline metal fluoride assisted solution post-treatment enabling $Sb_2(S,Se)_3$ solar cells with 10.7% efficiency," Adv. Energy Mater. **12**(1), 2103015 (2022).

[160]Y. Zhou, L. Wang, S. Chen, S. Qin, X. Liu, J. Chen, D.-J. Xue, M. Luo, Y. Cao, Y. Cheng, E. H. Sargent, and J. Tang, "Thin-film Sb_2Se_3 photovoltaics with oriented one-dimensional ribbons and benign grain boundaries," Nat. Photonics **9**(6), 409–415 (2015).

[161]C. Chen, L. Wang, L. Gao, D. Nam, D. Li, K. Li, Y. Zhao, C. Ge, H. Cheong, H. Liu, H. Song, and J. Tang, "6.5% certified efficiency Sb_2Se_3 solar cells using PbS colloidal quantum dot film as hole-transporting layer," ACS Energy Lett. **2**(9), 2125–2132 (2017).

[162]O. S. Hutter, L. J. Phillips, K. Durose, and J. D. Major, "6.6% efficient antimony selenide solar cells using grain structure control and an organic contact layer," Sol. Energy Mater. Sol. Cells **188**, 177–181 (2018).

[163]D.-B. Li, X. Yin, C. R. Grice, L. Guan, Z. Song, C. Wang, C. Chen, K. Li, A. J. Cimaroli, R. A. Awni, D. Zhao, H. Song, W. Tang, Y. Yan, and J. Tang, "Stable and efficient CdS/Sb_2Se_3 solar cells prepared by scalable close space sublimation," Nano Energy **49**, 346–353 (2018).

[164]X. Wen, C. Chen, S. Lu, K. Li, R. Kondrotas, Y. Zhao, W. Chen, L. Gao, C. Wang, J. Zhang, G. Niu, and J. Tang, "Vapor transport deposition of antimony selenide thin film solar cells with 7.6% efficiency," Nat. Commun. **9**(1), 2179 (2018).

[165]L. J. Phillips, C. N. Savory, O. S. Hutter, P. J. Yates, H. Shiel, S. Mariotti, L. Bowen, M. Birkett, K. Durose, D. O. Scanlon, and J. D. Major, "Current enhancement via a TiO_2 window layer for CSS Sb_2Se_3 solar cells: Performance limits and high V_{oc}," IEEE J. Photovoltaics **9**(2), 544–551 (2019).

[166]C. Chen, D. C. Bobela, Y. Yang, S. Lu, K. Zeng, C. Ge, B. Yang, L. Gao, Y. Zhao, M. C. Beard, and J. Tang, "Characterization of basic physical properties of Sb_2Se_3 and its relevance for photovoltaics," Front. Optoelectron. **10**(1), 18–30 (2017).

[167]X. Wang, Z. Li, S. R. Kavanagh, A. M. Ganose, and A. Walsh, "Lone pair driven anisotropy in antimony chalcogenide semiconductors," Phys. Chem. Chem. Phys. **24**(12), 7195–7202 (2022).

[168]R. E. Brandt, V. Stevanović, D. S. Ginley, and T. Buonassisi, "Identifying defect-tolerant semiconductors with high minority-carrier lifetimes: Beyond hybrid lead halide perovskites," MRS Commun. **5**(2), 265–275 (2015).

[169]C. N. Savory and D. O. Scanlon, "The complex defect chemistry of antimony selenide," J. Mater. Chem. A **7**(17), 10739–10744 (2019).

[170]K. P. McKenna, "Self-healing of broken bonds and deep gap states in Sb_2Se_3 and Sb_2S_3," Adv. Electron. Mater. **7**(3), 2000944 (2021).

[171]J. van Laar, A. Huijser, and T. L. van Rooy, "Electronic surface properties of Ga and In containing III–V compounds," J. Vac. Sci. Technol. **14**(4), 894–898 (1977).

[172]A. Puzder, A. J. Williamson, F. Gygi, and G. Galli, "Self-healing of CdSe nanocrystals: First-principles calculations," Phys. Rev. Lett. **92**(21), 217401 (2004).

[173]T. D. C. Hobson, L. J. Phillips, O. S. Hutter, K. Durose, and J. D. Major, "Defect properties of Sb_2Se_3 thin film solar cells and bulk crystals," Appl. Phys. Lett. **116**(26), 261101 (2020).

[174]A. Vashishtha, J. Kumar, N. Singh, and E. Edri, "Surface potential variation across (hk1) and non-(hk1) grain boundaries of antimony triselenide," J. Alloys Compd. **948**, 169714 (2023).

[175]J.-S. Park and A. Walsh, "Modeling grain boundaries in polycrystalline halide perovskite solar cells," Annu. Rev. Condens. Matter Phys. **12**(1), 95–109 (2021).

[176]Y. Zhou, L. M. Herz, A. K.-Y. Jen, and M. Saliba, "Advances and challenges in understanding the microscopic structure–property–performance relationship in perovskite solar cells," Nat. Energy **7**(9), 794–807 (2022).

[177]X. Zhao and R. Long, "Benign effects of twin boundaries on charge carrier lifetime in metal halide perovskites by a time-domain study," J. Phys. Chem. Lett. **12**(35), 8575–8582 (2021).

[178]W. Li, M. U. Rothmann, Y. Zhu, W. Chen, C. Yang, Y. Yuan, Y. Y. Choo, X. Wen, Y.-B. Cheng, U. Bach, and J. Etheridge, "The critical role of composition-dependent intragrain planar defects in the performance of $MA_{1-x}FA_xPbI_3$ perovskite solar cells," Nat. Energy **6**(6), 624–632 (2021).

[179]H. T. Pham, Y. Yin, G. Andersson, K. J. Weber, T. Duong, and J. Wong-Leung, "Unraveling the influence of CsCl/MACl on the formation of nanotwins, stacking faults and cubic supercell structure in FA-based perovskite solar cells," Nano Energy **87**, 106226 (2021).

[180]H. T. Pham, T. Duong, K. J. Weber, and J. Wong-Leung, "Insights into twinning formation in cubic and tetragonal multi-cation mixed-halide perovskite," ACS Mater. Lett. **2**(4), 415–424 (2020).

[181]D. Abou-Ras, B. Schaffer, M. Schaffer, S. S. Schmidt, R. Caballero, and T. Unold, "Direct insight into grain boundary reconstruction in polycrystalline $Cu(In,Ga)Se_2$ with atomic resolution," Phys. Rev. Lett. **108**(7), 075502 (2012).

[182]P. Schöppe, S. Schönherr, M. Chugh, H. Mirhosseini, P. Jackson, R. Wuerz, M. Ritzer, A. Johannes, G. Martínez-Criado, W. Wisniewski, T. Schwarz, C. T. Plass, M. Hafermann, T. D. Kühne, C. S. Schnohr, and C. Ronning, "Revealing the origin of the beneficial effect of cesium in highly efficient $Cu(In,Ga)Se_2$ solar cells," Nano Energy **71**, 104622 (2020).

[183]M. Raghuwanshi, J. Keutgen, A. M. Mio, H. Mirhosseini, T. D. Kühne, and O. Cojocaru-Mirédin, "The physics of twin boundary termination in $Cu(In,Ga)Se_2$ absorbers," Sol. RRL **7**(7), 2201033 (2023).

[184]M. Chugh, T. D. Kühne, and H. Mirhosseini, "Diffusion of alkali metals in polycrystalline $CuInSe_2$ and their role in the passivation of grain boundaries," ACS Appl. Mater. Interfaces **11**(16), 14821–14829 (2019).

[185]S. S. Schmidt, D. Abou-Ras, S. Sadewasser, W. Yin, C. Feng, and Y. Yan, "Electrostatic potentials at $Cu(In,Ga)Se_2$ grain boundaries: Experiment and simulations," Phys. Rev. Lett. **109**(9), 095506 (2012).

[186]D. Abou-Ras, C. T. Koch, V. Küstner, P. A. Van Aken, U. Jahn, M. A. Contreras, R. Caballero, C. A. Kaufmann, R. Scheer, T. Unold, and H.-W. Schock, "Grain-boundary types in chalcopyrite-type thin films and their correlations with film texture and electrical properties," Thin Solid Films **517**(7), 2545–2549 (2009).

[187]D. Abou-Ras, S. S. Schmidt, R. Caballero, T. Unold, H.-W. Schock, C. T. Koch, B. Schaffer, M. Schaffer, P.-P. Choi, and O. Cojocaru-Mirédin, "Confined and chemically flexible grain boundaries in polycrystalline compound semiconductors," Adv. Energy Mater. **2**(8), 992–998 (2012).

[188]A. Fujishima and K. Honda, "Electrochemical photolysis of water at a semiconductor electrode," Nature **238**(5358), 37–38 (1972).

[189]V. Scuderi, G. Impellizzeri, L. Romano, M. Scuderi, M. V. Brundo, K. Bergum, M. Zimbone, R. Sanz, M. A. Buccheri, F. Simone, G. Nicotra, B. G. Svensson, M. G. Grimaldi, and V. Privitera, "An enhanced photocatalytic response of nanometric TiO_2 wrapping of Au nanoparticles for eco-friendly water applications," Nanoscale **6**(19), 11189–11195 (2014).

[190]B. O'Regan and M. Grätzel, "A low-cost, high-efficiency solar cell based on dye-sensitized colloidal TiO_2 films," Nature **353**(6346), 737–740 (1991).

[191]H.-S. Kim, J.-W. Lee, N. Yantara, P. P. Boix, S. A. Kulkarni, S. Mhaisalkar, M. Grätzel, and N.-G. Park, "High efficiency solid-state sensitized solar cell-based on submicrometer rutile TiO_2 nanorod and $CH_3NH_3PbI_3$ perovskite sensitizer," Nano Lett. **13**(6), 2412–2417 (2013).

[192]E. Maras, M. Saito, K. Inoue, H. Jónsson, Y. Ikuhara, and K. P. McKenna, "Determination of the structure and properties of an edge dislocation in rutile TiO_2," Acta Mater. **163**, 199–207 (2019).

[193]W.-Y. Lee, P. D. Bristowe, Y. Gao, and K. L. Merkle, "The atomic structure of twin boundaries in rutile," Philos. Mag. Lett. **68**(5), 309–314 (1993).

[194]T. Luttrell, S. Halpegamage, J. Tao, A. Kramer, E. Sutter, and M. Batzill, "Why is anatase a better photocatalyst than rutile? - Model studies on epitaxial TiO_2 films," Sci. Rep. **4**(1), 4043 (2014).

[195]A. A. Gribb and J. F. Banfield, "Particle size effects on transformation kinetics and phase stability in nanocrystalline TiO_2," Am. Mineral. **82**(7–8), 717–728 (1997).

[196]R. L. Penn and J. F. Banfield, "Formation of rutile nuclei at anatase {112} twin interfaces and the phase transformation mechanism in nanocrystalline titania," Am. Mineral. **84**(5–6), 871–876 (1999).

[197]R. L. Penn and J. F. Banfield, "Oriented attachment and growth, twinning, polytypism, and formation of metastablephases: Insights from nanocrystalline TiO_2," Am. Mineral. **83**, 1077–1082 (1998).

[198]W. Yuan, J. Meng, B. Zhu, Y. Gao, Z. Zhang, C. Sun, and Y. Wang, "Unveiling the atomic structures of the minority surfaces of TiO_2 nanocrystals," Chem. Mater. **30**(1), 288–295 (2018).

[199]R. Huang and Y. Ikuhara, "STEM characterization for lithium-ion battery cathode materials," Curr. Opin. Solid State Mater. Sci. **16**(1), 31–38 (2012).

31 January 2024 08:53:32

[200]X. Liu and L. Gu, "Advanced transmission electron microscopy for electrode and solid-electrolyte materials in lithium-ion batteries," Small Methods **2**(8), 1800006 (2018).

[201]S. Sasano, R. Ishikawa, K. Kawahara, T. Kimura, Y. H. Ikuhara, N. Shibata, and Y. Ikuhara, "Grain boundary Li-ion conductivity in $(Li_{0.33}La_{0.56})TiO_3$ polycrystal," Appl. Phys. Lett. **116**(4), 043901 (2020).

[202]N. Balke, S. Jesse, A. N. Morozovska, E. Eliseev, D. W. Chung, Y. Kim, L. Adamczyk, R. E. García, N. Dudney, and S. V. Kalinin, "Nanoscale mapping of ion diffusion in a lithium-ion battery cathode," Nat. Nanotechnol. **5**(10), 749–754 (2010).

[203]K. Shen, Y. Wang, J. Zhang, Y. Zong, G. Li, C. Zhao, and H. Chen, "Revealing the effect of grain boundary segregation on Li ion transport in polycrystalline anti-perovskite Li_3ClO: A phase field study," Phys. Chem. Chem. Phys. **22**(5), 3030–3036 (2020).

[204]B. Chen, C. Xu, and J. Zhou, "Insights into grain boundary in lithium-rich anti-perovskite as solid electrolytes," J. Electrochem. Soc. **165**(16), A3946 (2018).

[205]J. A. Dawson, H. Chen, and I. Tanaka, "Crystal structure, defect chemistry and oxygen ion transport of the ferroelectric perovskite, $Na_{0.5}Bi_{0.5}TiO_3$: Insights from first-principles calculations," J. Mater. Chem. A **3**(32), 16574–16582 (2015).

[206]X. He, H. Sun, X. Ding, and K. Zhao, "Grain boundaries and their impact on li kinetics in layered-oxide cathodes for Li-ion batteries," J. Phys. Chem. C **125**(19), 10284–10294 (2021).

[207]J. A. Dawson and I. Tanaka, "Li intercalation into a β-MnO_2 grain boundary," ACS Appl. Mater. Interfaces **7**(15), 8125–8131 (2015).

[208]A. R. Symington, M. Molinari, J. A. Dawson, J. M. Statham, J. Purton, P. Canepa, and S. C. Parker, "Elucidating the nature of grain boundary resistance in lithium lanthanum titanate," J. Mater. Chem. A **9**(10), 6487–6498 (2021).

[209]J. A. Dawson, P. Canepa, T. Famprikis, C. Masquelier, and M. S. Islam, "Atomic-scale influence of grain boundaries on Li-ion conduction in solid electrolytes for all-solid-state batteries," J. Am. Chem. Soc. **140**(1), 362–368 (2018).

[210]Y. Inaguma, L. Chen, M. Itoh, and T. Nakamura, "Candidate compounds with perovskite structure for high lithium ionic conductivity," Solid State Ion. **70–71**, 196–202 (1994).

[211]C. Shao, H. Liu, Z. Yu, Z. Zheng, N. Sun, and C. Diao, "Structure and ionic conductivity of cubic $Li_7La_3Zr_2O_{12}$ solid electrolyte prepared by chemical co-precipitation method," Solid State Ion. **287**, 13–16 (2016).

[212]X. Liu, R. Garcia-Mendez, A. R. Lupini, Y. Cheng, Z. D. Hood, F. Han, A. Sharafi, J. C. Idrobo, N. J. Dudney, C. Wang, C. Ma, J. Sakamoto, and M. Chi, "Local electronic structure variation resulting in Li 'filament' formation within solid electrolytes," Nat. Mater. **20**(11), 1485–1490 (2021).

[213]S. Yu and D. J. Siegel, "Grain boundary contributions to Li-ion transport in the solid electrolyte $Li_7La_3Zr_2O_{12}$ (LLZO)," Chem. Mater. **29**(22), 9639–9647 (2017).

[214]F. Han, A. S. Westover, J. Yue, X. Fan, F. Wang, M. Chi, D. N. Leonard, N. J. Dudney, H. Wang, and C. Wang, "High electronic conductivity as the origin of lithium dendrite formation within solid electrolytes," Nat. Energy **4**(3), 187–196 (2019).

[215]A. G. Squires, D. W. Davies, S. Kim, D. O. Scanlon, A. Walsh, and B. J. Morgan, "Low electronic conductivity of $Li_7La_3Zr_2O_{12}$ solid electrolytes from first principles," Phys. Rev. Mater. **6**(8), 085401 (2022).

[216]H. Jeong Lee, B. Darminto, S. Narayanan, M. Diaz-Lopez, A. W. Xiao, Y. Chart, J. Hoon Lee, J. A. Dawson, and M. Pasta, "Li-ion conductivity in $Li_2OHCl_{1-x}Br_x$ solid electrolytes: Grains, grain boundaries and interfaces," J. Mater. Chem. A **10**(21), 11574–11586 (2022).

[217]J. A. Dawson, P. Canepa, M. J. Clarke, T. Famprikis, D. Ghosh, and M. S. Islam, "Toward understanding the different influences of grain boundaries on ion transport in sulfide and oxide solid electrolytes," Chem. Mater. **31**(14), 5296–5304 (2019).

[218]J. H. Werner and J. H. Werner, in *Polycrystalline Semiconductors*, edited by H. J. Möller and H. P. Strunk (Springer, Berlin, Heidelberg, 1989), pp. 345–351.

[219]S. Riepe, I. E. Reis, W. Kwapil, M. A. Falkenberg, J. Schön, H. Behnken, J. Bauer, D. Kreßner-Kiel, W. Seifert, and W. Koch, "Research on efficiency limiting defects and defect engineering in silicon solar cells - results of the German research cluster SolarFocus," Phys. Status Solidi C **8**(3), 733–738 (2011).

[220]A. Liu, S. P. Phang, and D. Macdonald, "Gettering in silicon photovoltaics: A review," Sol. Energy Mater. Sol. Cells **234**, 111447 (2022).

[221]D. Macdonald and L. J. Geerligs, "Recombination activity of interstitial iron and other transition metal point defects in p- and n-type crystalline silicon," Appl. Phys. Lett. **85**(18), 4061–4063 (2004).

[222]J. Schmidt, B. Lim, D. Walter, K. Bothe, S. Gatz, T. Dullweber, and P. P. Altermatt, "Impurity-related limitations of next-generation industrial silicon solar cells," IEEE J. Photovoltaics **3**(1), 114–118 (2013).

[223]G. Stokkan, A. Song, and B. Ryningen, "Investigation of the grain boundary character and dislocation density of different types of high performance multi-crystalline silicon," Crystals **8**(9), 341 (2018).

[224]S. Ratanaphan, Y. Yoon, and G. S. Rohrer, "The five parameter grain boundary character distribution of polycrystalline silicon," J. Mater. Sci. **49**(14), 4938–4945 (2014).

[225]J. Chen, T. Sekiguchi, D. Yang, F. Yin, K. Kido, and S. Tsurekawa, "Electron-beam-induced current study of grain boundaries in multicrystalline silicon," J. Appl. Phys. **96**(10), 5490–5495 (2004).

[226]P. P. Altermatt and G. Heiser, "Development of a three-dimensional numerical model of grain boundaries in highly doped polycrystalline silicon and applications to solar cells," J. Appl. Phys. **91**(7), 4271–4274 (2002).

[227]T. Fujisaki, A. Yamada, and M. Konagai, "Effects of grain boundaries on cell performance of poly-silicon thin film solar cells by 2-D simulation," Sol. Energy Mater. Sol. Cells **74**(1–4), 331–337 (2002).

[228]U. Hess, P. Y. Pichon, S. Seren, A. Schönecker, and G. Hahn, "Crystal defects and their impact on ribbon growth on substrate (RGS) silicon solar cells," Sol. Energy Mater. Sol. Cells **117**, 471–475 (2013).

[229]C. T. Trinh, M. Bokalic, N. Preissler, M. Trahms, D. Abou-Ras, R. Schlatmann, D. Amkreutz, and M. Topic, "Assessment of bulk and interface quality for liquid phase crystallized silicon on glass," IEEE J. Photovoltaics **9**(2), 364–373 (2019).

[230]H. C. Sio, S. P. Phang, T. Trupke, and D. Macdonald, "Impact of phosphorous gettering and hydrogenation on the surface recombination velocity of grain boundaries in p-type multicrystalline silicon," IEEE J. Photovoltaics **5**(5), 1357–1365 (2015).

[231]H. C. Sio and D. Macdonald, "Direct comparison of the electrical properties of multicrystalline silicon materials for solar cells: Conventional p-type, n-type and high performance p-type," Sol. Energy Mater. Sol. Cells **144**, 339–346 (2016).

[232]S. Tsurekawa, K. Kido, and T. Watanabe, "Measurements of potential barrier height of grain boundaries in polycrystalline silicon by Kelvin probe force microscopy," Philos. Mag. Lett. **85**(1), 41–49 (2005).

[233]L.-P. Scheller and N. H. Nickel, "Charge transport in polycrystalline silicon thin-films on glass substrates," J. Appl. Phys. **112**(1), 013713 (2012).

[234]J. M. Burst, S. B. Farrell, D. S. Albin, E. Colegrove, M. O. Reese, J. N. Duenow, D. Kuciauskas, and W. K. Metzger, "Carrier density and lifetime for different dopants in single-crystal and polycrystalline CdTe," APL Mater. **4**(11), 116102 (2016).

[235]J. M. Burst, J. N. Duenow, D. S. Albin, E. Colegrove, M. O. Reese, J. A. Aguiar, C.-S. Jiang, M. K. Patel, M. M. Al-Jassim, D. Kuciauskas, S. Swain, T. Ablekim, K. G. Lynn, and W. K. Metzger, "CdTe solar cells with open-circuit voltage breaking the 1 V barrier," Nat. Energy **1**(3), 16015 (2016).

[236]H. R. Moutinho, R. G. Dhere, M. J. Romero, C.-S. Jiang, B. To, and M. M. Al-Jassim, "Electron backscatter diffraction of CdTe thin films: Effects of $CdCl_2$ treatment," J. Vac. Sci. Technol. A **26**(4), 1068–1073 (2008).

[237]G. Stechmann, S. Zaefferer, P. Konijnenberg, D. Raabe, C. Gretener, L. Kranz, J. Perrenoud, S. Buecheler, and A. N. Tiwari, "3-Dimensional microstructural characterization of CdTe absorber layers from CdTe/CdS thin film solar cells," Sol. Energy Mater. Sol. Cells **151**, 66–80 (2016).

[238]C. Li, Y. Wu, J. Poplawsky, T. J. Pennycook, N. Paudel, W. Yin, S. J. Haigh, M. P. Oxley, A. R. Lupini, M. Al-Jassim, S. J. Pennycook, and Y. Yan, "Grain-boundary-enhanced carrier collection in CdTe solar cells," Phys. Rev. Lett. **112**(15), 156103 (2014).

[239]J. D. Poplawsky, N. R. Paudel, C. Li, C. M. Parish, D. Leonard, Y. Yan, and S. J. Pennycook, "Direct imaging of Cl- and Cu-induced short-circuit efficiency changes in CdTe solar cells," Adv. Energy Mater. **4**(15), 1400454 (2014).

[240]A. Kanevce, J. Moseley, M. Al-Jassim, and W. K. Metzger, "Quantitative determination of grain-boundary recombination velocity in CdTe by cathodoluminescence measurements and numerical simulations," IEEE J. Photovoltaics **5**(6), 1722–1726 (2015).

[241]G. Stechmann, S. Zaefferer, T. Schwarz, P. Konijnenberg, D. Raabe, C. Gretener, L. Kranz, J. Perrenoud, S. Buecheler, and A. Nath Tiwari, "A correlative investigation of grain boundary crystallography and electronic properties in CdTe thin film solar cells," Sol. Energy Mater. Sol. Cells **166**, 108–120 (2017).

[242]W. K. Metzger, D. Albin, M. J. Romero, P. Dippo, and M. Young, "CdCl$_2$ treatment, S diffusion, and recombination in polycrystalline CdTe," J. Appl. Phys. **99**(10), 103703 (2006).

[243]J. Moseley, P. Rale, S. Collin, E. Colegrove, H. Guthrey, D. Kuciauskas, H. Moutinho, M. Al-Jassim, and W. K. Metzger, "Luminescence methodology to determine grain-boundary, grain-interior, and surface recombination in thin-film solar cells," J. Appl. Phys. **124**(11), 113104 (2018).

[244]U. Rau, K. Taretto, and S. Siebentritt, "Grain boundaries in Cu(In,Ga)(Se,S)$_2$ thin-film solar cells," Appl. Phys. A **96**(1), 221–234 (2009).

[245]D. Abou-Ras, S. S. Schmidt, N. Schäfer, J. Kavalakkatt, T. Rissom, T. Unold, R. Mainz, A. Weber, T. Kirchartz, E. Simsek Sanli, P. A. Van Aken, Q. M. Ramasse, H.-J. Kleebe, D. Azulay, I. Balberg, O. Millo, O. Cojocaru-Mirédin, D. Barragan-Yani, K. Albe, J. Haarstrich, and C. Ronning, "Compositional and electrical properties of line and planar defects in Cu(In,Ga)Se$_2$ thin films for solar cells—A review," Phys. Status Solidi RRL **10**(5), 363–375 (2016).

[246]O. Cojocaru-Mirédin, M. Raghuwanshi, R. Wuerz, and S. Sadewasser, "Grain boundaries in Cu(In,Ga)Se$_2$: A review of composition–electronic property relationships by atom probe tomography and correlative microscopy," Adv. Funct. Mater. **31**(41), 2103119 (2021).

[247]O. Cojocaru-Mirédin, T. Schwarz, and D. Abou-Ras, "Assessment of elemental distributions at line and planar defects in Cu(In,Ga)Se$_2$ thin films by atom probe tomography," Scr. Mater. **148**, 106–114 (2018).

[248]M. Raghuwanshi, R. Wuerz, and O. Cojocaru-Mirédin, "Interconnection between trait, structure, and composition of grain boundaries in Cu(In,Ga)Se$_2$ thin-film solar cells," Adv. Funct. Mater. **30**(31), 2001046 (2020).

[249]M. Raghuwanshi, M. Chugh, G. Sozzi, A. Kanevce, T. D. Kühne, H. Mirhosseini, R. Wuerz, and O. Cojocaru-Mirédin, "Fingerprints indicating superior properties of internal interfaces in Cu(In,Ga)Se$_2$ thin-film solar cells," Adv. Mater. **34**(37), 2203954 (2022).

[250]D. Abou-Ras, N. Schäfer, T. Rissom, M. N. Kelly, J. Haarstrich, C. Ronning, G. S. Rohrer, and A. D. Rollett, "Grain-boundary character distribution and correlations with electrical and optoelectronic properties of CuInSe$_2$ thin films," Acta Mater. **118**, 244–252 (2016).

[251]S. Sadewasser, D. Abou-Ras, D. Azulay, R. Baier, I. Balberg, D. Cahen, S. Cohen, K. Gartsman, K. Ganesan, J. Kavalakkatt, W. Li, O. Millo, T. Rissom, Y. Rosenwaks, H.-W. Schock, A. Schwarzman, and T. Unold, "Nanometer-scale electronic and microstructural properties of grain boundaries in Cu(In, Ga)Se$_2$," Thin Solid Films **519**(21), 7341–7346 (2011).

[252]N. Nicoara, R. Manaligod, P. Jackson, D. Hariskos, W. Witte, G. Sozzi, R. Menozzi, and S. Sadewasser, "Direct evidence for grain boundary passivation in Cu(In,Ga)Se$_2$ solar cells through alkali-fluoride post-deposition treatments," Nat. Commun. **10**(1), 3980 (2019).

[253]J.-J. Li, J.-Y. Ma, Q.-Q. Ge, J.-S. Hu, D. Wang, and L.-J. Wan, "Microscopic investigation of grain boundaries in organolead halide perovskite solar cells," ACS Appl. Mater. Interfaces **7**(51), 28518–28523 (2015).

[254]J. S. Yun, A. Ho-Baillie, S. Huang, S. H. Woo, Y. Heo, J. Seidel, F. Huang, Y.-B. Cheng, and M. A. Green, "Benefit of grain boundaries in organic–inorganic halide planar perovskite solar cells," J. Phys. Chem. Lett. **6**(5), 875–880 (2015).

[255]J. S. Yun, J. Seidel, J. Kim, A. M. Soufiani, S. Huang, J. Lau, N. J. Jeon, S. I. Seok, M. A. Green, and A. Ho-Baillie, "Critical role of grain boundaries for ion migration in formamidinium and methylammonium lead halide perovskite solar cells," Adv. Energy Mater. **6**(13), 1600330 (2016).

[256]N. Faraji, C. Qin, T. Matsushima, C. Adachi, and J. Seidel, "Grain boundary engineering of halide perovskite CH$_3$NH$_3$PbI$_3$ Solar Cells with photochemically active additives," J. Phys. Chem. C **122**(9), 4817–4821 (2018).

[257]H.-S. Kim and N.-G. Park, "Parameters affecting I–V hysteresis of CH$_3$NH$_3$PbI$_3$ perovskite solar cells: Effects of perovskite crystal size and mesoporous TiO$_2$ layer," J. Phys. Chem. Lett. **5**(17), 2927–2934 (2014).

[258]A. M. A. Leguy, Y. Hu, M. Campoy-Quiles, M. I. Alonso, O. J. Weber, P. Azarhoosh, M. van Schilfgaarde, M. T. Weller, T. Bein, J. Nelson, P. Docampo, and P. R. F. Barnes, "Reversible hydration of CH$_3$NH$_3$PbI$_3$ in films, single crystals, and solar cells," Chem. Mater. **27**(9), 3397–3407 (2015).

[259]J. Euvrard, Y. Yan, and D. B. Mitzi, "Electrical doping in halide perovskites," Nat. Rev. Mater. **6**(6), 531–549 (2021).

[260]E. Gutierrez-Partida, H. Hempel, S. Caicedo-Dávila, M. Raoufi, F. Peña-Camargo, M. Grischek, R. Gunder, J. Diekmann, P. Caprioglio, K. O. Brinkmann, H. Köbler, S. Albrecht, T. Riedl, A. Abate, D. Abou-Ras, T. Unold, D. Neher, and M. Stolterfoht, "Large-grain double cation perovskites with 18 μs lifetime and high luminescence yield for efficient inverted perovskite solar cells," ACS Energy Lett. **6**(3), 1045–1054 (2021).

[261]M. Ziatdinov, A. Ghosh, C. Wong, and S. V. Kalinin, "AtomAI framework for deep learning analysis of image and spectroscopy data in electron and scanning probe microscopy," Nat. Mach. Intell. **4**, 1101–1112 (2022).

31 January 2024 08:53:32